Title
Quantitative dissection of pattern formation along the central dogma in the early fly embryos

Author
Kim, Yang Joon

Publication Date
2021

Peer reviewed|Thesis/dissertation

Quantitative dissection of pattern formation along the central dogma in the early fly embryos

by

Yang Joon Kim

A dissertation submitted in partial satisfaction of the

requirements for the degree of

Doctor of Philosophy

in

Biophysics

in the

Graduate Division

of the

University of California, Berkeley

Committee in charge:

Professor Hernan G. Garcia, Chair
Professor Michael Eisen
Professor Xavier Darzacq
Professor Rob Phillips

Fall 2021

Quantitative dissection of pattern formation along the central dogma in the early fly embryos

Abstract

Quantitative dissection of pattern formation along the central dogma in the early fly embryos

by

Yang Joon Kim

Doctor of Philosophy in Biophysics

University of California, Berkeley

Professor Hernan G. Garcia, Chair

The question of how a cell determines which cell fate it will adopt is at the heart of developmental biology. In most cases, morphogens (mainly transcription factors or signaling molecules) control cell fates by directing cells to activate or repress downstream gene expression programs containing a specific subset of genes required for the desired cell function and morphology. Over the past few decades, this question has been dissected in great detail in several model organisms. One of the best-studied examples is the early embryo of the fruit fly, *Drosophila melanogaster*, whose cascade of gene expression network has been revealed by decades of hard work. Indeed, the fruit fly is one of the first organisms whose morphogens were identified using mutant screens pioneered by Christiane Nüsslein-Volhard and Eric Wieschaus. The identified morphogens revealed how the initial gradients of morphogens instruct cells at different positions along the embryo body axis to adopt different fates, such as those corresponding to legs or antennae, by activating differential transcriptional programs.

For the past decade, this knowledge of classic developmental biology, which revealed great details about the underlying gene regulatory networks, has been under quantitative dissection via the development of a wide array of new experimental techniques. The accumulation of these quantitative data demands quantitative models to understand the underlying principles behind the gene regulation. Ultimately, one of the dreams of developmental biologists is to have a predictive understanding of gene expression patterns solely from the patterns of input morphogens and the regulatory DNA sequences.

I believe that the field of developmental biology is at an exciting new phase where quantitative measurements meet theoretical modeling to unveil the molecular underpinnings of transcriptional and translational regulation. In my view, the dream of predictive developmental biology can only be achieved by an active dialogue between theoretical modeling that generates experimentally testable hypotheses and quantitative measurements to test these hypotheses.

My dissertation is an attempt to contribute to this new phase of quantitative data meeting

theoretical modeling by developing and characterizing molecular tools for quantitative measurements of gene expression following the central dogma (transcription and translation), and theoretical frameworks to understand and predict transcriptional regulation and protein pattern formation.

To my family, Heegyum Kim, Wonhee Kim, Sareum Kim, and my wife, Olivia Woojung Lee.

Contents

List of Figures

List of Tables

Acknowledgments

As a young and naive Physics undergraduate, I came to the United States for my Ph.D. with the ambition of rewriting the developmental biology textbooks with theoretical models and fancy math equations. After six and a half years, I am still far from that ambition, actually realizing that I am more ignorant than ever. However, when I reflect on my Ph.D., I realize how lucky I have been that I had so many valuable experiences such as having fun doing crazy experiments at midnight, traveling to Woods Hole to teach a course, learning excellent research inside and outside of the lab. Of course, there were darker days that I felt like none of my projects were working, and I wasted several months or years. However, now I know that these darker days were also part of the journey named Ph.D., just like Frodo Baggins' journey in the Lord of the Rings. Overall, I felt that I have grown up to be a much better scientific researcher than in seven years: I got a prestigious fellowship from a foundation in Korea, pushing my project to publication, making connections to many great scientists, and learning how to do science better. I could become a slightly better scientist than before because I had an incredibly nurturing environment over the past six and a half years. With that, I would like to thank those who made that nurturing environment.

First and foremost, I want to thank my advisor, Hernan Garcia, who has given me endless support in both intellectual and emotional ways. First, he gave me a great degree of intellectual freedom to do exploratory research, make crazy transgenic flies, and make my own mistakes. Thanks to Hernan's critical and thoughtful feedback, I also learned how to write science in English. I also appreciate his kindness in being present when I needed him the most. He always tried his best to make himself available for discussions, a quick chat, or emergency meetings. I learned so much from his fearless, audacious attitude in science, pushing me out of my comfort zone. Now I know that I could learn the most by going out of my comfort zone and challenging myself. My interaction with him is so rich that I cannot possibly write down all the great things that I appreciate for him. I hope I can keep this great mentor even after my graduation.

Teaching Physical Biology of the Cell course with Hernan was one of my Ph.D.'s hardest and most rewarding experiences. Although I majored in physics as an undergraduate, statistical mechanics has been the most challenging topic. I learned so much from Hernan's pedagogical approach to science: spending a lot of effort unpacking the contents to general audiences.

Thanks to my thesis and qualifying exam committee: Nipam Patel, Xavier Darzacq, Ahmet Yildiz, Michael (Mike) Eisen, and Rob Phillips. First, Nipam, who used to have his lab next to our lab, has taught me the basics of fly genetics and the beauty of clever genetic tricks. Second, Xavier served for my qualifying exam and thesis committee and helped me with critical feedback on my projects. Mike has influenced me in exposure to open science and how to make scientific research more available to broader audiences in the scientific community. I had a lot of fun interacting with Ahmet over the past six years, rotating in his lab working on single-molecules studies on motor protein, dynein, and teaching with him last year on Introduction to Biophysics. Lastly, Rob Phillips has been my scientific grandfather

and a mentor for science and life. I had the privilege of knowing and interacting with him closely for courses at Woods Hole Marine Biological Laboratory, CalTech, his visits to our lab, and joint retreats. I appreciate his willingness to discuss matters beyond science with me. Also, a shout out to the Biophysics program coordinator, Kate Chase, who always kindly replied to my questions and helped me go through sophisticated paper works painlessly.

My collaborators inside and outside the lab made it possible for me to put together the work presented here. I would like to start with the earliest lab members of the Garcia lab, Matty Norstad, and Jacques Bothma. Matty Norstad was a lab technician who taught me the beauty of Gibson Assembly, molecular cloning and fly genetics. Jacques Bothma has taught me some of the most sophisticated fly genetics tricks and mentored me on designing and pushing the project more efficiently. I learned a lot from my discussion on designing flies, projects, and papers in general. I had much fun working closely with Paul Jeammet and Kaitlin Rhee on the second chapter. We spent a long time in the microscope room, discussing science, which I truly enjoyed. Jonathan Liu has been my go-to person in theoretical modeling and data science questions. I really appreciate him making himself available for almost any time and teaching me how to model and apply Bayesian inference techniques to look at my data more closely. Armando Reimer greatly improved the Garcia laboratory's computational image analysis pipeline, which enabled the live imaging experiments shown here. I worked closely with Simon Alamos and Jordan Xiao to generate functional optogenetic fly transcription factors. Jake Zhao and Nicholas Lammers took this effort and generated the fly lines and exciting optogenetic Knirps. Meghan Turner and I did initial characterizations of many MCP and LlamaTag components together, which constituted some of the workhorse fly lines in the lab. Gabriella Martini and I worked closely on the translational dynamics project. Without her effort to generate fly lines and perform complicated fly husbandry during the pandemic, it would not have been possible to push the project this far. Yasemin Kiriscioglu and I have been working closely on chapter 5. I learned a lot about Bayesian inference Steve Small at NYU has helped me interpret my results from chapter 2, providing *in situ* raw data for chapter 3. I wish I had more overlap with our talented postdocs, Bruno Morreti, Brandon Schlomann, and Julia Falo-SanJuan. They had given me a lot of helpful feedback on my manuscript, and I am looking forward to what they will accomplish in Garcia lab after my departure.

I also want to thank researchers at Chan Zuckerberg Biohub for making the last part of my Ph.D. more fun and joyful. Angela Pisco has allowed me to learn about the single-cell genomics field within three months. Special thanks to Jonathan Liu for introducing me to the data science team at Biohub and kindly walking me through the spatial transcriptomics research at Biohub. I am genuinely excited about my new chapter at Biohub as a bioinformatics data scientist.

I would like to thank my family for their unlimited support on my journey for the past 30 years. Khalil Gibran wrote that parents are the bows from which their children as living arrows are sent forth. My parents have been the most robust bow I could possibly imagine. No matter what I wanted to do, they always supported me more than I could ask. My parents spent countless hours driving me to English schools far from my place, pulled in their belts

for my tuition. They also had to put up with seeing me only once in a year or two during my Ph.D. days. Without their sacrifice, love, and support, it would not have been possible for me to get this far in my life.

Lastly, I could not have finished my graduate school without the support and love from my wife, Woojung Olivia Lee. Since we met on a blind date ten years ago, she has given me enormous love and cheerleading that embraced me up from many frustrating failures during my academic journey. She gave me emotional support and academic support as my fellow researcher since she started her Ph.D. program. As a former MCB major, she has been my best-tester for most of my talks, posters, and any sort of scientific products that I make.

The Korea Foundation for Advanced Studies (KFAS) has supported me generously with their scholarship and network. The Burroughs Wellcome Fund Career Award supported the laboratory of Hernan Garcia at the Scientific Interface, the Sloan Research Foundation, the Human Frontiers Science Program, the Searle Scholars Program, the Shurl, and Kay Curci Foundation, the Hellman Foundation, the NIH Director's New Innovator Award (DP2 OD024541-01), and an NSF CAREER Award (1652236).

Chapter 1

Lighting up the Central Dogma during the development of early fly embryos - An Introduction

The question of how a cell determines which cell fate it will adopt is at the heart of developmental biology. In most cases, morphogens (mainly transcription factors or signaling molecules) control cell fates by directing cells to activate or repress downstream gene expression programs containing a specific subset of genes required for the desired cell function and morphology. Over the past few decades, this question has been dissected in great detail in several model organisms. One of the best-studied examples is the early embryo of the fruit fly, *Drosophila melanogaster*, whose cascade of gene expression network has been revealed by decades of hard work as shown in Figure 1.1A (Garcia et al. 2020; Gilbert 2010). Indeed, the fruit fly is one of the first organisms whose morphogens were identified using mutant screens (Nusslein-Volhard and Wieschaus 1980; Nusslein-Volhard, Wieschaus, and Kluding 1984). The identified morphogens revealed how the initial gradients of morphogens instruct cells at different positions along the embryo body axis to adopt different fates, such as those corresponding to legs or antennae, by activating differential transcriptional programs (Fig. 1.1A).

For the past decade, this knowledge of classic developmental biology, which revealed great details about the underlying gene regulatory networks, has been under quantitative dissection via the development of a wide array of new experimental techniques (Garcia et al. 2020; Small and Arnosti 2020). The accumulation of these quantitative data (see Bothma et al. (2014), Garcia et al. (2013b), Gregor et al. (2007b), Lammers et al. (2020), Lucas et al. (2013), and Reeves et al. (2012)) demands quantitative models to understand the underlying principles behind the gene regulation (Garcia et al. 2020). Ultimately, one of the dreams of developmental biologists is to have a predictive understanding of gene expression patterns solely from the patterns of input morphogens and the regulatory DNA sequences.

I believe that the field of developmental biology is at an exciting new phase where quantitative measurements meet theoretical modeling to unveil the molecular underpinnings of

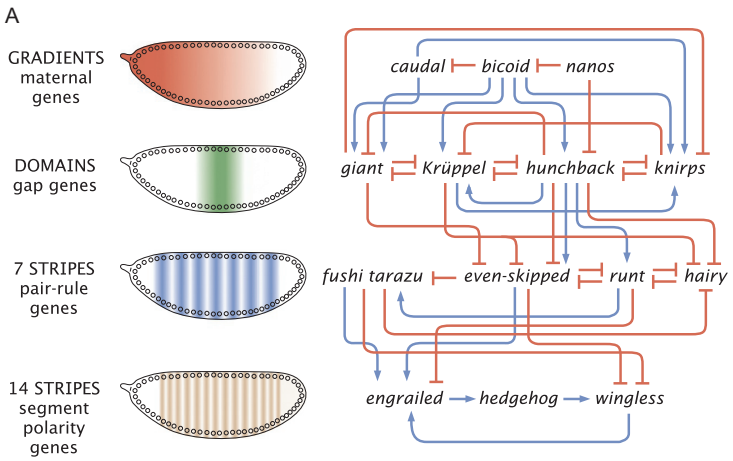

Figure 1.1: *Drosophila melanogaster* gene regulatory network. **(A)** Current state-of-the-art mapping of the gene regulatory network in segmentation of anterior-posterior axis of the fruit fly *Drosophila melanogaster*. Figure and caption are adapted from (Garcia et al. 2020).

transcriptional and translational regulation. In my view, the dream of predictive developmental biology can only be achieved by an active dialogue between theoretical modeling that generates experimentally testable hypotheses and quantitative measurements to test these hypotheses.

My dissertation is an attempt to contribute to this new phase of quantitative data meeting theoretical modeling by developing and characterizing molecular tools for quantitative measurements of gene expression following the central dogma (transcription and translation), and theoretical frameworks to understand and predict transcriptional regulation and protein pattern formation (outlined in Fig. 1.2). In this chapter, I will provide a preview of the later chapters of this thesis together with a summary of the key experiments and results.

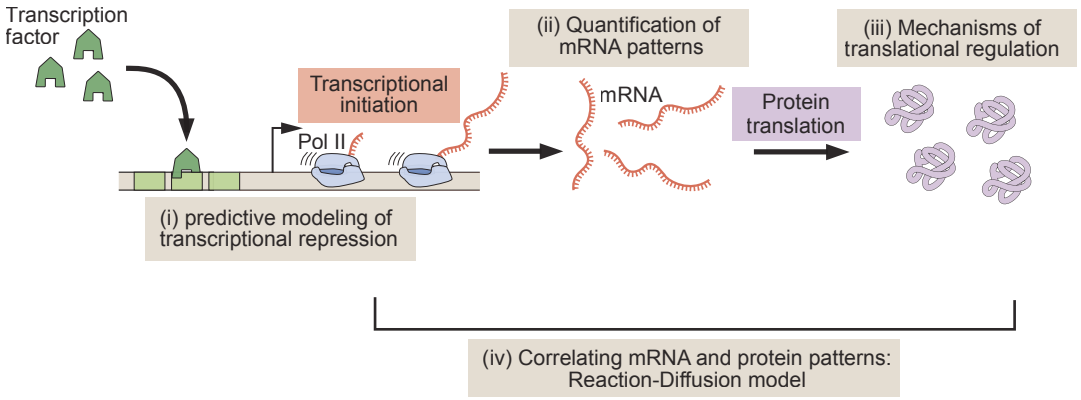

Figure 1.2: Outline of the thesis. The chapters are organized loosely following the steps of the Central Dogma. (i) Understanding the input-output function of transcriptional initiation (Chapter 2). (ii) Comparative study on methods to quantify cytoplasmic mRNA (Chapter 3). (iii) Quantification of translation dynamics (Chapter 4). (iv) Quantifying the pattern formation along the Central Dogma using reaction-diffusion models (Chapter 5).

1.1 Preview of Chapter 2: Understanding the transcriptional input-output function in repression

In the early fruit fly embryo, most morphogens are transcription factors that either activate or repress the level of transcription of downstream genes. These transcription factors bind to a sequence of regulatory DNA called an enhancer that dictates the output level of transcription as a function of input transcription factor concentrations. Thus, enhancer sequence define gene regulatory input-output functions (Furlong and Levine 2018). The study of these input-output functions has accumulated great knowledge of the architectures of various enhancers and the number and position of each transcription factor binding site inside that enhancer (Small and Arnosti 2020).

From this knowledge of activators and repressors (especially where they bind to exert their regulatory action), synthetic enhancers where one introduces transcription factor binding sites in existing scaffold have been used to characterize the identity of a given transcription factor as either activator or repressor (Chen et al. 2012; Löhr et al. 2009; Papagianni et al. 2018). However, we are still far from rationally designing enhancer sequences with precisely predicted output levels of transcription. For example, if we want to decrease the transcription level by a factor of two, how many repressor binding sites should we add in an enhancer, or how much do we need to increase the concentration of the repressor protein? These questions

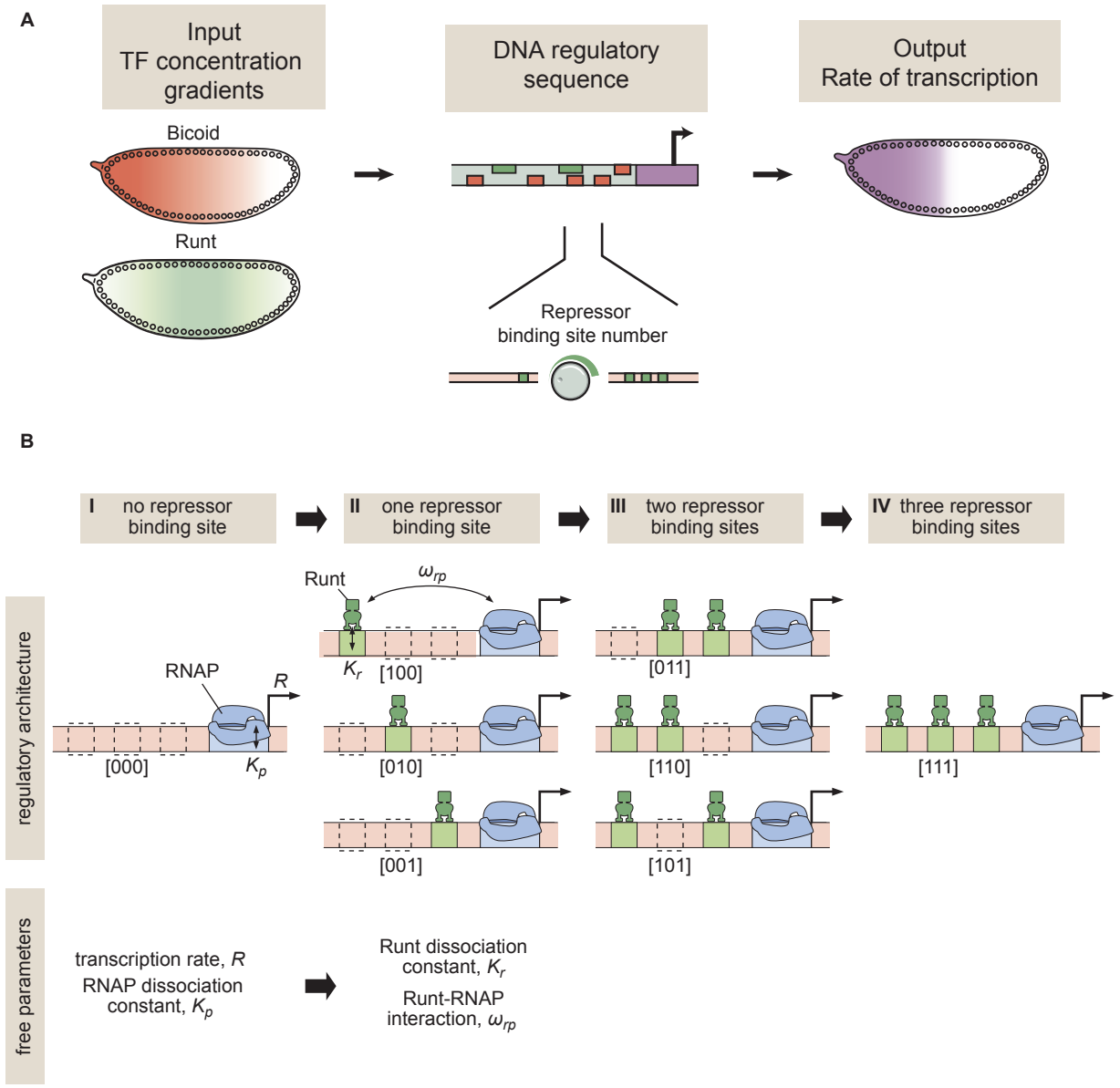

Figure 1.3: Preview of chapter 2. See caption in the next page.

clearly show our lack of predictive understanding of transcriptional input-output function where inputs are the concentration of transcription factors and their binding sites in a given enhancer, and the output is the level of transcription.

In this chapter, we chose a simple system of synthetic enhancers with binding sites for an activator, Bicoid, and a repressor, Runt, that we can use to build tractable theoretical

Figure 1.3: Preview of chapter 2. **(A)** Input-Output function framework of transcriptional regulation. Here, we present a case study with one activator (Bicoid) and one repressor (Runt) that regulate synthetic enhancers where the number and position of repressor binding sites can be systematically tuned. **(B)** A theoretical model of transcriptional repression. (I) We assume that transcription occurs with a rate R when the promoter is occupied by RNA polymerase II (RNAP), and that RNAP has a dissociation constant to the promoter of K_p. (II) The one-Runt binding site at different positions: when the Runt repressor is bound to its binding site, it interacts with RNAP with an interaction term, ω_{rp}. We assume that all Runt binding sites have the same dissociation constant of K_r. (III, IV) Two- and three- Runt binding sites as combinatorics of (II): the minimal model assumes that the two Runt molecules act independently with the RNAP. In this case, we can generate quantitative predictions for the transcriptional output from these two- or three-Runt binding sites cases.

models with a handful of parameters (Fig. 1.3 A and B). Specifically, we tested whether widespread thermodynamic models could be used to infer parameters describing simple regulatory architectures that inform parameter-free predictions of more complex enhancers in the context of transcriptional repression by Runt in the early fruit fly embryo (shown in Fig. 1.4).

By modulating the number and placement of Runt binding sites within an enhancer and quantifying the resulting transcriptional activity using live imaging, we discovered that thermodynamic models could successfully explain the experimental data for one-Runt binding site cases. However, the parameter-free prediction for two- or three-Runt binding site constructs cannot recapitulate the experimental data and could explain the data only when we invoke interaction terms between multiple molecular players beyond pairwise interactions between transcription factors and RNA polymerases. This multi-component interaction captures the combinatorial complexity underlying eukaryotic transcriptional regulation and cannot be determined from simpler regulatory architectures, highlighting the challenges in reaching a predictive understanding of transcriptional regulation in eukaryotes and calling for approaches that quantitatively dissect their molecular nature.

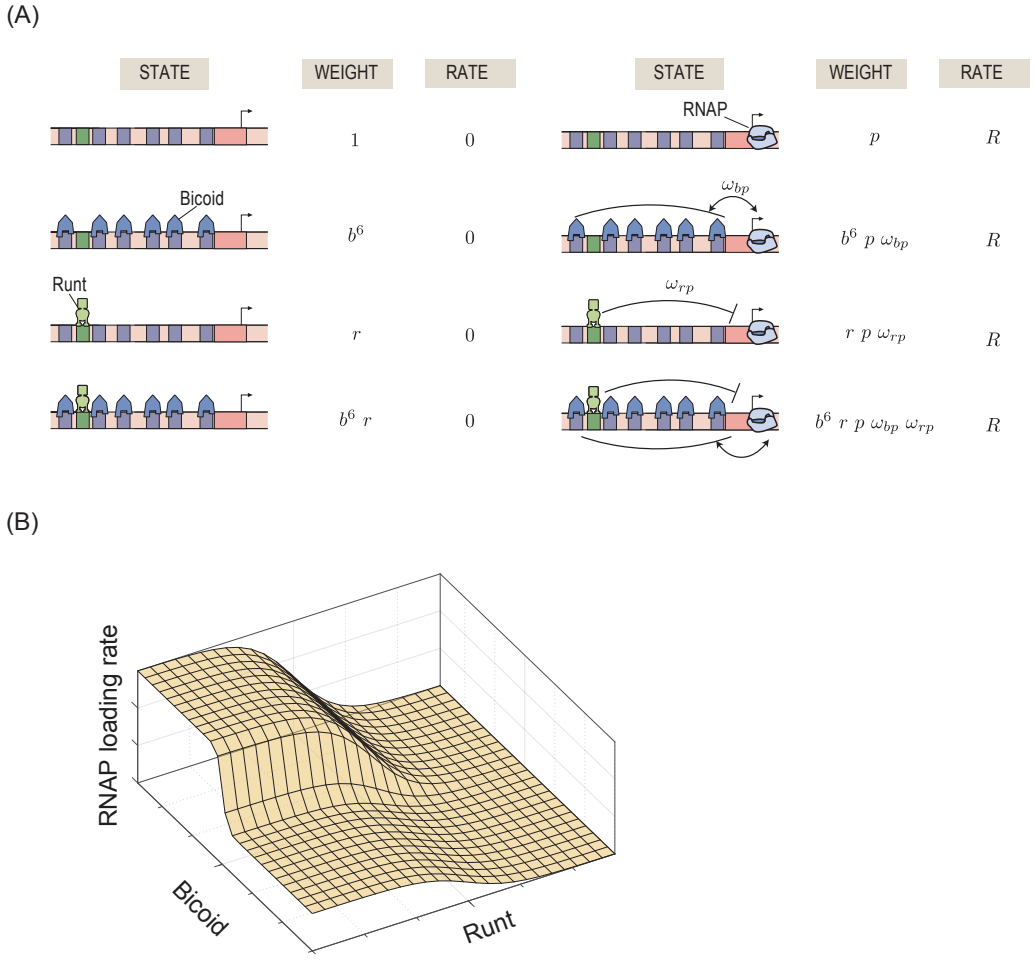

Figure 1.4: Thermodynamic model of transcriptional regulation by Bicoid activator and Runt repressor generates quantitative, experimentally testable predictions of transcriptional output. **(A)** States and statistical weights for the regulation of *hunchback* P2 with one Runt binding site in the limit of strong Bicoid-Bicoid cooperativity. Here, we use the dimensionless parameters $b = [Bicoid]/K_b$, $r = [Runt]/K_r$, and $p = [RNAP]/K_p$, where K_b, K_r, and K_p are the dissociation constants of Bicoid, Runt, and RNAP, respectively. ω_{bp} represents the cooperativity between Bicoid and RNAP, ω_{rp} captures the cooperativity between Runt and RNAP, and R represents the rate of transcription when the promoter is occupied by RNAP. The top two rows correspond to states where only Bicoid and RNAP act, while the bottom two rows represent repression by Runt. **(B)** Representative prediction of RNAP loading rate as a function of Bicoid and Runt concentrations for $\omega_{bp} = 3, \omega_{rp} = 0.001, p = 0.001, R = 1(AU/min)$.

1.2 Preview of Chapter 3: Comparison of methods to quantify cytoplasmic mRNA patterns

Chapter 3 focuses on a comparative study of experimental methods to measure cytoplasmic mRNA patterns in the fly embryo. An accurate quantification method is essential to characterizing the patterns of transcription factors and their downstream gene products. There are several experimental methods that have been widely used by developmental biologists to quantify cytoplasmic mRNA patterns. However, there is lack of comparative studies in assessing these methods in terms of their quantitative power. In this chapter, we want to compare these methods to test whether different methods give equivalent quantitative results or not.

One of the widely used techniques to measure the gene expression pattern is *in situ* hybridization. Here, the RNA of interest is hybridized with complementary DNA probes followed by the tagging of those complexes with fluorophores or enzymatic probes for characterization of the gene expression patterns. There are broadly two categories of *in situ* hybridization methods depending on the source of the signal: chemogenic and fluorogenic. The chemogenic method is called colorimetric *in situ* hybridization (which we refer to as *in situ* throughout this thesis). It relies on an enzymatic reaction, such as that catalyzed by alkaline phosphatase, with its substrate bound which generates a colored precipitate (as showcased in Fig. 1.5 A) (Small 2000). The fluorogenic method is called fluorescence *in situ* hybridization (which we refer to as FISH), relying on fluorophores attached to the primary or secondary antibodies that bind to the DNA probe, thus generating a fluorescence signal that is proportional to the number of mRNA molecules (as showcased in Fig. 1.5B). These in situ hybridization methods could be multiplexed to detect multiple mRNA species simultaneously (Chen et al. 2015). An alternative approach is tagging the nascent transcripts using bacteriophage stem-loop structures such that the inserted sequence of MS2 (or PP7) forms a loop structure upon transcription which is then bound by bacteriophage coat proteins such as MCP (or PCP) fused to fluorescent proteins (Bertrand et al. 1998). This tagging system enables quantification of the number of nascent transcripts actively being transcribed in real-time by monitoring the MS2 *spots* as shown in Figure 1.5C (Garcia et al. 2013b). By integrating the MS2 spot fluorescence intensity over time, it is possible to calculate the accumulated mRNA quantity (Garcia et al. 2013b).

All of the methods mentioned above have different types of caveats. For example, *in situ* hybridization methods could be used for the multiplexed detection of hundreds to thousands of mRNA species, whereas stem-loop methods can detect no more than two or three genes at a time. Also, while stem-loop methods enable the tracking of transcriptional dynamics in real-time at the single-cell level, *in situ* hybridization methods require fixed samples and thus offer data from a snapshot. Of course, there is no perfect method; instead, for each experimental need, there is one method more suitable than the other in terms of throughput, ease of use, and accuracy. In this section, we will perform a comparative study for colorimetric in situ hybridization (*in situ*), fluorescence in situ hybridization (FISH), and MS2-MCP

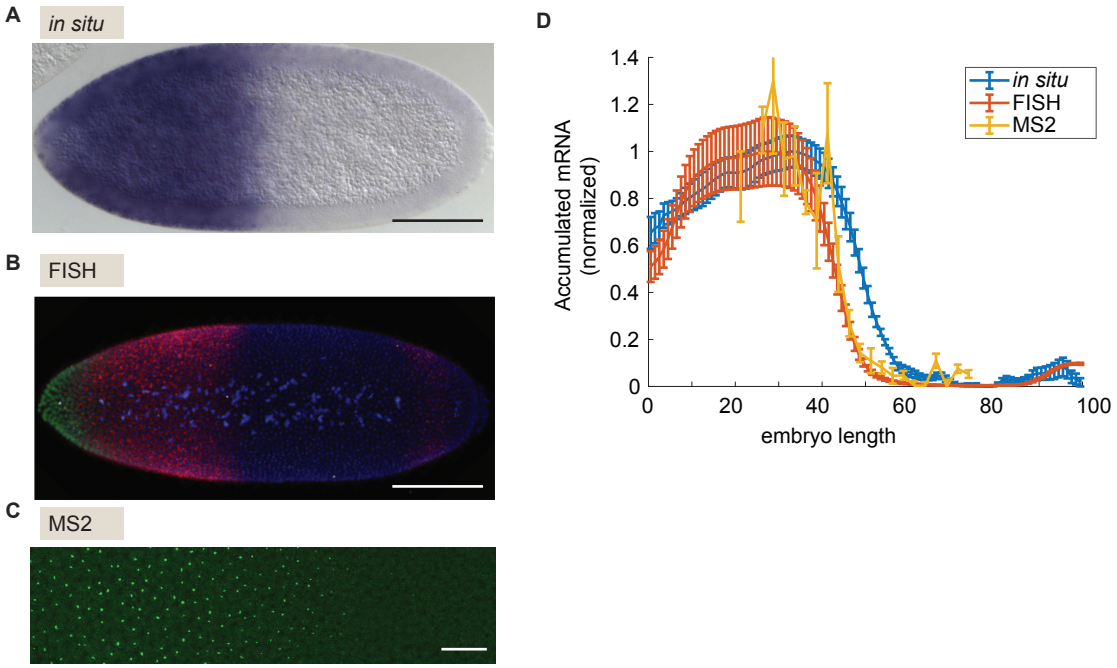

Figure 1.5: Experimental methods to measure cytoplasmic mRNA patterns. **(A,B,C)** Snapshot of fly embryos featuring cytoplasmic mRNA patterns driven by the *hunchback* P2 enhancer in nuclear cycle 14. **(A)** Colorimetric *in situ* hybridization. Scale bar represents 100 μm. **(B)** Fluorescence *in situ* hybridization (FISH) with red probe and co-stained with Bicoid protein with green probe. Scale bar represents 100 μm. (B) is adapted from Park et al. (2019). **(C)** MS2 with MCP-GFP. Green dots represent loci of active transcription. The embryo image shows 20-60% of the embryo length along the anterior-posterior axis. Scale bar represents 20 μm. **(D)** Comparison of the patterns of cytoplasmic mRNA acquired using different experimental methods. The y-axis shows the accumulated mRNA from each method normalized by the accumulated mRNA values at 20% of the embryo length.

techniques to assess their accuracy in quantifying the cytoplasmic mRNA patterns in the fruit fly embryos.

To compare these three different methods in their ability to quantify the cytoplasmic mRNA patterns, we chose the well-characterized system of the *hunchback* P2 enhancer that is known to drive a step-like pattern of mRNA (Perry, Boettiger, and Levine 2011). We used all three methods for the same construct that drives transcription under the *hunchback* P2 enhancer. We observed a difference in the patterns of cytoplasmic mRNA between the three methods as shown in Figure 1.5D. Briefly, the FISH and MS2 data showed agreement while the *in situ* showed a more posteriorly shifted pattern. In conclusion, we revealed the pros and cons of different methods of quantifying the patterns of cytoplasmic mRNA, facilitating the choice of experimental method that is more suitable for one's specific scientific question.

1.3 Preview of Chapter 4: Quantitative dissection of the translational regulation dynamics

Although most studies in developmental biology have treated mRNA and protein patterns more or less equivalently (**Gilbert2014**), there is emerging evidence that this equivalence might not hold true for some cases. Indeed, studies suggest that translation efficiency is not uniform across space and time and is under regulation (Dufourt et al. 2021; Surkova et al. 2019; Vinter et al. 2021). One of the most well-known examples of translational regulation is the regulation of maternal gradients in the early fruit fly embryos. For example, *caudal* mRNA is supplied maternally with a uniform distribution along the embryo's anterior-posterior axis. The translation of *caudal* mRNA is repressed by Bicoid, which forms an exponentially decaying gradient along the anterior-posterior axis. Thus, Bicoid represses the translation of *caudal* mRNA mainly at the anterior pole, leading to an opposite gradient of Caudal protein which peaks at the posterior and decreases towards anterior as shown in Figure 1.6 A and B. Another well-studied example is the translational regulation of maternal *hunchback* mRNA. The maternal gene *nanos* is expressed in a protein concentration gradient which is high in the posterior end of the embryo and low in the anterior end. Nanos protein is known to bind to the 3'UTR of the *hunchback* mRNA via Pumilio. Nanos protein represses the translation of maternal hunchback mRNA, which leads to a step-like expression emerging from uniform mRNA distribution along the anterior-posterior axis (Murata and Wharton 1995; Wharton et al. 1998). Our goal in this chapter is to dissect the translational regulatory logic encoded by different 3'UTR sequences, such as those corresponding to *caudal* and maternal *hunchback*. Although it has been known that the protein levels are downregulated by these translational repressors (either Bicoid or Nanos), the molecular mechanism by which this repression is achieved still remains elusive. For example, there could be different strategies to achieve an equivalent level of translational repression: either regulating the rate of translational initiation, the fraction of mRNA engaged in translation, or any combination thereof as shown in Figure 1.6 C (Vinter et al. 2021).

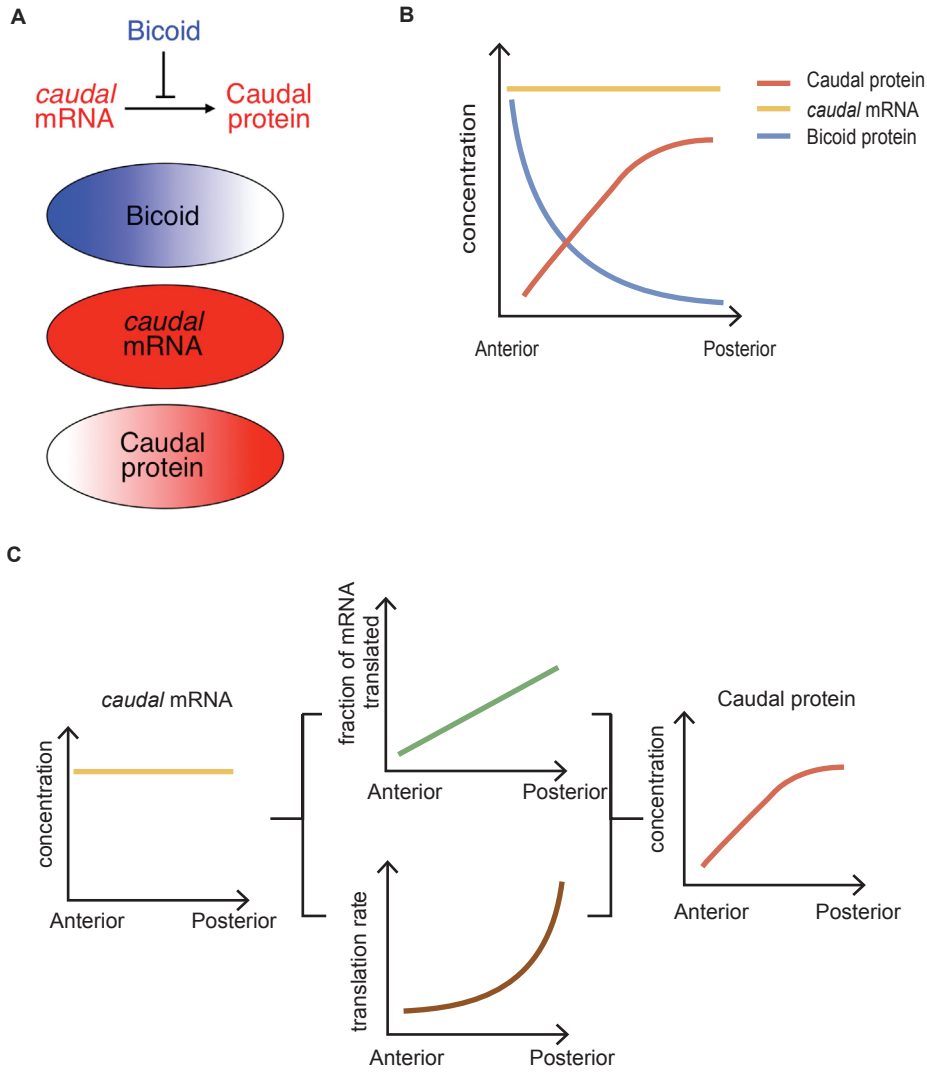

Figure 1.6: Translational regulation generates spatial protein gradients out of spatially uniform mRNA patterns. **(A)** Example of translational repression of *caudal* mRNA by Bicoid protein. Bicoid protein is expressed in an exponentially decaying gradient along the anterior-posterior axis of the embryo. *caudal* mRNA is supplied maternally and distributed uniformly along the anterior-posterior axis. Bicoid protein represses the translation of the *caudal* mRNA, thus generating the spatial gradient of the Caudal protein. (A) is adapted from (Rödel, Gilles, and Averof 2013). **(B)** A schematic figure of concentration profile along the anterior-posterior axis of the fly embryo for *caudal* mRNA, Bicoid protein, and Caudal protein. **(C)** There could be different ways to achieve translational repression. For example, the rate of translation, the fraction of mRNA molecules translated, or both could be under regulation by Bicoid to achieve the spatial gradient of the resulting Caudal protein. Note that, here, we have chosen arbitrary functional forms for the translation rate and the fractoin of mRNA molecules being translated for illustrative purposes.

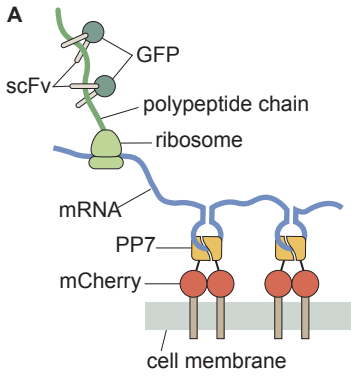

Figure 1.7: SunTags enable the visualization of nascent loci of translation and the quantificaiton of the number of nascent polypeptides. **(A)** Schematic of the SunTag:scFv-GFP to tag the nascent polypeptides and PP7:PCP to tether the mRNA to the cell membrane. This tethering is done for more extended tracking of the loci.

In order to dissect these molecular details, we need a tool to monitor and quantify translation dynamics at the single-ribosome level. To fluorescently label nascent polypeptides, we used the recently developed SunTag system. This system consists of repeated peptides (SunTag) inserted into the N-terminal of the protein of interest that can be bound by a single-chain variable fragment of an antibody (scFv) fused to fluorescent proteins (shown in Fig. 1.7 A) (Tanenbaum et al. 2014; Yan et al. 2016). Recent studies in the early fruit fly embryos using the SunTag reporter system reported on the spatio-temporal heterogeneities in translational dynamics, such as along the apical-basal axis (Dufourt et al. 2021) or along the anterior-posterior axis (Vinter et al. 2021). These studies have revealed that translational control is an uncharted area that could be under regulation by a group of unknown factors that could be associated with translation machinery and mRNA molecules.

Our initial goal was to implement the SunTag system in fruit fly embryos by adding the SunTag sequences upstream of the *hunchback* mRNA under the *hunchback* P2 minimal enhancer in a synthetic platform shown in Fig. 1.8A. Given that this mRNA pattern is very well characterized, we could then use it as a platform to dissect the translational pattern (Perry et al. 2012). We used scFv fused to sfGFP to quantify the SunTag upon translation and PCP-mCherry to tether the mRNA to the membrane as well as visualization of single mRNA molecules. Our preliminary data showed a promising result that demonstrated punctuated signals from the SunTag-scFv channel that recapitulate the step-like *hunchback* mRNA pattern along the anterior-posterior axis. The zoomed-in image in Figure 1.8 B clearly shows puncta of translation. As the next step, We sought to take the image this same construct over time. The zoomed-in movie on the *hunchback* boundary region again showed punctuated loci of translation as shown in Figure 1.8 C. We took two representative time traces from the

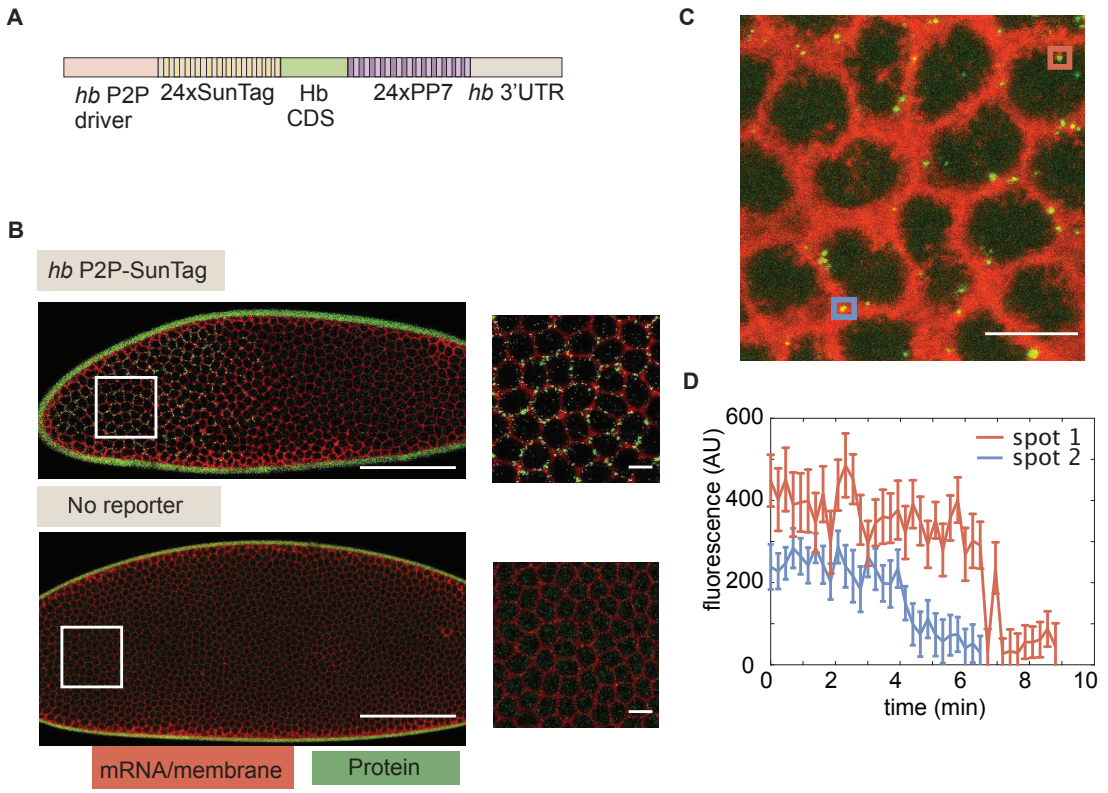

Figure 1.8: Proof-of-principle: *hunchback* P2P driven SunTag reporter recapitulates the step-like spatial pattern of *hunchback* mRNA and captures its translational dynamics. **(A)** Schematics of the reporter constructs. *hunchback* P2P driver followed by 24 repeats of SunTag, the *lacZ* coding sequence, 24 repeats of the PP7 loop, and the *hunchback* 3'UTR. The PP7 loops are used to tether the mRNA molecules to the membrane for a imaging. **(B)** Snapshots of embryos with or without the SunTag reporter shown in (A). (Top Left) A full embryo snapshot with the SunTag reporter and (Top Right) a zoomed-in image from the white squared region in the full embryo image. (Bottom Left) A full embryo snapshot without the SunTag reporter and (Bottom Right) a zoomed-in image from the white squared region in the full embryo image. Scale bars on the full embryo images represent $100\mu m$. Scale bars on the zoomed-in images represent $10\mu m$. **(C)** A zoomed-in image of the *hunchback*P2P driven SunTag construct with scFv-sfGFP and PCP-mCherry-CAAX. The green puncta represent the nascent loci of translation, and the membrane is marked with PCP-mCherry-CAAX. Blue and Red squared regions mark two nascent loci of translation whose temporal dynamics are shown in (D). **(D)** Time traces of the two loci of translation shown in (C) over 10 minutes in nuclear cycle 14.

same movie, marked with blue and red squares in Figure 1.8 C. These two time traces in Figure 1.8 D show the downregulation of translational activity over time in nuclear cycle 14, which is consistent with previous results Vinter et al. (2021).

Upon successful implementation of the SunTag approach, we aim to quantitatively dissect the differential translation dynamics from different 3'UTR sequences, such as *caudal* and maternal *hunchback*. Thus, we created synthetic reporter constructs with a gene cassette followed by different 3'UTR sequences. Careful characterization of these reporters remains as future work.

1.4 Preview of Chapter 5: Reaction-Diffusion models to connect transcriptional and translational pattern formation

So far, we have looked into different steps along the Central Dogma, from a set of transcription factors binding to a regulatory DNA sequence to drive transcription initiation, leading to the accumulation of mRNA molecules forming a gene expression pattern along the embryo's body axes, which then leads to a pattern of protein which acts onto the gene regulatory network. Classic developmental biology work has treated the patterns of transcripts and protein as almost equivalently. Only recently with the advent of techniques capable of measuring, for example, real-time translational regulation, was it proposed that mRNA and protein patterns are not always the same (Fig. 1.9 A) (Surkova et al. 2019). In this chapter, we connect quantitative measurements of transcription and translation under the reaction-diffusion modeling framework (Jaeger et al. 2004).

The reaction-diffusion model was proposed by Alan Turing to explain pattern formation in nature: patterns of stripes or spots emerging autonomously from homogeneous, uniform state (Turing 1952). A widespread application of the reaction-diffusion model in the fruit fly embryo is the so-called Synthesis, Degradation, and Diffusion (SDD) model (Gregor et al. 2007a). This model has been used to explain pattern formation of a maternal gene, *bicoid*.

Inspired by the SDD modeling framework, we wondered to which degree we could explain the protein pattern solely from the knowledge of mRNA patterns. Moreover, we wanted to challenge the SDD model by generating experimentally testable predictions. For example, the SDD model often assumes that parameters such as diffusion coefficients, synthesis or degradation rates for mRNA or protein are static (Gregor et al. 2007a). The SDD model works quite well with this simple assumption for systems with slow dynamics (on the order of a few hours) such as the spatial gradient formation of the maternal protein Bicoid (Gregor et al. 2007a). However, it remains unclear whether this assumption of parameters being static would hold for other genes with faster dynamics (on the order of tens of minutes) such as the pattern formation for zygotic proteins. By contrasting the predictions generated from this simple assumption with quantitative data, we can test this widespread assumption.

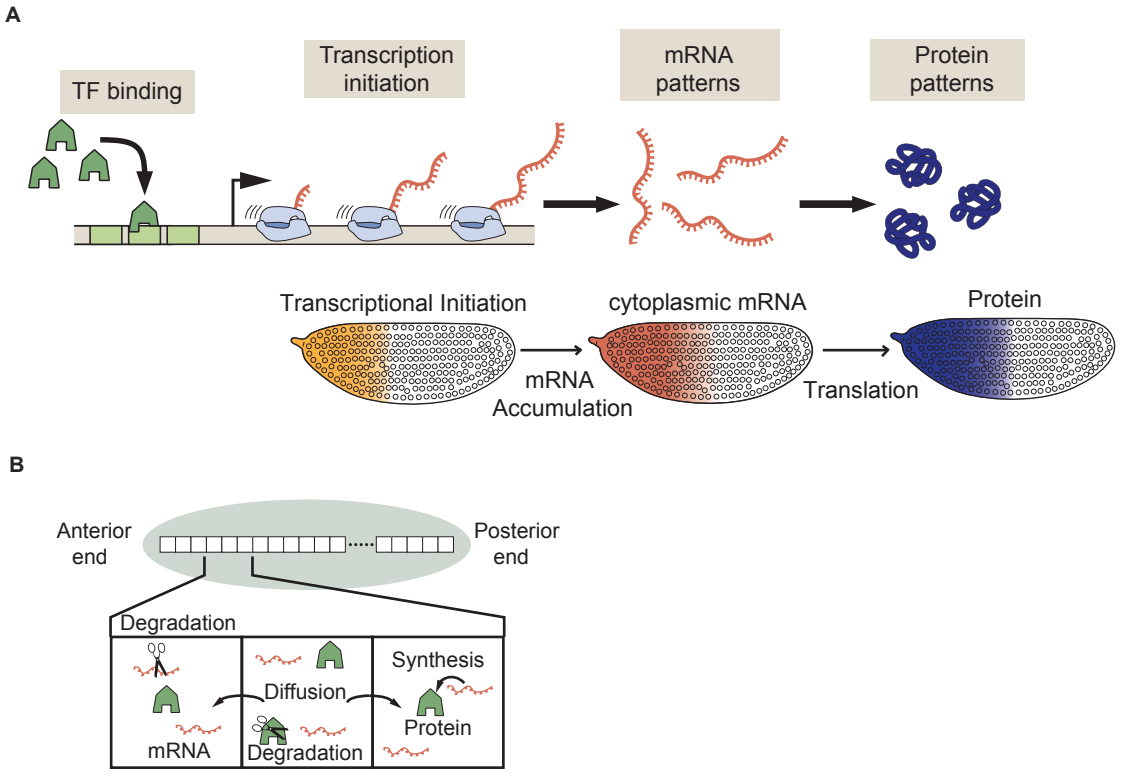

Figure 1.9: Conceptual framework to predict protein patterns from transcriptional initiation patterns using the reaction-diffusion model. **(A)** Schematic showing pattern formation along the Central Dogma. Pattern formation starts with a pattern of transcription initiation, leading to a pattern of cytoplasmic mRNA, then ultimately to a protein pattern. **(B)** A conceptual framework of the reaction-diffusion model. Reaction entails the synthesis and degradation of both mRNA and protein. Both mRNA and protein diffuse through the embryo. For simplicity, we assume that the embryo is one-dimensional along the anterior-posterior axis.

In the SDD model, there are parameters as follows: synthesis and degradation of both mRNA and protein as well as diffusion coefficients of both mRNA and protein. For simplicity, we assume that the embryo is one-dimensional along the anterior-posterior axis (Fig. 1.9 B). From previous measurements, some of these parameters were readily available, and if not, we could make educated guesses from the measurements from similar systems (Abu-Arish et al. 2010; Little, Tikhonov, and Gregor 2013) With these parameters at hand, we are ready to generate predictions of the protein pattern given the rate of transcription as a function of space and time.

To test the predictive power of our model, we built an experimental system where we can simultaneously measure the transcription dynamics and protein output in real-time. Specifically, we combined the MS2-MCP system with the LlamaTag in a synthetic gene cassette to simultaneously monitor the transcription and translation events (Fig. 1.10 A). With this reporter system, we could monitor the transcription initiation and output protein level in real-time as shown in Figure 1.10 B,C, and D.

By plugging in the rate of transcription from the MS2-MCP measurement, combined with the best estimates of the SDD model parameters, we could get a quantitative prediction for the protein level along space and time. This predicted protein pattern along the anterior-posterior axis can be directly compared with the measured protein pattern revealed by the LlamaTag.

As a proof of concept, we chose a set of parameters based of previous measurements for a variety of mRNA and protein species in the early fly embryo (Abu-Arish et al. 2010; Little, Tikhonov, and Gregor 2013). These parameters were used to generate the predicted protein patterns at different time points as shown in Figure 1.11 A. To contrast this prediction with the experimental data shown in Figure 1.11 B, we made a one-to-one comparison of the prediction and measurement at each position and time point (shown in Fig. 1.11 C). If our prediction is accurate, we should be able to get a perfect correlation between the prediction and the measurement, meaning the Pearson's correlation coefficient is one. However, as we investigated for all time points from our measurements acquired every minute, we could never observe this perfect correlation with any combinations of static parameters. We hypothesized that this might suggest that some parameters could change over time or space.

This hypothesis is in line with recent experimental results proposing that the translation of zygotic *hunchback* mRNA is under spatio-temporal regulation (Vinter et al. 2021). Further investigations are needed in both theoretical modeling and experimental measurements to dissect the spatiotemporal dependence of these biophysical parameters, which could potentially reveal the hidden knobs of gene regulation during development.

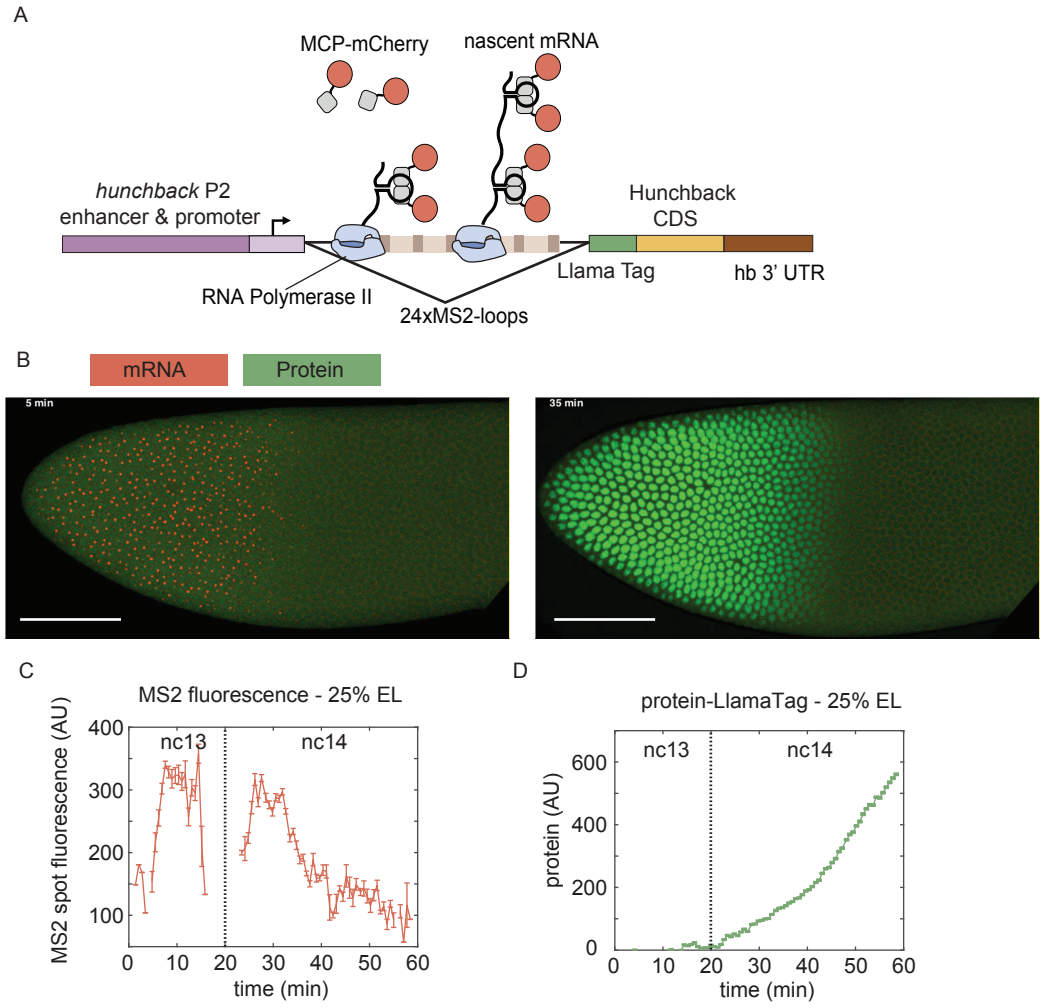

Figure 1.10: Experimental methods to simultaneously measure the transcriptional activity and protein patterns. **(A)** Schematics of our construct. *hunchback* P2P driver is followed by 24 repeats of the MS2 loop, a LlamaTag, *hunchback* coding sequence (CDS), and *hunchback* 3'UTR. **(B)** Two snapshots of an embryo expressing the reporter construct shown in (A). (Left) An embryo in early nucelar cycle 14. Transcriptional loci are shown as red spots. The protein pattern has not emerged yet. (Right) The same embryo as on the left, but in late nuclear cycle 14. Transcriptional activity has halted at this point, and the protein pattern emerged. The scale bar represents $100\mu m$. **(C)** MS2 spot fluorescence time trace averaged over 2.5% spatial bin at 25% of the embryo length (EL). **(D)**The LlamaTag protein nuclear fluorescence time trace averaged over 2.5% spatial bin at 25% of the embryo length.

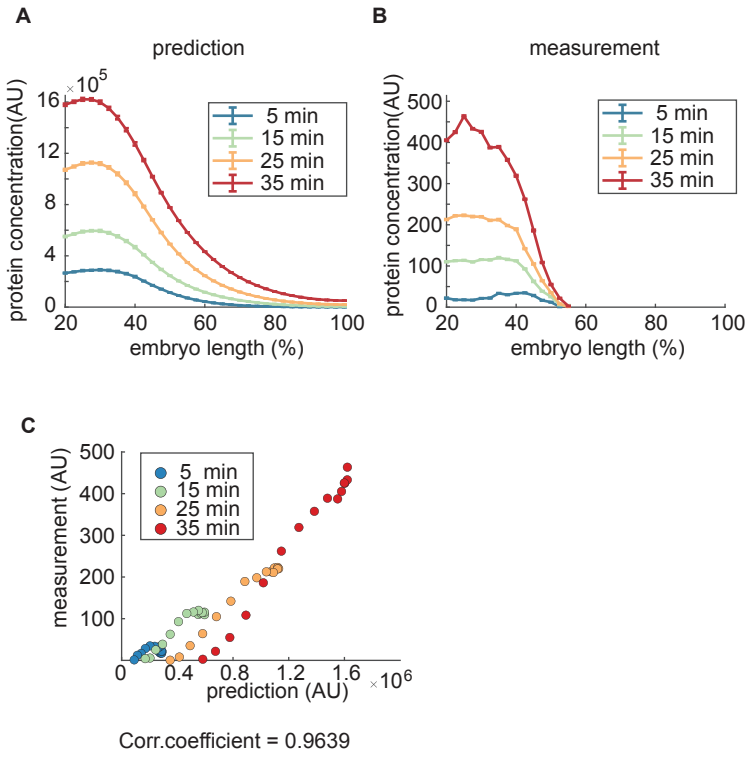

Figure 1.11: Comparison of predicted and experimentally measured protein patterns. **(A,B)** Using the Reaction-Diffusion model, we generated the predicted protein pattern for a set of parameters that are our best estimates. **A** Predicted protein level along the anterior-posterior axis during nuclear cycle 14, for four time points. **(B)** Measured protein level along the anterior-posterior axis during nuclear cycle 14, for the same four time points as in (A). **(C)** Comparison between prediction and measurement shown in (A). The Pearson's correlation coefficient gives an estimate of how good the prediction is.

Chapter 2

Predictive modeling for transcriptional repression in a synthetic developmental enhancer

1 Introduction

During embryonic development, transcription factors bind stretches of regulatory DNA termed enhancers to dictate the spatiotemporal dynamics of gene expression patterns that will lay out the future body plan of multicellular organisms (Small and Arnosti 2020; Spitz and Furlong 2012). One of the greatest challenges in quantitative developmental biology is to predict these patterns from knowledge of the number, placement, and affinity of transcription factor binding sites within enhancers. The early embryo of the fruit fly Drosophila melanogaster has become one of the main workhorses in this attempt to achieve a predictive understanding of cellular decision-making in development due to its well-characterized gene regulatory network and transcription factor binding motifs, and the ease with which its development can be quantified using live imaging (Garcia et al. 2020; Rivera et al. 2019; Small and Arnosti 2020).

Predictive understanding calls for the derivation of theoretical models that generate quantitative and experimentally testable predictions. Thermodynamic models based on equilibrium statistical mechanics have emerged as a widespread theoretical framework to achieve this goal (Ackers, Johnson, and Shea 1982; Bintu et al. 2005a,b; Bolouri and Davidson 2003; Eck et al. 2020; Fakhouri et al. 2010; Phillips et al. 2019; Sayal et al. 2016; Segal et al. 2008; Vilar and Leibler 2003). For instance, over the last decade, a dialogue between these thermodynamic models and experiments demonstrated the capacity to quantitatively predict bacterial transcriptional regulation from knowledge of the DNA regulatory architecture (Brewster et al. 2014; Garcia and Phillips 2011; Garcia et al. 2012; He et al. 2010; Sepulveda et al. 2016).

The predictive power of these models is evident when inferring model parameters from simple regulatory architectures (Boedicker, Garcia, and Phillips 2013; Boedicker et al. 2013;

Phillips et al. 2019; Razo-Mejia et al. 2018). Consider, for example, that RNA polymerase II (RNAP)—which we take as a proxy for the whole basal transcriptional machinery—binds to a promoter with a dissociation constant K_p. When RNAP is bound, transcription is initiated at a rate R (Fig. 1A). In the absence of any regulation, a thermodynamic model will only have K_p and R as its free parameters which can be experimentally determined by, for example, measuring mRNA distributions (Razo-Mejia et al. 2020). Now, we assume that the parameters K_p and R inferred in this step do not just enable a fit to the data, but that their values represent physical quantities that remain unaltered as more complex regulatory architectures are iteratively considered. As a result, when we consider the case where a single repressor molecule can bind, our model calls for only two new free parameters: a dissociation constant for repressor to its binding motif K_r, and a negative cooperativity between repressor and RNAP, ω_{rp}, that makes the recruitment of RNAP less favorable when the repressor is bound to its binding site (Fig. 1B). Once again, after determining K_r and ω_{rp} experimentally (Phillips et al. 2019), we consider the case where two repressors can bind simultaneously (Fig. 1C). If the repressors interact with RNAP independently of each other, then our model has no remaining free parameters such that we will have reached complete predictive power. However, protein-protein interactions between repressors could exist or even higher-order interactions giving rise to a repressor-repressor-RNAP ternary complex might be present. The extra complexity represented by these interactions would require yet another round of experimentation to quantify these interactions represented by ω_{rr} and ω_{rrp} in Figure 1C, respectively. Even after quantifying these parameters, predictive power might not be reached if, after adding yet another repressor binding site, a complex between all three repressors and RNAP can be formed (Fig. 1D).

While protein-protein cooperativity captured by ω_{rr} has been studied both in bacteria (Ackers, Johnson, and Shea 1982; Ptashne and Gann 2002) and eukaryotes (Fakhouri et al. 2010; Giniger and Ptashne 1988; Lebrecht et al. 2005; Ma et al. 1996; Parker et al. 2011; Sayal et al. 2016), the necessity of accounting for the higher-order interactions such as those described in our example by the ω_{rrp} and ω_{rrrp} terms had only been demonstrated in archeae (Peeters et al. 2013) and bacteria (Dodd et al. 2004). The need to invoke this higher-order cooperativity in eukaryotes only became apparent in the last few years (Biddle et al. 2020; Estrada et al. 2016a; Park et al. 2019). These higher-order cooperativities might be necessary in order to account for the complex interactions mediated by, for example, the recruitment of co-repressors (Courey and Jia 2001; Walrad, Hang, and Gergena 2011), mediator complex (Park et al. 2019), or any other element of the transcriptional machinery. As a result, while posing a challenge to reaching a parameter-free predictive understanding of transcriptional regulation, higher-order cooperativity provides an avenue for quantifying the complexity of the molecular processes underlying eukaryotic cellular decision-making.

In this paper, we sought to test whether an iterative and predictive approach, such as that outlined in Figure 1, was possible for transcriptional repression in the early embryo of the fruit fly Drosophila melanogaster or whether it is necessary to invoke higher-order cooperativities that challenge the reach of our predictive models as we add more complexity to the system. To make this possible, we engineered binding sites for the Runt repressor into

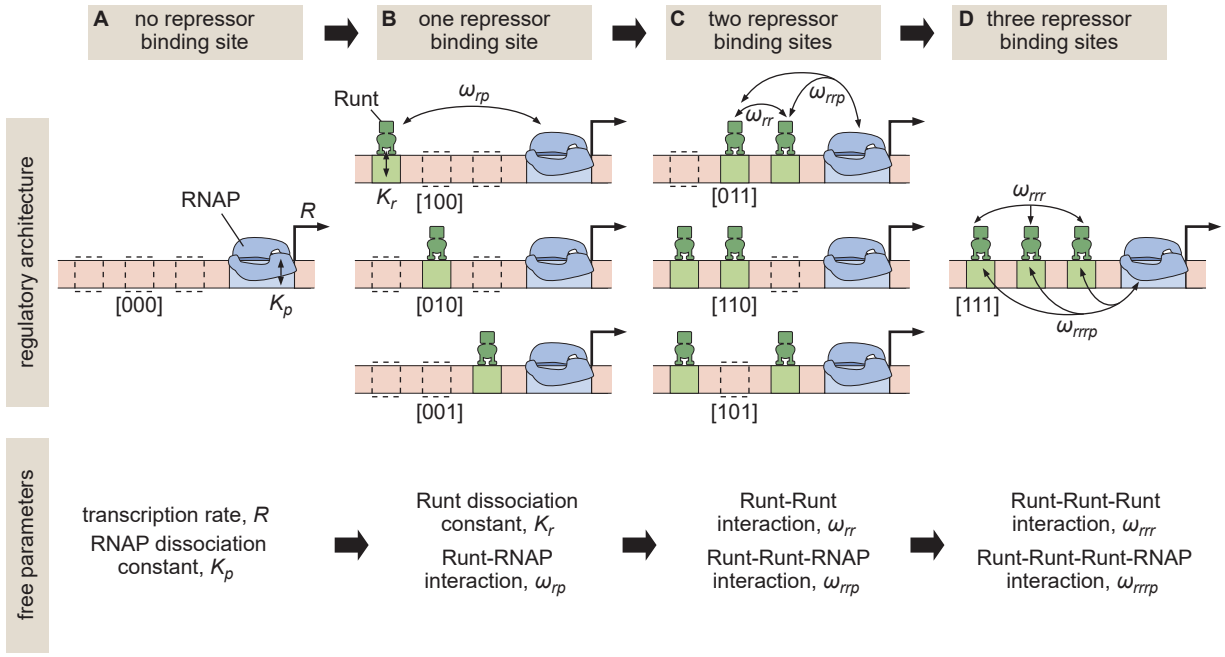

Figure 1: Building up predictive models of transcriptional repression. **(A)** In the absence of repressor binding, gene expression can be characterized by a dissociation constant between RNAP and the promoter K_p and the rate of transcription initiation when the promoter is bound by RNAP R. **(B)** In the presence of a single repressor binding site, models need to account for two additional parameters describing the repressor dissociation constant K_r and a repressor-RNAP interaction term ω_{rp}. **(C)** For two-repressor architectures, parameters accounting for repressor-repressor interactions ω_{rr} and for interactions giving rise to a repressor-repressor-RNAP complex could also have to be incorporated. **(D)** For the case of three repressor binding sites, additional parameters ω_{rrr} and ω_{rrrp} capturing the higher-order cooperativity between three repressor molecules and between three Runt molecules and RNAP, respectively, could be necessary. Note the nomenclature shown below each construct, which indicates which Runt binding sites are present in each construct.

the Bicoid-activated *hunchback* P2 minimal enhancer. We systematically varied the number and placement of Runt binding sites within this enhancer (Chen et al. 2012) in order to determine whether model fits to real-time transcriptional measurements from the enhancer constructs containing only one-Runt binding site could accurately predict repression in two- and three-Runt binding site constructs (Fig. 1A and B). We found that a thermodynamic model can recapitulate all our data. However, we also discovered that, while the model could describe repression by a single Runt repressor, protein-protein and higher-order cooperativities had to be invoked in order to quantitatively account for regulation by two or more repressor molecules. While these higher-order cooperativities limit the iterative bottom-up discourse between theory and experiment that has been successful in bacteria (Phillips, Kondev, and Theriot 2009), they also provide a concrete theoretical framework for quantifying the complexities behind eukaryotic transcriptional control, and calling for the development of new theories and experiments specifically conceived to uncover the the molecular underpinnings of this complexity.

2 Results

Predicting transcription rate using a thermodynamic model of Bicoid activation and Runt repression

We built a predictive model of Runt repression on the Bicoid-activated *hunchback* P2 enhancer using the thermodynamic model framework (Bintu et al. 2005a,b; Phillips et al. 2019) with the goal of predicting the rate of transcription initiation as a function of input transcription factor concentration, and the number and placement of Runt repressor binding sites. Our model rests on the "occupancy hypothesis" that states that the rate of mRNA production, $d[mRNA]/dt$, is proportional to the probability of the promoter being bound by RNA polymerase II (RNAP), p_{bound}, such that

$$\frac{d\,[mRNA]}{dt} = R\; p_{bound}, \tag{1}$$

where R is the rate of mRNA production when the promoter is occupied by RNAP. Note that, throughout this study, we treat the rate of transcription initiation and the rate of RNAP loading interchangeably.

To generate intuition, we start by modeling the case of *hunchback* P2 with one Runt binding site. Figure 2A illustrates the possible states the system can be found in. Each state has an associated statistical weight which can be calculated as prescribed by equilibrium statistical mechanics (Bintu et al. 2005a,b). Here, we assume that there are six Bicoid binding sites with the same dissociation constant given by K_b, one Runt binding site with a dissociation constant specified by K_r, and a promoter with a dissociation constant for RNAP prescribed by K_p. In the absence of Runt, we consider four states as shown in the top two rows of Figure 2A. Here, we assume that Bicoid-Bicoid cooperativity is so strong that the enhancer

can either be unoccupied or completely bound by Bicoid molecules (Gregor et al. 2007b; Park et al. 2019). Further, we consider an interaction between Bicoid and RNAP given by ω_{bp}. For simplicity, we use the dimensionless parameters $b = [Bicoid]/K_b$, $r = [Runt]/K_r$ and $p = [RNAP]/K_p$. These assumptions lead to a functional form reminiscent of a Hill function that explains the sharp step-like expression pattern along the embryo's anterior-posterior axis of the *hunchback* gene (Driever and Nusslein-Volhard 1988, 1989; Gregor et al. 2007b; Park et al. 2019). A full thermodynamic model in which we do not make this assumption of high Bicoid-Bicoid cooperativity is discussed in detail in Section S1 and Section S2 .

The molecular mechanism by which Runt downregulates transcription of its target genes remains unclear (Chen et al. 2012; Hang and Gergen 2017; Koromila and Stathopoulos 2017, 2019). Here, we assume the so-called "direct repression" model (Gray, Szymanski, and Levine 1994) that posits that Runt operates by inhibiting RNAP binding to the promoter through a direct Runt-RNAP interaction term given by $\omega_{rp} < 1$ independently of Bicoid. As a result, in the presence of Runt, we consider four additional states as shown in the bottom two rows of Figure 2A. Other potential mechanisms of Runt repression are further discussed in Supplementary Section S5), where we also show that the choice of specific mechanism does not change our conclusions.

Given these assumptions, we arrive at the microstates and corresponding statistical weights shown in Figure 2A. The probability of finding RNAP bound to the promoter, p_{bound}, is calculated by dividing the sum of all statistical weights featuring RNAP by the sum of the weights of all possible microstates. The calculation of p_{bound} combined with Equation 1 leads to the expression

$$Rate = R\, p_{bound} = R\, \frac{p + b^6\, p\, \omega_{bp} + r\, p\, \omega_{rp} + b^6\, r\, p\, \omega_{bp}\, \omega_{rp}}{1 + b^6 + r + b^6\, r + p + b^6\, p\, \omega_{bp} + r\, p\, \omega_{rp} + b^6\, r\, p\, \omega_{bp}\, \omega_{rp}}, \quad (2)$$

which makes it possible to predict the output rate of mRNA production as a function of the input concentrations of Bicoid and Runt (Fig. 2B). With this theoretical framework in hand, we experimentally tested the predictions of this model.

Measuring transcriptional input-output to test model predictions

The transcriptional input-output function in Figure 2B indicates that, in order to predict the rate of RNAP loading and to test our theoretical model, we need to first measure the concentration of the input Bicoid and Runt transcription factors. In order to quantify the concentration profile of Bicoid, we used an established eGFP-Bicoid line (Gregor et al. 2007b) and measured mean Bicoid nuclear concentration dynamics along the anterior-posterior axis of the embryo over nuclear cycles 13 and 14 (nc13 and nc14, respectively) as shown in Movie S1 (Eck et al. 2020). An example snapshot and time trace of Bicoid nuclear concentration dynamics at 40% of the embryo length appear in Figure 3A and B.

Quantification of the Runt concentration using standard fluorescent protein fusions is not possible due to the slow maturation times of these proteins (Bothma et al. 2018). We therefore measured Runt concentration dynamics using our recently developed LlamaTags,

which are devoid of such maturation dynamics artifacts (Bothma et al. 2018). Specifically, we generated a new fly line harboring a fusion of a LlamaTag against eGFP to the endogenous runt gene using CRISPR/Cas9-mediated homology-directed repair (Materials and Methods; **??**).

Using this LlamaTag fusion, we measured the mean Runt nuclear fluorescence along the anterior-posterior axis of the embryo over nc13 and nc14 (Materials and Methods; Figure 3B; Movie S2). As expected due to the location of the runt gene on the X chromosome (Lott et al. 2011), there is a sex dependence in the nuclear concentration levels in nc13, with males displaying lower Runt levels than females; this difference is compensated by early nc14 (Fig. 3C,D). As a result, for ease of analysis, we focused subsequent quantitative dissection on nc14.

We used the measured input protein concentration profiles to predict the output transcription rate. To make this possible, we invoked previous observations stating that the concentration dynamics of input transcription factors does not significantly affect the initial rate of RNAP loading (Eck et al. 2020; Garcia et al. 2013b). As a result, we decided to use the time-averaged concentration dynamics of Bicoid and Runt over a time window spanning 5 min after the 13th anaphase to 10 min after this anaphase (gray shaded region in Fig. 3B and D) as inputs to our model, resulting in static spatial concentration profiles shown in Figure 3E. We then used these time-averaged concentration profiles of input transcription factors to calculate the time-averaged rate of transcription initiation over the same time window. In the Supplementary Information Section S3 we compare this methodology with one that acknowledges input transcription factor concentration dynamics and show that the prediction stemming from both approaches leads to equivalent theoretical predictions. Notably, the time-averaged rate of transcription predicted by the dynamic inputs was similar to the rate of transcription predicted by the static inputs.

Along the anterior-posterior axis of the embryo, the measured Bicoid and Runt concentration profiles define a trajectory through the input-output function (Fig. 2B). Given a set of parameters, this trajectory predicts the initial rate of RNAP loading. This quantitative prediction can be directly compared with experimentally measured transcription initiation rates. For example, given the concentration profiles shown in Figure 3E, we calculate the RNAP loading rate as a function of the position along the embryo for different values of the Runt-RNAP interaction, captured by ω_{rp} (Fig. 3F). As expected, we predict that the rate of transcription decreases as ω_{rp}, describing Runt-RNAP cooperativity, decreases.

Next, we sought to experimentally test these predictions by measuring the rate of RNAP loading using the MS2 system (Bertrand et al. 1998; Garcia et al. 2013b; Lucas et al. 2013). Here, we inserted 24 repeats of the MS2 loop sequence following the *hunchback* P2 enhancer and *even-skipped* promoter in our reporter construct, which leads to the fluorescent labeling of sites of active transcription in living embryos (Fig. 3G and H; Movie S3). The fluorescence intensity of each MS2 spot is proportional to the number of actively transcribing RNAP molecules (Garcia et al. 2013b). In order to quantify the transcriptional activity reported by MS2, we measured the mean MS2 spot fluorescence over nuclei in a narrow spatial window (Fig. 3I (Eck et al. 2020; Garcia et al. 2013b). To measure the initial rate of RNAP loading, we

obtained the slope of the initial rise in the number of actively transcribing RNAP molecules over the same time window used to average input transcription factor concentration (Fig. 3I, brown line). The resulting RNAP loading rate plotted over the anterior-posterior axis is in qualitative agreement with the classic pattern driven by the *hunchback* P2 minimal enhancer (Fig. 3J; **???**).

While we chose the initial rate of transcription as the experimental measurable to confront against our model predictions, the MS2 technique can also report on other dynamical features of transcription such as the time window over which transcription occurs and the fraction of loci that engage in transcription at any point over the nuclear cycle. While these two quantities have been shown to be relevant in shaping gene expression patterns in other regulatory contexts (Dufourt et al. 2018; Eck et al. 2020; Garcia et al. 2013b; Lammers et al. 2020; Reimer et al. 2021), we found that the transcription time window was not significantly regulated in the presence of Runt. As described in Section S8 , we did find some modulation of the fraction of transcriptionally engaged loci for a subset of our synthetic enhancer constructs but, as we could not detect a clear trend in how this fraction of active loci was modulated, we did not pursue a theoretical dissection of the control of this quantity by Runt.

Enhancer sequence dictates unrepressed transcription rates by determining RNAP-promoter interactions

A major assumption of our theoretical approach is that the model parameters obtained from simple regulatory architectures can be used as inputs for more complex constructs. For instance, we assume that the Runt-independent model parameters for Bicoid and RNAP action—K_b, ω_{bp}, p and R (Fig. 2A)—are conserved for all constructs containing Runt binding sites regardless of their number and placement in the enhancer. If model parameters can be shared across constructs, then our model should predict the same profile for the rate of transcription across all synthetic enhancer constructs.

To test this assumption, we measured the initial rate of RNAP loading in all of our reporter constructs, in *runt* null embryos (Materials and Methods). Notably, unrepressed transcription rates varied significantly across synthetic enhancers (Fig. 5A). For example, despite no Runt being present, the [001] construct had almost twice the unrepressed rate of [000] .

This large construct-to-construct variability in unrepressed transcription rates likely originates from the Runt binding site sequences interfering with some combination of Bicoid and RNAP function. To uncover the mechanistic effect of these Runt binding sites sequences on unrepressed activity, we sought to determine which parameters in our thermodynamic model varied across constructs. In the absence of Runt repressor, only four states remain corresponding to the two top rows of Figure 2A. In this limit, the predicted rate of transcription is given by

$$Rate = R\ \frac{p + b^6\ p\ \omega_{bp}}{1 + p + b^6 + b^6\ p\ \omega_{bp}}, \tag{3}$$

where we have invoked the same parameters as in Equation 2.

To obtain the model parameters for each construct measured in Figure 5A, we used the Bayesian inference technique of Markov Chain Monte Carlo (MCMC) sampling that has been widely used for inferring the biophysical parameters from theoretical models (**???**; Supplementary Section S4). A representative comparison of the MCMC fit to the experimental data reveals good agreement between theory and experiment (Fig. 5B). MCMC sampling also gives the distribution of the posterior probability for each parameter as well as their cross-correlation (Fig. 5C). These corner plots reveal relatively unimodal posterior distributions, suggesting that a unique set of parameters can explain the data.

Note that, while the Bicoid dissociation constant K_b and the Bicoid-RNAP interaction term ω_{bp} remain largely unchanged regardless of enhancer sequence, there is considerable variability in the inferred mean RNAP-dependent parameters p and R (Fig. 5D). This variability can be further quantified by examining the coefficient of variation,

$$CV = \frac{\sigma}{\mu}, \tag{4}$$

where σ and μ are the standard deviation and the mean of each parameter, respectively, calculated over all constructs. The coefficients of variation for the RNAP and promoter-dependent parameters are much higher than those for Bicoid-dependent parameters ($\approx 40\%$ versus $< 10\%$; Fig. 5E). This suggests that the variability in unrepressed transcription rates due to the presence of Runt binding sites is due to differences in the behavior of RNAP at the promoter rather than differences in Bicoid binding or activation being. As a result, as we consider increasingly more complex regulatory architectures, each construct will necessitate its own specific Bicoid- and RNAP-dependent parameters as inferred in Figure 5D. However, we will conserve Runt-dependent parameters as we consider increasingly more complex constructs featuring more Runt binding sites.

The thermodynamic model recapitulates repression by one Runt binding site

Next, we asked whether our model recapitulates gene expression for the *hunchback* P2 enhancer with a one-Runt binding site in the presence of Runt repressor as predicted by Equation 2. We posited that, since the binding site sequence remains unaltered throughout our constructs (Fig. S9), the value of the Runt dissociation constant K_r would also remain unchanged across these enhancers regardless of Runt binding site position; however, we assumed that, as the distance between Runt and the promoter varied, so could the Runt-RNAP interaction term ω_{rp}.

We measured the initial rate of transcription along the embryo for all our constructs containing one Runt binding site in the presence of Runt protein. We then used MCMC sampling to infer the Runt-dependent parameters K_r and ω_{rp} for each of these constructs while retaining the mean values of Runt-independent parameters (K_b, ω_{bp}, p, and R) obtained from the experiments performed in the absence of Runt (Fig. 5). The resulting MCMC fits

show significant agreement with the experimental data (Fig. 6A), confirming that, within our model, the same dissociation constant K_r can be used for all Runt binding sites regardless of their position within the enhancer. Further, the corner plot yielded a unimodal distribution of posterior probability of the inferred parameters (Fig. 6B), indicating the existence of a unique set of most-likely model parameters.

The observed trend in the Runt-RNAP interaction captured by ω_{rp} qualitatively agrees with the "direct repression" model. Specifically, because the model assumes that Runt interacts directly with RNAP, it predicts that, the farther apart Runt and the promoter are, the lower this interaction should be (Gray, Szymanski, and Levine 1994). In agreement with this prediction, the mean value of ω_{rp} obtained from our fits changes from high repression ($\omega_{rp} \approx 0.1$) in the [001] construct to almost no repression ($\omega_{rp} \approx 1$) in the [100] construct as the Runt site is moved away from the promoter (Fig. 6C). Thus, the direct repression model recapitulates repression by a single Runt molecule using the the same dissociation constant regardless of Runt binding site position, and displays the expected dependence of the Runt-RNAP interaction term on the distance between these two molecules.

Predicting repression by two-Runt binding sites requires both Runt-Runt and Runt-Runt-RNAP higher-order cooperativity

Could the parameters inferred in the preceding section be used to accurately predict repression in the presence of two Runt binding sites? An extra Runt binding site enables new protein-protein interactions between Runt molecules and RNAP (Fig. 7A). First, we considered individual Runt-RNAP interaction terms, ω_{rp1} and ω_{rp2}, whose values were already inferred from the one-Runt binding site constructs as $\omega_{rp_{[001]}}$, $\omega_{rp_{[010]}}$, *and* $\omega_{rp_{[100]}}$ (Fig. 6D). Second, we considered protein-protein interactions (positive or negative) between two Runt molecules, ω_{rr}. Third, following recent studies of Bicoid activation of the *hunchback* P2 minimal enhancer (Estrada et al. 2016b; Park et al. 2019), we also posited the existence of simultaneous Runt-Runt-RNAP higher-order cooperativity ω_{rrp}. Given these different cooperativities, and as shown in detail in Figure S16B, the predicted rate of transcription is

$$\begin{aligned} Rate =& R\left(p + b^6\ p\ \omega_{bp} + r\ p\ (\omega_{rp1} + \omega_{rp2}) + r^2\ p\ \omega_{rp1}\omega_{rp2}\omega_{rr}\omega_{rrp} + b^6\ r\ p\ \omega_{bp}\ (\omega_{rp1} + \omega_{rp2}) + \right. \\ & \left. b^6\ r^2\ p\ \omega_{bp}\omega_{rp1}\omega_{rp2}\omega_{rr}\omega_{rrp}\right)\left(1 + b^6\ (1 + 2r + p\ \omega_{bp}) + 2r + p + r\ p\ (\omega_{rp1} + \omega_{rp2}) + r^2\ (\omega_{rr}\right. \\ & \left. + p\ \omega_{rp1}\omega_{rp2}\omega_{rr}\omega_{rrp}) + b^6\ r\ p\ \omega_{bp}\ (\omega_{rp1} + \omega_{rp2}) + b^6\ r^2\ \omega_{rr} + b^6\ r^2\ p\ \omega_{bp}\omega_{rp1}\omega_{rp2}\omega_{rr}\omega_{rrp}\right)^{-1}. \end{aligned} \tag{5}$$

Despite the complexity of this equation, note that its only free parameters are the cooperativity parameters ω_{rr} and ω_{rrp}. As a result, we sought to determine whether the Runt-RNAP cooperativity terms, ω_{rp1} and ω_{rp2}, are sufficient to predict repression by two Runt molecules, or whether the cooperativities given by ω_{rr} and ω_{rrp} also need to be invoked.

Consider the simplest case where two Runt molecules bind and interact with RNAP independently from each other. Here, $\omega_{rr} = 1$, and $\omega_{rrp} = 1$. This model has no free

parameters; all parameters have already been determined by the inferences performed on Runt null datasets and one-Runt binding site constructs (Fig. 5 and Fig. 6, respectively). While there was some agreement between the model and the data for the [101] construct (Fig. 7B, center), significant deviations from the prediction occurred for the other two constructs. These deviations ranged from less repression than predicted for [011] (Fig. 7B, left) to more repression than predicted for [110] (Fig. 7B, right). Thus, this simple model of Runt independent repression is not supported by the experimental data, suggesting additional regulatory interactions between the Runt molecules and RNAP.

A first alternative to the independent repression model is the consideration of Runt-Runt cooperative interactions such as those that characterize many transcription factors (Estrada et al. 2016a; He et al. 2010; Park et al. 2019; Ptashne 2004; Segal et al. 2008). However, adding a Runt-Runt cooperativity term, ω_{rr}, was insufficient to account for the observed regulatory behavior (Fig. 7C; Fig. S13 more thoroughly analyzes this discrepancy). A second alternative consists in incorporating a Runt-Runt-RNAP higher-order cooperativity term, ω_{rrp}. While the best MCMC fits revealed significant improvements in predictive power, important deviations still existed for the [110] construct (Fig. 7D, right; Fig. S15 more thoroughly analyzes the MCMC inference results).

Not surprisingly, given the agreement of the higher-order cooperativity model with the data for the [011] and [101] constructs (Fig. 7D, left and center), this agreement persisted when both Runt-Runt cooperativity and Runt-Runt-RNAP higher-order cooperativity were considered (Fig. 7E, left and center). However, including these two cooperativities also significantly improved the ability of model at explaining the [110] experimental data (Fig. 7E, right). Thus, while higher-order cooperativity is the main interaction necessary to quantitatively describe repression by two Runt repressors, pairwise cooperativity also needs to be invoked. This conclusion is supported by our MCMC sampling: posterior distributions for the Runt-Runt cooperativity term are not well constrained for the [011] or [101] constructs, whereas Runt-Runt-RNAP higher-order cooperativity is constrained very well across all constructs (Fig. S16D; Fig. S16 more thoroughly analyzes the MCMC inference results). As a result, accounting for both pairwise and higher order cooperativity is necessary for the model to explain the observed rate of RNAP loading of all three constructs.

The higher-order cooperativity revealed by our analysis can lead to more or less repression than predicted by the independent repression model, motivating us to determine the magnitude of this cooperativity across constructs. To make this possible, we inferred the magnitude of the Runt-Runt cooperativity ω_{rr} and the Runt-Runt-RNAP higher-order cooperativity ω_{rrp}. As shown in Figure 7F, depending on the spatial arrangement of Runt binding sites, the Runt-Runt-RNAP higher-order cooperativity term ω_{rrp} can be below or above 1. Note that, in doing these fits, we first set the Runt-Runt cooperativity, ω_{rr}, values for [011] and [101] to 1 because, as we had demonstrated in Figure 7D, only the higher-order Runt-Runt-RNAP cooperativity was necessary. Thus, different placements of Runt molecules on the enhancer lead to distinct higher-order interactions with RNAP which, in turn, can result in less or more repression than predicted by a model where Runt molecules act independently of each other.

Repression by three-Runt binding sites also requires higher-order cooperativity

Building on our success in deploying thermodynamic models to explain repression by one- and two-Runt binding sites, we investigated repression by three-Runt binding sites. First, we accounted for pairwise interactions between Runt and RNAP, which were inferred from measurements of the one-Runt binding site constructs (Fig. 1B), yielding $\omega_{rp_{[001]}}$, $\omega_{rp_{[010]}}$, and $\omega_{rp_{[100]}}$ from [001], [010], and [100]. Second, we considered pairwise protein-protein interactions between Runt molecules (Fig. 1C), which were inferred from the two-Runt binding sites constructs through the parameters $\omega_{rr_{[011]}}$, $\omega_{rr_{[101]}}$, and $\omega_{rr_{[110]}}$. Finally, we incorporated Runt-Runt-RNAP higher-order cooperativity acquired from the two-Runt binding sites constructs (Fig. 1C) captured by $\omega_{rrp_{[011]}}$, $\omega_{rrp_{[101]}}$, and $\omega_{rrp_{[110]}}$. we tested our model predictions using a similar scheme to that described in the previous section: we generated a parameter-free prediction for the initial rate of transcription by using the inferred parameters from the one- and two-Runt binding sites constructs, including the pairwise and higher-order interactions described above.

Figure 8A shows the resulting parameter-free prediction. As seen in the figure, our model could not qualitatively recapitulate the experimental data as it predicted too much repression. Such disagreement suggests that additional regulatory interactions are at play. Building on the need for higher-order cooperativity in the two-Runt binding site case, we propose the existence of higher order cooperativities necessary to describe regulation by three Runt molecules—Runt-Runt-Runt higher-order cooperativity, ω_{rrr} and Runt-Runt-Runt-RNAP higher-order cooperativity, ω_{rrrp} (Fig. 1D). The resulting expression for the predicted rate of transcription in the presence of all these sources of cooperativity is shown in Equation **??** in Section S2 . Importantly, we did not try to find the optimal value for these higher-order coopratividies through fitting. Instead, our objective was to determine whether the addition of any of these new parameters was sufficient to explain our data. When including only a Runt-Runt-Runt-RNAP higher-order cooperativity parameter of $\omega_{rrrp} = 2300$, our model recapitulated the experimental data (Fig. 8B). Thus, our results further support the view in which the addition of Runt repressor binding motifs in an enhancer cannot be explained by a simple additive interaction between each bound repressor. Rather, their combinatorial effect must be taken into account.

(A)

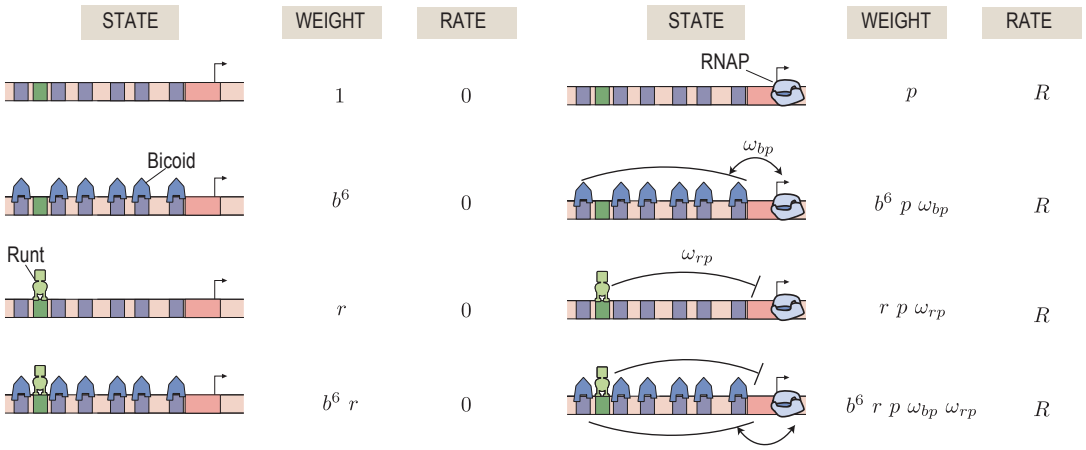

(B)

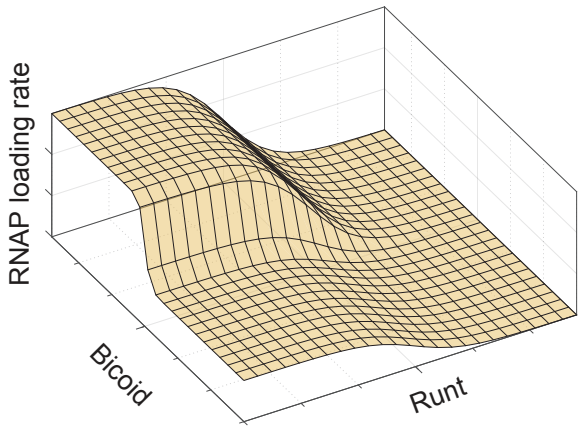

Figure 2: Thermodynamic model of transcriptional regulation by Bicoid activator and Runt repressor. **(A)** States and statistical weights for the regulation of *hunchback* P2 with one Runt binding site in the limit of strong Bicoid-Bicoid cooperativity. Here, we use the dimensionless parameters $b = [Bicoid]/K_b$, $r = [Runt]/K_r$, and $p = [RNAP]/K_p$, where K_b, K_r, and K_p are the dissociation constants of Bicoid, Runt, and RNAP, respectively. ω_{bp} represents the cooperativity between Bicoid and RNAP, ω_{rp} captures the cooperativity between Runt and RNAP, and R represents the rate of transcription when the promoter is occupied by RNAP. The top two rows correspond to states where only Bicoid and RNAP act, while the bottom two rows represent repression by Runt. **(B)** Representative prediction of RNAP loading rate as a function of Bicoid and Runt concentrations for $\omega_{bp} = 3, \omega_{rp} = 0.001, p = 0.001, R = 1(AU/min)$.

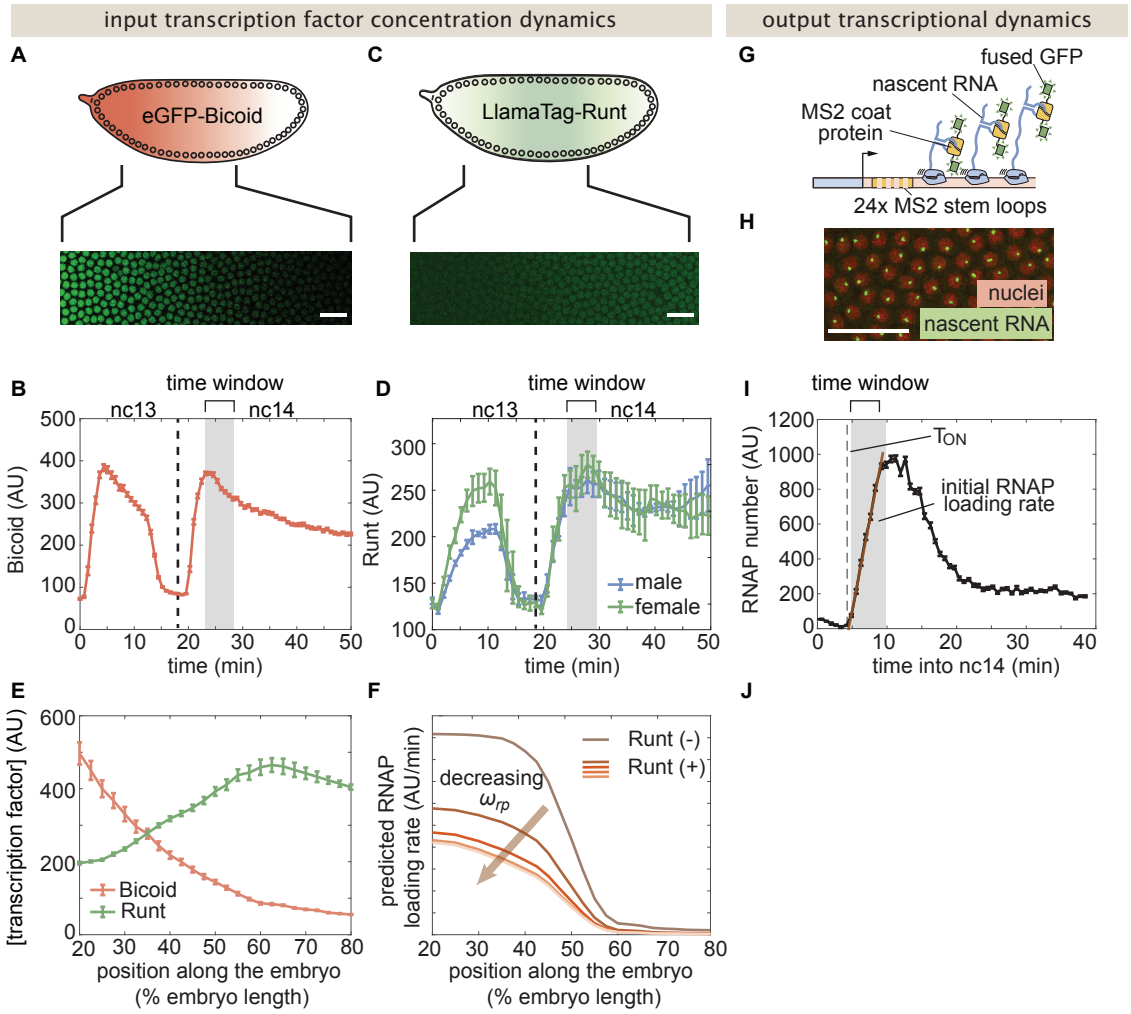

Figure 3: Measurement of input transcription factor concentrations and output rate of transcription to test model predictions. See caption in the next page.

Figure 4: Measurement of input transcription factor concentrations and output rate of transcription to test model predictions. **(A)** Snapshot of an embryo expressing eGFP-Bicoid spanning 20-60% of the embryo length. (For a full time-lapse movie, see Movie S1.) **(B)** Bicoid nuclear fluorescence dynamics taken at 40% of the embryo. **(C)** Snapshot of an embryo expressing eGFP:LlamaTag-Runt spanning 20-60% of the embryo length. (For a full time-lapse movie, see Movie S2.) **(D)** Runt nuclear concentration dynamics in males and females. **(E)** Measured transcription factor concentration profiles along the anterior-posterior axis of the embryo. The concentration profiles are averaged over the gray shaded regions shown in (B) and (D) which corresponds to a time window between 5 and 10 minutes into nc14. **(F)** Predicted RNAP loading rate for *hunchback* P2 with one Runt binding site over the anterior-posterior axis generated for a reasonable set of model parameters $K_b = 30$ AU, $K_r = 100$ AU, $\omega_{bp} = 100$, $p = 0.001$, and $R = 1$ AU/min for varying values of the Runt-RNAP interaction term $\omega_{rp} = [10^{-2}, 1]$. **(G)** Schematic of the MS2 system where 24 repeats of the MS2 loop sequence are inserted downstream of the promoter followed by the *lacZ* gene. The MS2 coat protein (MCP) fused to GFP binds the MS2 loops. **(H)** Example snapshot of an embryo expressing MCP-GFP and Histone-RFP. Green spots to active transcriptional loci and red circles correspond to nuclei. Spot intensities are proportional to the number of actively transcribing RNAP molecules. **(I)** Representative MS2 fluorescence averaged over a narrow window (2.5% of the embryo length) along the anterior-posterior axis of the embryo. The initial rate of RNAP loading was obtained by fitting a line (brown) to the initial rise of the data. **(J)** Measured initial rate of RNAP loading (over a spatial bin of 2.5% of the embryo length) across the anterior-posterior axis of the embryo, from the *hunchback* P2 enhancer. (B, D, E, and J, error bars represent standard error of the mean over ≥ 3 embryos; I, error bars represent standard error of the mean over the spatial averaging corresponding to roughly ten nuclei; A, C, and H, white scale bars represent 20 μm.)

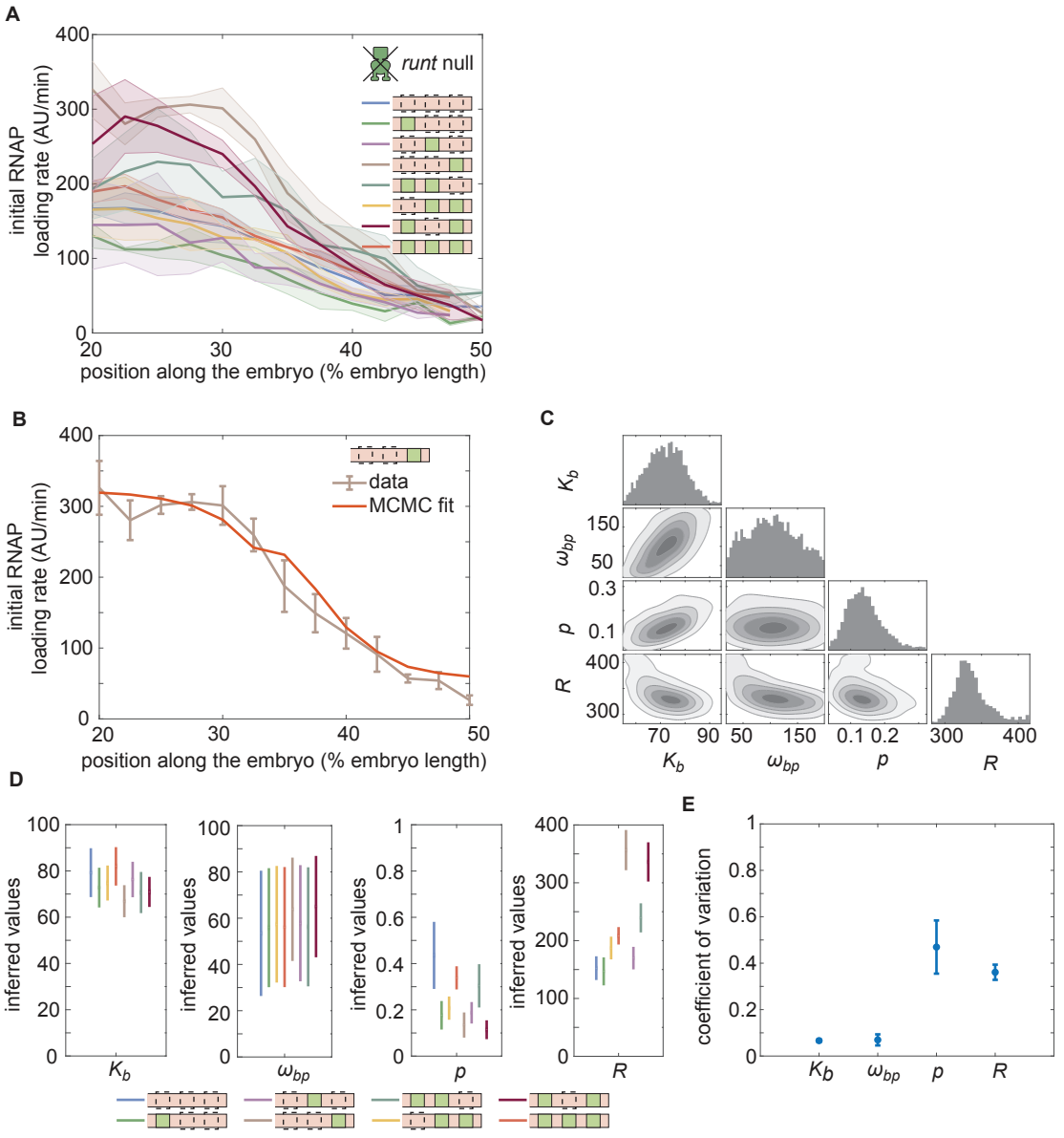

Figure 5: Enchancer-to-enhancer variability in the unrepressed transcription level stems from unique RNAP-dependent parameters. **(A)** Measured initial rates of RNAP loading across the anterior-posterior axis of the embryo for all synthetic enhancer constructs in the *absence* of Runt protein. **(B)** Representative best MCMC fit and **(C)** associated corner plot for the [001] construct in the runt null background. **(D)** Inferred model parameters for all synthetic enhancers in the absence of Runt repressor. **(E)** Coefficient of variation of inferred parameters. (B, C, error bars represent standard error of the mean over ¿3 embryos; E, error bars represent standard deviations calculated from the MCMC posterior chains; F, error bars are calculated by propagating the standard deviation of individual parameters from their MCMC chains.)

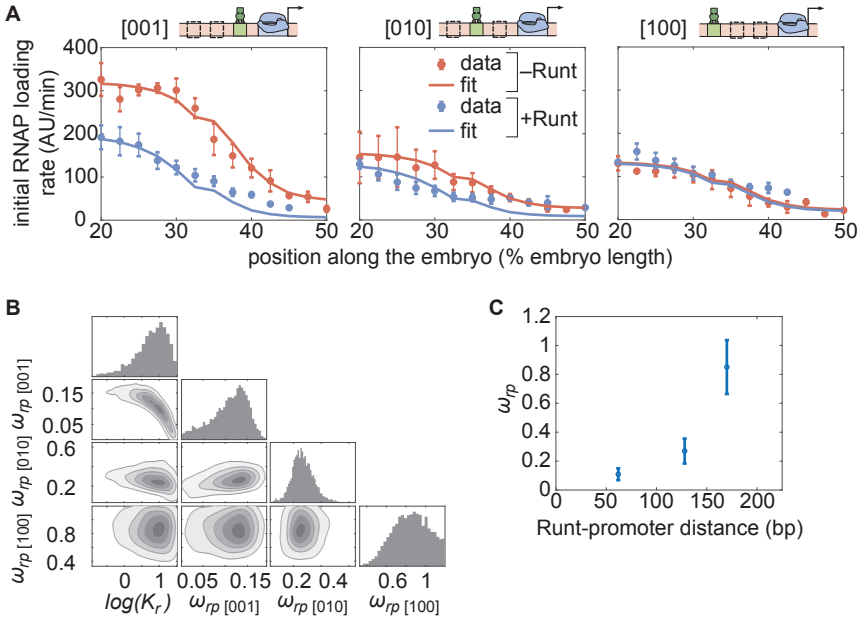

Figure 6: Testing the direct repression model in the presence of one Runt binding site. **(A)** Initial transcription rate as a function of position along the embryo for the three constructs containing one Runt binding site in the presence and absence of Runt repressor, together with their best MCMC fits. **(B)** Corner plots from MCMC inference for all constructs with one Runt binding site. **(C)** Inferred ω_{rp} value as a function of distance between the promoter and the Runt binding site. (B, data points represent mean and standard error of the mean over > 3 embryos; D, data and error bars represent the mean and standard deviation of the posterior chains, respectively.)

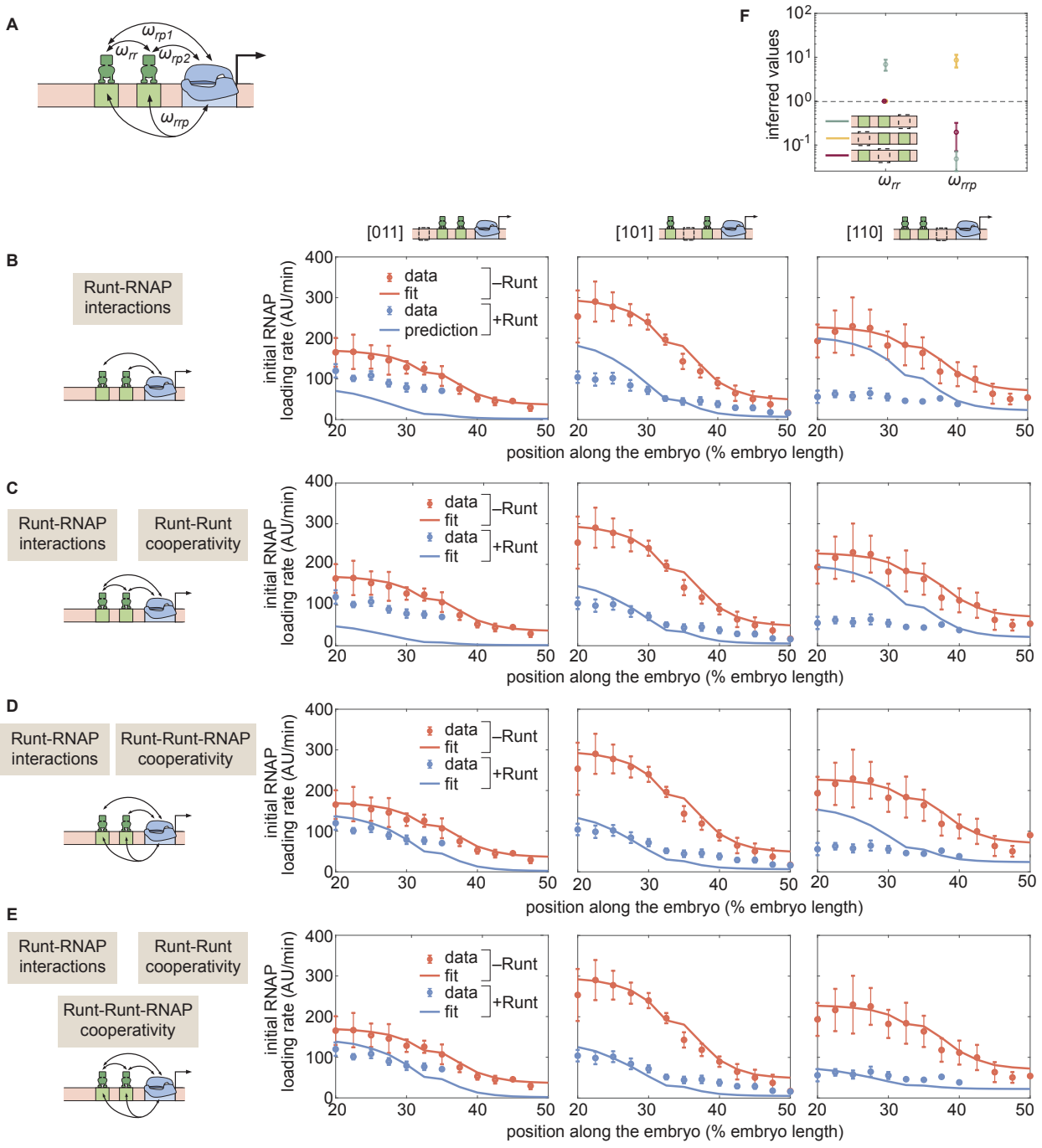

Figure 7: Prediction for the transcription initiation rate of *hunchback* P2 with two-Runt binding sites under different models of cooperativity. See caption in the next page.

Figure 7: Prediction for the transcription initiation rate of *hunchback* P2 with two-Runt binding sites under different models of cooperativity. **(A)** Direct repression model for *hunchback* P2 with two-Runt binding sites featuring Runt-RNAP interaction terms given by ω_{rp1} and ω_{rp2}, Runt-Runt cooperativity captured by ω_{rr}, and Runt-Runt-RNAP higher-order cooperativity accounted for by ω_{rrp}. **(B)** Parameter-free model prediction for two-Runt binding sites when the two Runt molecules bind the DNA and interact with RNAP independently of each other. **(C,D,E)** Best MCMC fits for the data for two-Runt binding site constructs for models with various combinations of cooperativity parameters. **(C)** Model incorporating Runt-Runt cooperativity. **(D)** Model incorporating Runt-Runt-RNAP higher-order cooperativity. **(E)** Model accounting for both Runt-Runt cooperativity and Runt-Runt-RNAP higher-order cooperativity. **(F)** Fixed or inferred parameters ω_{rr} and ω_{rrp} for all two-Runt binding site constructs. Note that ω_{rr} is fixed to 1 for [011] and [101] constructs due to the fact that no Runt-Runt cooperativity is necessary to quantitatively describe the expression driven by these constructs; only the [110] construct is used to infer both $_{rr}$ and ω_{rrp}. The horizontal line of $\omega = 1$ denotes the case of no cooperativity other than Runt-RNAP cooperativity, ω_{rp}. (B-E, data points represent mean and standard error of the mean over > 3 embryos; F, data and error bars represent the mean and standard deviation of the posterior chain, while the standard deviation for the fixed ω_{rr} is set to 0.)

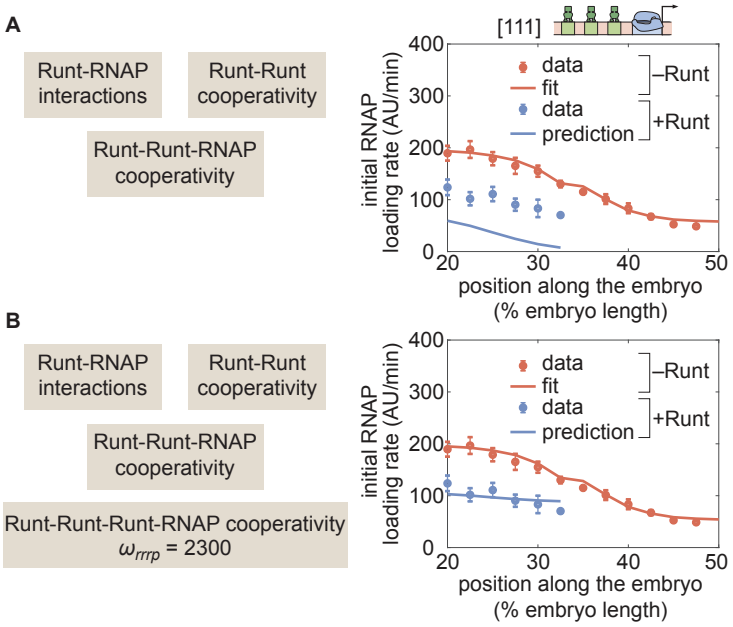

Figure 8: Prediction for *hunchback* P2 with three-Runt binding sites and multiple sources of cooperativity. **(A)** Prediction using previously inferred Runt-RNAP, Runt-Runt, and Runt-Runt-RNAP cooperativity parameters. **(B)** Prediction as in (A), but incorporating an additional Runt-Runt-Runt-RNAP higher-order cooperativity parameter of $\omega_{rrrp} = 2300$, corresponding to roughly 8 k_BT of free energy. (Data points represent mean and standard error of the mean over ¿3 embryos.)

3 Discussion

One of the challenges in generating predictions to probe thermodynamic models is that, often, these models are contrasted against experimental data from endogenous regulatory regions (Park et al. 2019; Sayal et al. 2016; Segal et al. 2008). Here, the presence of multiple binding sites for several transcription factors—known and unknown (Vincent, Estrada, and DePace 2016)—leads to models with a combinatorial explosion of free parameters. Like the proverbial elephant that can be fit with four parameters (Mayer, Khairy, and Howard 2010), experiments with endogenous enhancers typically contain enough parameters to render it possible to explain away apparent disagreement between theory and experiment (Garcia et al. 2020).

To close this gap, synthetic minimal enhancers have emerged as an attractive alternative to endogenous enhancers (Crocker, Ilsley, and Stern 2016; Fakhouri et al. 2010; Park et al. 2019; Sayal et al. 2016). Here, the presence of only a handful of transcription factor binding sites and the ability to systematically control their placement and affinity dramatically reduce the number of free parameters in the model (Garcia et al. 2020). Inferences performed on these synthetic constructs could then inform model parameters that would make it possible to quantitatively predict transcriptional output of *de novo* enhancers (Sayal et al. 2016).

Building on these works, in the present investigation we sought to predict how the Runt repressor, which counteracts activation by Bicoid along the anterior-posterior axis of the early fly embryo (Chen et al. 2012), dictates the output level of transcription. To dissect repression, a strong and detectable level of expression in the absence of the repressor was needed, prompting us to choose a simple system of synthetic enhancers based on the strong *hunchback* P2 minimal enhancer (Chen et al. 2012; Garcia et al. 2013b). This enhancer has been carefully dissected in terms of its activator Bicoid and the pioneer-like transcription factor Zelda in the early embryo (Driever and Nusslein-Volhard 1988; Eck et al. 2020; Garcia et al. 2013b; Park et al. 2019), making it easier to identify neutral sequences within the enhancer for introducing Runt binding sites (Chen et al. 2012). Further, when inserted into *hunchback* P2, Runt binding site number determines the level of transcription incrementally (Chen et al. 2012). Thus, *hunchback* P2 provided an ideal scaffold onto which to quantitatively and systematically dissect repression by Runt.

Previous studies using synthetic enhancers relied on measurements of input transcription factor patterns using fluorescence immunostaining, and of cytoplasmic mRNA patterns using fluorescence in situ hybridization (FISH) or single-molecule FISH. These fixed-tissue techniques have key differences from the live-imaging approach adopted here. First, given the dynamical nature of development, it is necessary to know when data were acquired. Doing so with high temporal resolution using FISH is challenging, although it can be accomplished to some degree by synchronizing embryo deposition before fixation (Park et al. 2019). Second, while most transcription factors directly dictate the rate of RNAP loading, and hence the rate of mRNA production (Eck et al. 2020; Garcia et al. 2013b; Spitz and Furlong 2012), typical FISH measurements report on the accumulated mRNA in the cytoplasm, which is a convolution of all processes of the transcription cycle—initiation, elongation, and termination

(Alberts 2015; Liu et al. 2021)—as well as mRNA nuclear export dynamics, diffusion, and degradation. These processes could be modulated in space and time, potentially confounding measurements. Here, we overcame these challenges by using the MS2 technique to precisely time our embryos and acquire the rate of transcription initiation.

Interestingly, our initial dissection of constructs containing various combinations of Runt binding sites, but in the absence of Runt protein, revealed that unrepressed gene expression levels depend strongly on the number and placement of the binding sites within the enhancer (Fig. 5A). These results challenge previous assumptions that unregulated gene expression levels would stay unchanged as enhancer architecture is modulated (Barr et al. 2017; Fakhouri et al. 2010; Sayal et al. 2016), but they are in accordance with observations in bacterial systems (Garcia et al. 2012). As a result, our measurements call for accounting for unregulated levels in future quantitative dissections of eukaryotic enhancers, or to study relative magnitudes such as the fold-change in gene expression that has driven the dissection of bacterial transcriptional regulation (Phillips et al. 2019).

Once we accounted for this difference in unrepressed gene expression levels, we determined that the repression profiles obtained for constructs bearing one-Runt binding site could be described by a simple thermodynamic model (Fig. 2). Specifically, we showed that the same dissociation constant described Runt binding regardless of the position of its binding site along the enhancer (Fig. 6A). Further, the Runt-RNAP interaction terms describing repressor action decreased as the binding site was placed farther from the promoter (Fig. 6C), qualitatively consistent with a "direct repression" model in which Runt needs to physically contact RNAP in order to realize its function (Gray, Szymanski, and Levine 1994; Hewitt et al. 1999; Jaynes and O'Farrell 1991).

Although our model recapitulated repression by a one-Runt binding site, the inferred parameters were insufficient to quantitatively predict repression by two-Runt binding sites (Fig. S6B). These results suggest that multiple repressors do not act independently of each other. Instead, new parameters describing both Runt-Runt cooperativity and Runt-Runt-RNAP higher-order cooperativity had to be incorporated into our models to quantitatively describe Runt action in these constructs (Fig. S6C-E).

While we have long known about protein-protein cooperative interactions (Ackers, Johnson, and Shea 1982), in the last few years it has become clear that higher-order cooperativity can also be at play in eukaryotic systems (Biddle et al. 2020; Estrada et al. 2016b; Park et al. 2019) as well as in bacteria (Dodd et al. 2004) and archaea (Peeters et al. 2013). The existence of this higher-order cooperativity suggests that, to predict gene expression from DNA sequence, it might be necessary to build an understanding of the many simultaneous interactions that precede transcriptional initiation. Our discovery of higher-order cooperativity in the action of multiple Runt molecules opens up new avenues to uncover the molecular nature of this phenomenon. For example, following an approach developed in (Park et al. 2019), it could be possible to determine whether and how these cooperativity parameters are modulated upon perturbation of molecular players such as the Groucho or CtBP co-repressors, Big-brother, a co-factor facilitating the Runt binding to DNA, and components of the mediator complex (Courey and Jia 2001; Park et al. 2019; Walrad, Hang, and Gergena 2011). Indeed, (Park

et al. 2019) recently showed that co-activators and mediator units are involved in dictating the magnitude of similar higher-order cooperativity terms in activation by Bicoid. Thus, our thermodynamic models provide a lens through which to dissect the molecular underpinnings of Runt interactions with itself and with the transcriptional machinery.

Notably, the need to invoke cooperative interactions as more Runt binding sites are being added opposes our goal of predicting complex regulatory architectures from experiments with simpler architectures without the need to invoke new parameters. However, it will be interesting to determine whether more parameters need to be invoked as the number of Runt binding sites increases beyond three, or whether the parameters already inferred are sufficient to endow our models with parameter-free predictive power.

Importantly, while our model adopted a "direct repression" view of the mechanism of Runt action, other mechanisms of repression such as "quenching" could also describe the data. While all such models call for higher-order cooperativity to describe the data (Supplementary Section S5), our data cannot differentiate among those models. Thus, we did not attempt to distinguish different molecular mechanisms of Runt transcriptional repression.

Finally, even though the work presented here has relied exclusively on thermodynamic models, it is important to note that a much more general approach based on non-equilibrium models could also be appropriate for describing our data. Indeed, an increasing body of work over the last few years has provided evidence for the necessity of invoking these more complex models in the context of transcriptional regulation in eukaryotes (Eck et al. 2020; Estrada et al. 2016b; Li et al. 2018; Park et al. 2019). In future work, it will be interesting to determine whether, when our data is viewed through the lens of these non-equilibrium models, invoking higher-order cooperativity is still necessary or whether, instead, simple pairwise protein-protein interactions suffice to reach an agreement between theory and experiment.

Overall, the work presented here establishes a framework for systematically and quantitatively studying repression in the early fly embryo. As showcased here, synthetic enhancers based on the *hunchback* P2 minimal enhancer constitute an ideal scaffold for the study of other repressors in early fly embryos. For example, we envision that this approach could be used to dissect repression by other transcription factors such as *Capicua* or *Krüppel* (Chen et al. 2012; Löhr et al. 2009; Papagianni et al. 2018; Sauer and Jackle 1991), and to probe observations of multiple repressors working together to oppose activation by Bicoid in establishing gene expression patterns along the anterior-posterior axis (Briscoe and Small 2015; Chen et al. 2012). We anticipate that a similar approach could be used to dissect repression along the dorso-ventral axis of the embryo, by for example, adding repressor binding sites to well-established reporter constructs that are only regulated by the Dorsal activator (Jiang and Levine 1993). Critically, we need to understand not only how one species of repressor works in concert with an activator, but also how multiple species of repressors work together as a system. The approach presented here provides a way forward for predictively understanding the complex gene regulatory network that shapes gene expression patterns in the early fly embryo.

4 Materials and Methods

Generation of synthetic enhancers with MS2 reporters

The synthetic enhancer constructs used in this study are based off of **?**. In summary, the *hunchback* P2 enhancer was used as a scaffold to introduce Runt binding sites at different positions that are thought to be neutral (i.e. these Runt binding sites do not interfere with any other obvious binding sites for other transcription factors in the early *Drosophila* embryos as shown in Fig. S9). For the three positions chosen to introduce Runt binding sites in **?**, the Gene Synthesis service from Genscript was used to generate synthetic enhancers with all possible configurations of zero-, one-, two-, and three-Runt binding sites in *hunchback* P2 as shown in Figure 1A. The enhancer sequences were placed into the original plasmid pIB backbone (Chen et al. 2012) using the Gene Fragment Synthesis service in Genscript, followed by the *even-skipped* promoter, and 24 repeats of MS2v5 loops (Wu et al. 2015), the *lacZ* coding sequence, and the α-Tubulin 3'UTR sequence (Chen et al. 2012). These plasmids were injected into the 38F1 landing site using the RMCE method (Bateman, Lee, and Wu 2006) by BestGene Inc. Flies were screened by selecting for white eye color and made homozygous. The orientation of the insertion was determined by genomic PCR to ensure a consistent orientation across all of our constructs. Specifically, we used two sets of primers that each amplified one of these two possible orientations: "Upward", where the forward primer binds to a genomic location outside of 38F1 (TTCTAGTTCCAGTGAAATCCAAGCA) and the reverse primer binds to a location in our reporter transgene (ACGCCAGGGTTTTCCCAG), and "Downward", where the forward primer remains the same as the "Upward" set and the reverse primer binds to a location in our reporter transgene (CTCTGTTCTCGCTATTATTCCAACC) when the insertion is the opposite orientation to the "Upward" orientation. As a result, only amplicons from either one of the orientations of insertion in the 38F1 landing site can be obtained. We chose the "Downward" orientation for all our constructs.

CRISPR-Cas9 knock-in of the green LlamaTag in the endogenous *runt* locus

We used CRISPR-Cas9 mediated Homology Directed Repair (HDR) to insert the LlamaTag against eGFP into the N-terminal of the *runt* endogenous locus (Bothma et al. 2018; Gratz et al. 2015). The donor plasmid was constructed by stitching individual fragments—PCR amplified left/right homology arms from the endogenous *runt* locus roughly 1 kb in length each, LlamaTag, and pHD-scarless vector—using Gibson assembly (Gratz et al. 2015). The PAM sites in the donor plasmid were mutated such that the Cas9 only cleaved the endogenous loci, not the donor plasmid, without changing the amino acid sequence of the Runt protein. The final donor plasmid contained the 3xP3-dsRed marker such that dsRed is expressed in the fly eye and ocelli for screening. Positive transformant flies were screened using a fluorescence dissection scope and set up for single fly crosses to establish individual lines that were then verified with PCR amplification and Sanger sequencing (UC Berkeley Sequencing Facility).

Importantly, this *llamaTag-runt* allele rescues development to adulthood as a homozygous. Thus we concluded that the LlamaTag-Runt allele can be used to monitor the behavior of endogenous Runt protein.

Fly strains

Transcription from the synthetic enhancer reporter constructs was measured by using embryos from crossing *yw;his2av-mRFP1;MCP-eGFP(2)* females and *yw;synthetic enhancer-MS2v5-lacZ;+* males as described in (Eck et al. 2020; Garcia et al. 2013b; Lammers et al. 2020).

eGFP-Bicoid measurements were performed using the fly line from (Gregor et al. 2007b). The LlamaTag-Runt measurements were done using the fly line *LlamaTag-Runt; +; vasa-eGFP, His2Av-iRFP* illustrated in Table 2. Briefly, eGFP was supplied by a *vasa* maternal driver. Females carrying both the LlamaTag-Runt and the *vasa*-driven eGFP were crossed with males carrying the LlamaTag-Runt, the progeny from this cross were imaged and then recovered to determine the embryo's sex using PCR. PCR was run with three sets of primers: Y chr1 (Forward: CGATCCAGCCCAATCTCTCATATCACTA, Reverse: ATCGTCGGTAATGTGTCCTCCGTAATTT), Y chr2 (Forward: AACGTAACCTAGTCGGATTGCAAATGGT, Reverse: GAGGCGTACAATTTCCTTTCTCATGTCA), and Auto1 (Forward: GATTCGATGCACACTCACATTCTTCTCC , Reverse: GCTCAGCGCGAAACTAACATGAAAAACT). Two of primer sets (Y chr1 and Y chr2) bind to the Y chromosome while the other one (Auto1) binds to the autosome and constitutes a positive control (Lott et al. 2011).

To generate the embryos that are zygotic null for the runt allele, we used a fly cross scheme consisting of two crosses. In the first generation, we crossed *LlamaTag-Runt;+;+* males with *run3/FM6;+;MCP-eGFP(4F),his2av-mRFP1* females. *run3* is the null allele for *runt*, missing around 5 kb including the coding sequence of the *runt* locus (Chen et al. 2012; Gergen and Butler 1988). The *MCP-eGFP(4F)* transgene expresses approximately twice the amount of MCP protein than the *MCP-eGFP(2)* (Eck et al. 2020; Garcia et al. 2013b) and thus results in similar levels of MCP to those of *MCP-eGFP(2)* in the trans-heterozygotes. The female progeny from this cross, *LlamaTag-Runt/run3;+;MCP-eGFP(4F),his2av-mRFP1/+* was then crossed with males whose genotype was *LlamaTag-Runt/Y;synthetic enhancer-MS2v5-lacZ;+* to produce the embryos that we used for live imaging. The resulting embryos carried maternally supplied MCP-eGFP and His-RFP for visualization of nascent transcripts and nuclei. The X chromosome contained LlamaTag-Runt allele or *run3* null allele. We could differentiate between these two genotypes because, when the embryo had the Runt allele, a stripe pattern would appear in late nc14. We imaged all embryos until late nc14 to make sure that we were capturing the nulls.

Sample preparation and data collection

Sample preparation was done following the protocols described in **?**. Briefly, embryos were collected, dechorionated with bleach for 1-2 minutes, and then mounted between a

semipermeable membrane (Lumox film, Starstedt, Germany) and a coverslip while embedded in Halocarbon 27 oil (Sigma-Aldrich). Live imaging was performed using a Leica SP8 scanning confocal microscope, a White Light Laser and HyD dectectors (Leica Microsystems, Biberach, Germany). Imaging settings for the MS2 experiments with the presence of MCP-eGFP and Histone-RFP were the same as in **?** except that we used 1024x245 (pixels) format to image a wider field of view along the anterior-posterior axis. The settings for the eGFP-Bicoid measurements were the same as described in **?**.

The settings for the eGFP:LlamaTag-Runt measurements were similar to that of eGFP-Bicoid except for the following. To increase our imaging throughput, we utilized the "Mark and Position" functionality in the LASX software (Leica SP8) to image 5-6 embryos simultaneously. To account for the decreased time resolution, we lowered the z-stack size from 10 μm to 2.5 μm, keeping the 0.5 μm z-step. By doing this, we could maintain 1 minute frame rate for each imaged embryo. Additionally, these flies expressed Histone-iRFP, instead of Histone-RFP as in **?**, so that we used a 670 nm laser at 40 μW (measured at a 10x objective) for excitation of the histone channel, and the HyD detector was set to a 680 nm-800 nm spectral window.

Image Analysis

Images were analyzed using custom-written software (MATLAB, mRNA Dynamics Github repository) following the protocol in **?** and **?**. Briefly, this procedure involved segmentation and tracking of nuclei and transcription spots. First, segmentation and tracking of individual nuclei were done using the histone channel as a nuclear mask. Second, segmentation of each transcription spot was done based on its fluorescence intensity and existence over multiple z-stacks. The intensity of each MCP-GFP transcriptional spot was calculated by integrating pixel intensity values in a small window around the spot and subtracting the background fluorescence measured outside of the active transcriptional locus. When there was no detectable transcriptional activity, we assigned NaN values for the intensity. The tracking of transcriptional spots was done by using the nuclear tracking and proximity of transcriptional spots between consecutive time points. The nuclear protein fluorescence intensities from the eGFP-Bicoid and LlamaTag-Runt fly lines, which we use as a proxy for the protein nuclear concentration, were calculated as follows. Using the nuclear mask generated from the histone channel, we performed the same nuclear segmentation and tracking as described above for the MS2 spots. Then,for every z-section, we extracted the integrated fluorescence over a $2\mu m$ diameter circle on the xy-plane centered on each nucleus. For each nucleus, the recorded fluorescence corresponded to the z-position where the fluorescence was maximal. This resulted in an average nuclear concentration as a function of time for each single nucleus. These concentrations from individual nuclei were then averaged over a narrow spatial window (2.5% of the embryo length) to generate the spatially averaged protein concentration reported in the main text. For the eGFP:LlamaTag-Runt datasets, we had to subtract the background eGFP fluorescence due to the presence of an unbound

eGFP population (Bothma et al. 2018). We used the same protocol described in **?** and in the Supplementary Section S7 to extract this background.

Bayesian inference procedure: Markov Chain Monte Carlo sampling

Parameter inference was done using the Markov Chain Monte Carlo (MCMC) method. We used a well-established package *MCMCstat* that uses an adaptive MCMC algorithm (Haario, Saksman, and Tamminen 2001; Haario et al. 2006). A detailed description on how we performed the MCMC parameter inference, for example setting the priors and bounds for parameters, is illustrated in Supplementary Section S4 .

Biological Materials

Plasmids	
Name (hyperlinked to Benchling)	**Function**
pIB-hbP2-evePr-MS2v5-LacZ-Tub3UTR	[000]-MS2v5 reporter construct
pIB-hbP2+r1-far-evePr-MS2v5-LacZ-Tub3UTR	[100]-MS2v5 reporter construct
pIB-hbP2+r1-mid-evePr-MS2v5-LacZ-Tub3UTR	[010]-MS2v5 reporter construct
pIB-hbP2+r1-close-evePr-MS2v5-LacZ-Tub3UTR	[001]-MS2v5 reporter construct
pIB-hbP2+r2-2+3-evePr-MS2v5-LacZ-Tub3UTR	[011]-MS2v5 reporter construct
pIB-hbP2+r2-1+3-evePr-MS2v5-LacZ-Tub3UTR	[101]-MS2v5 reporter construct
pIB-hbP2+r2-1+2-evePr-MS2v5-LacZ-Tub3UTR	[110]-MS2v5 reporter construct
pIB-hbP2+r3-evePr-MS2v5-LacZ-Tub3UTR	[111]-MS2v5 reporter construct
pHD-scarless-LlamaTag-Runt	Donor plasmid for LlamaTag-Runt CRISPR knock-in fusion for the N-terminal
pU6:3-gRNA(Runt-N-2)	gRNA plasmid for LlamaTag-Runt CRISPR knock-in fusion for the N-terminal
pCasper-vasa-eGFP	*vasa* maternal driver for ubiquitous eGFP expression in the early embryo

Table 1: List of plasmids used to create the transgenic fly lines used in this study.

Fly lines	
Genotype	**Use**
LlamaTag-Runt; +; vasa-eGFP, His2Av-iRFP	Visualize LlamaTagged Runt protein and label nuclei
LlamaTag-Runt; +; MCP-eGFP(4F), His2Av-iRFP	Visualize LlamaTagged Runt protein, nascent transcripts and label nuclei
run3/FM6; +; +	Visualize LlamaTagged Runt protein, nascent transcripts and label nuclei
yw; His2Av-mRFP; MCP-eGFP	Females to label nascent RNA and nuclei
yw; [000]-MS2v5 ; +	Males carrying the MS2 reporter transgene
yw; [100]-MS2v5 ; +	Males carrying the MS2 reporter transgene
yw; [010]-MS2v5 ; +	Males carrying the MS2 reporter transgene
yw; [001]-MS2v5 ; +	Males carrying the MS2 reporter transgene
yw; [011]-MS2v5 ; +	Males carrying the MS2 reporter transgene
yw; [101]-MS2v5 ; +	Males carrying the MS2 reporter transgene
yw; [110]-MS2v5 ; +	Males carrying the MS2 reporter transgene
yw; [111]-MS2v5 ; +	Males carrying the MS2 reporter transgene

Table 2: List of fly lines used in this study and their experimental usage

5 Acknowledgements

We are grateful to Armando Reimer, Brandon Schlomann, Elizabeth Eck, Gabriella Martini, Jacques Bothma, Jeehae Park, Jia Ling, Matthew Norstad, Michael Eisen, Nicholas Lammers, Nipam Patel, Rob Phillips, Simon Alamos, Xavier Darzacq,and Yasemin Kirişçioğlu for their guidance and comments on our manuscript. This work was supported by the Burroughs Wellcome Fund Career Award at the Scientific Interface, the Sloan Research Foundation, the Human Frontiers Science Program, the Searle Scholars Program, the Shurl and Kay Curci Foundation, the Hellman Foundation, the NIH Director's New Innovator Award (DP2 OD024541-01), and NSF CAREER Award (1652236) to HGG, and a KFAS scholarship to YJK.

S1 Derivation of the general thermodynamic model for the *hunchback* P2 enhancer

In this section, we rederive the thermodynamic model presented in the main text, now without the assumption of strong Bicoid-Bicoid cooperativity. The equilibrium thermodynamic modeling framework that we used in this paper is described in more detail in **??**.

We start by modeling the case of *hunchback* P2 without any Runt binding sites, which is believed to have at least six Bicoid binding sites (Driever, Thoma, and Nusslein-Volhard 1989; Park et al. 2019). As shown by the states and weights presented in Figure S1A, in our thermodynamic model, we assume that the six Bicoid binding sites have the same dissociation constant given by K_b, and we posit that RNAP-promoter binding is governed by a dissociation constant given by K_p. We also assume pairwise cooperativity between Bicoid molecules given by ω_b, and cooperativity between each Bicoid molecule and RNAP given by ω_{bp}. For simplicity, we will use the dimensionless parameters $b = [Bicoid]/K_b$ and $p = [RNAP]/K_p$, where $[Bicoid]$, and $[RNAP]$ are the concentrations of Bicoid and RNAP, respectively, and K_b and K_p are their corresponding dissociation constants.

We factor the total partition function into two categories: Z_b corresponding to states that only have Bicoid bound, and Z_{bp} describing states with both Bicoid and RNAP bound. Then then calculate each component separately. The sum of microstates for Z_b is

$$Z_b = 1 + 6b + 15b^2\omega_b + \cdots + b^6\omega_b^5 = 1 + \sum_{i=1}^{6} \binom{6}{i} b^i \omega_b^{i-1}. \tag{S1}$$

Using the binomial theorem, we can simplify Equation S1 leading to

$$Z_b = 1 + \sum_{i=1}^{6} \binom{6}{i} b^i \omega_b^{i-1} = 1 + \frac{1}{\omega_b}\left[(1 + b\ \omega_b)^6 - 1\right]. \tag{S2}$$

Using the same logic, we obtain Z_{bp} such that

$$Z_{bp} = \left(p + p \sum_{i=1}^{6} \binom{6}{i} b^i \omega_b^{i-1} \ \omega_{bp}^i \right) = p + \frac{p}{\omega_b} \left[(1 + b \ \omega_b \ \omega_{bp})^6 - 1 \right]. \tag{S3}$$

Using these two partition functions, we then calculate the probability of the promoter being bound by RNAP, p_{bound} as

$$P_{bound} = \frac{Z_{bp}}{Z_b + Z_{bp}} = \frac{p + \frac{p}{\omega_b} \left[(1 + b \ \omega_b \ \omega_{bp})^6 - 1 \right]}{1 + \frac{1}{\omega_b} \left[(1 + b \ \omega_b)^6 - 1 \right] + p + \frac{p}{\omega_b} \left[(1 + b \ \omega_b \ \omega_{bp})^6 - 1 \right]}. \tag{S4}$$

Following recent work (Gregor et al. 2007b; Park et al. 2019), we now assume that the Bicoid-Bicoid pairwise cooperativity is very strong ($\omega_b \gg 1$). We can then simplify Equation S4 to obtain

$$P_{bound} = \frac{p + p \ b^6 \ \omega_b^5 \ \omega_{bp}^6}{1 + p + b^6 \ \omega_b^5 + p \ b^6 \ \omega_b^5 \ \omega_{bp}^6}. \tag{S5}$$

If we now define a new binding constant for Bicoid, $K_b' = K_b * (\frac{1}{\omega_b})^{\frac{5}{6}}$, such that $b' = b \ \omega_b^{\frac{5}{6}}$, and a new cooperativity term between Bicoid and RNAP given by $\omega_{bp}' = \omega_{bp}^6$, we can then rewrite Equation S5 as

$$P_{bound} = \frac{p + b'^6 \ p \ \omega_{bp}'}{1 + p + b'^6 + b'^6 \ p \ \omega_{bp}'}, \tag{S6}$$

which is the expression we use throughout the main text. Thus, strong pairwise cooperativity between Bicoid molecules leads to a functional form where only the state with all Bicoid molecules bound remain (six in this case). This strong cooperativity can explain the sharp step-like expression pattern along the embryo's anterior-posterior axis of the *hunchback* gene (Fig. 3J; **????**).

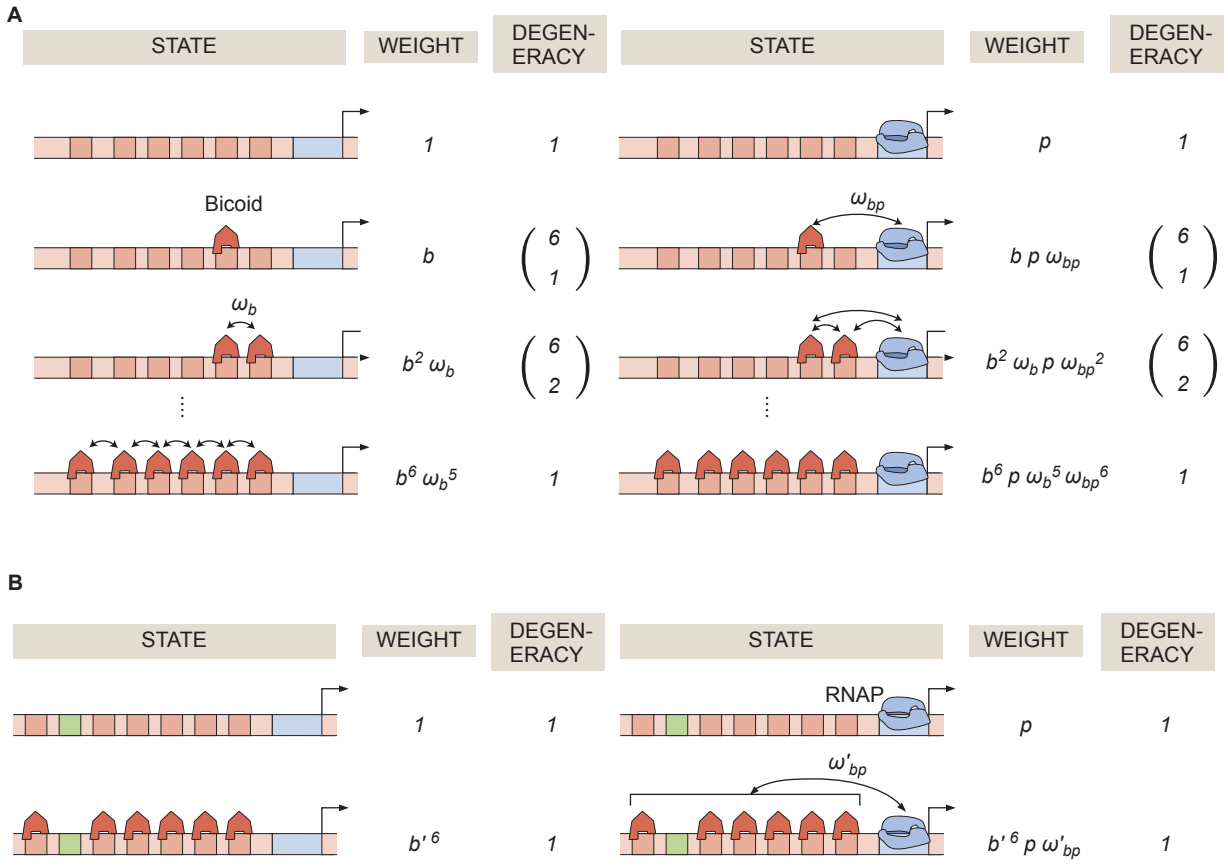

Figure S1: General thermodynamic model for a *hunchback* P2 enhancer with six Bicoid binding sites. **(A)** States, weights, and degeneracy considered for our thermodynamic model. **(B)** Simpler form of the thermodynamic model in the limit of $\omega_b \gg 1$.

S2 Derivation of the general and simpler thermodynamic model for the *hunchback* P2 enhancer with one Runt binding site

Having derived the equation for the strong cooperative binding of Bicoid to the wild-type *hunchback* P2 enhancer, we will now extend that model to the case of *hunchback* P2 with one Runt binding site. The corresponding states and weights of our full model are shown in Figure S2A.

Using a similar logic for calculating the partition functions as described in the previous

section, we can compute the probability of the promoter being bound by RNAP as

$$\mathrm{p}_{bound} = \frac{\overbrace{\left(p + p\sum_{i=1}^{6}\binom{6}{i} b^i \omega_b^{i-1} \omega_{bp}^i\right)}^{\text{Bicoid and RNAP}} + \overbrace{\left(r\ p\ \omega_{rp} + r\ p\ \omega_{rp}\sum_{i=1}^{6}\binom{6}{i} b^i \omega_b^{i-1} \omega_{bp}^i\right)}^{\text{Bicoid, Runt, and RNAP}}}{\underbrace{\left(1 + \sum_{i=1}^{6}\binom{6}{i} b^i \omega_b^{i-1}\right)}_{\text{Bicoid only}} + \underbrace{\left(p + p\sum_{i=1}^{6}\binom{6}{i} b^i \omega_b^{i-1} \omega_{bp}^i\right)}_{\text{Bicoid and RNAP}} + \underbrace{\left(r + r\sum_{i=1}^{6}\binom{6}{i} b^i \omega_b^{i-1}\right)}_{\text{Bicoid and Runt}} + \underbrace{\left(rp\omega_{rp} + rp\omega_{rp}\sum_{i=1}^{6}\binom{6}{i} b^i \omega_b^{i-1} \omega_{bp}^i\right)}_{\text{Bicoid, Runt, and RNAP}}}, \tag{S7}$$

where, in addition to the parameters defined in the above section for the wild-type *hunchback* P2 case in the absence of Runt, we have added two parameters: the dissociation constant for Runt given by K_r, and a Runt-RNAP interaction term (an anti-cooperativity), ω_{rp}. Using the binomial theorem as in Equation S2, we can simplify Equation S7 to obtain

$$\mathrm{p}_{bound} = \frac{p + \frac{p}{\omega_b}[(1+b\omega_b\omega bp)^6 - 1] + rp\omega_{rp} + \frac{rp\omega_{rp}}{\omega_b}[\left(1+b\omega_b\omega_{bp}\right)^6) - 1]}{1 + \frac{1}{\omega_b}[(1+b\omega_b)^6 - 1] + p + \frac{p}{\omega_b}[(1+b\omega_b\omega bp)^6 - 1] + r + \frac{r}{\omega_b}[(1+b\omega_b)^6 - 1] + rp\omega_{rp} + \frac{rp\omega_{rp}}{\omega_b}[\left(1+b\omega_b\omega_{bp}\right)^6 - 1]}. \tag{S8}$$

We now again assume that Bicoid-Bicoid cooperativity is very strong such that $\omega_b \gg 1$. Then, we can combine Equation S8 with Equation 1 to obtain

$$Rate = R\ p_{bound} = R\ \frac{p + b'^6\ p\ \omega_{bp} + r\ p\ \omega_{rp} + b'^6\ r\ p\ \omega'_{bp}\ \omega_{rp}}{1 + b'^6 + r + b'^6\ r + p + b'^6\ p\ \omega'_{bp} + r\ p\ \omega_{rp} + b'^6\ r\ p\ \omega'_{bp}\ \omega_{rp}}, \tag{S9}$$

where the new parameters, b' and ω'_{bp} are defined in the same way as in Equation S6. The effective states and weights remaining after taking this limit are shown in Figure S2B. Similarly, we can derive expressions for p_{bound} in the presence of two and three Runt binding sites, and in the strong Bicoid-Bicoid cooperativity limit in order to obtain the predictions used throughout this text. We show this expression for two Runt binding sites in Equation 5.

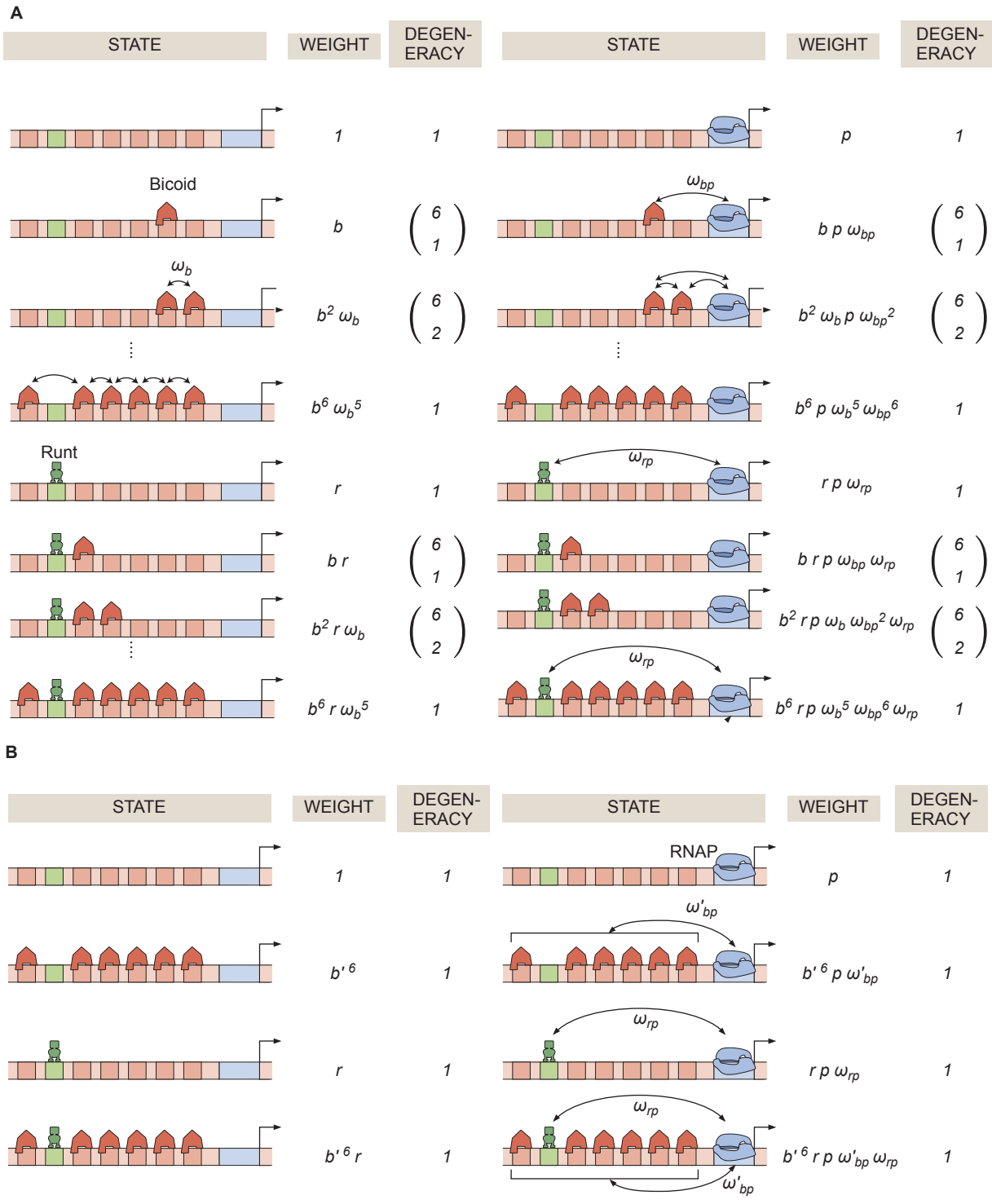

Figure S2: General thermodynamic model for an enhancer with six-Bicoid binding sites and one Runt binding site. **(A)** Statistical weights and degeneracy of each state the system can be found in. **(B)** Simpler form of the model from (A) in the limit of strong Bicoid-Bicoid cooperativity.

S3 Comparing using static versus dynamic transcription factor concentrations as model inputs

In this section, we tested whether using static, time-averaged transcription factor concentration profiles yielded comparable theoretical predictions than when instead acknowledging the fact that input transcription factor concentration changes over time. Briefly, we compared the predicted rate of transcription calculated in two ways: (1) time-averaging the instantaneous rate from the dynamic transcription factor concentration profiles over a specified time window (from 5 to 10 minutes from the 13th anaphase) and (2) using static input transcription factors already time-averaged over the same time window.

As a concrete example, we focused on the *hunchback* P2 enhancer with one Runt binding site. We calculated the predicted rate of transcription using the thermodynamic model given by Equation 2. First, we performed this calculation using the dynamic concentration profiles of Bicoid and Runt shown in Figure 3B and D, respectively. Briefly, the terns b and r in Equation 2 now become functions of time such that

$$Rate(t) = R\,\frac{p + b^6(t)\ p\ \omega_{bp} + r(t)\ p\ \omega_{rp} + b^6(t)\ r(t)\ p\ \omega_{bp}\ \omega_{rp}}{1 + b^6(t) + r(t) + b^6(t)\ r(t) + p + b^6(t)\ p\ \omega_{bp} + r(t)\ p\ \omega_{rp} + b^6(t)\ r(t)\ p\ \omega_{bp}\ \omega_{rp}}, \tag{S10}$$

where $b(t) = [Bicoid](t)/K_b$ and $r(t) = [Runt](t)/K_r$. We choose a set of reasonable values for the model parameters to illustrate the calculation of $Rate(t)$ at 30% of the embryo length. The resulting dynamic rate of transcription profile is shown in Figure S3A (blue curve). We then use this profile to calculate the time-averaged rate of transcription over the time window of 5 to 10 minutes from the 13th anaphase, resulting in the green area shown in Figure S3A.

The predicted average rate of RNAP loading given dynamic input transcription factors can be compared to the predicted rate of RNAP loading given the average input concentrations that we used throughout the main text (Fig. 3E). Specifically, we plug the static concentration profiles of Bicoid and Runt shown in Figure 3E into Equation 2 to obtain the red area shown in Figure S3A. As shown in the figure, the predicted rate of transcription obtained by these two analysis methodologies are equivalent within error.

Finally, we performed this comparison between different approaches to calcualte the rate of transcription as a function of position along the embryo (from 20% to 70% of the embryo length). As shown in Figure S3B, the resulting spatial profiles are comparable within error. Thus, we have shown that our approach of using time-averaged, static transcription factor concentrations as inputs to our model yield quantitatively equivalent result as accounting for the dynamic concentration profiles of these transcription factors.

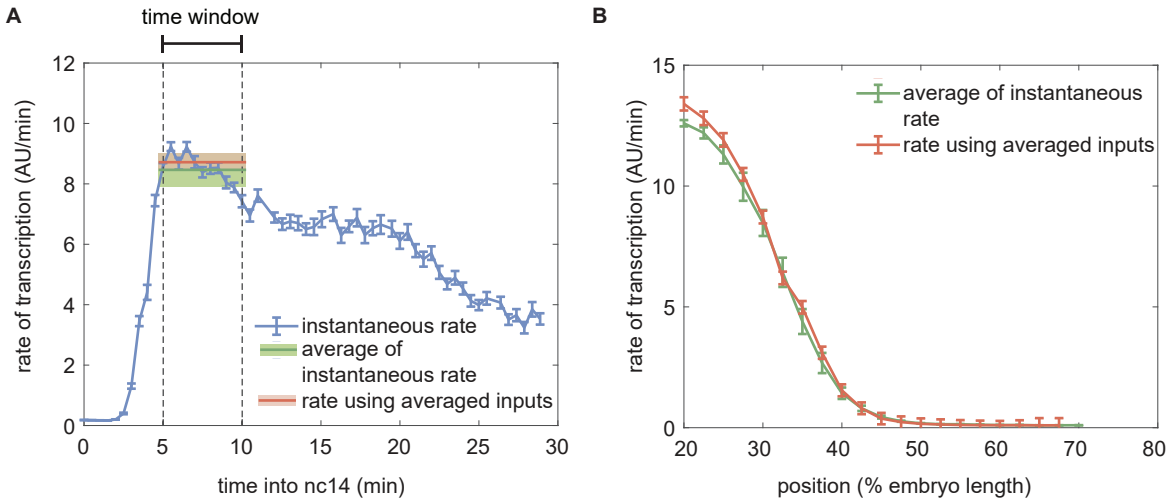

Figure S3: Comparison of the predicted rate of transcription using dynamic and time-averaged transcription factor concentration profiles as inputs. **(A)** Instantaneous predicted rate of transcription calculated using dynamic transcription factor concentration profiles at each time point (blue) and resulting averaged rate of transcription averaged over the time window of 5-10 minutes from the 13th anaphase (green) compared to the predicted rate of transcription obtained using the static transcription factor concentrations of Bicoid and Runt shown in Figure 3E (red). (Illustrative predictions calculated at 30% of the embryo length using $K_b = 30(AU)$, $K_r = 100(AU)$, $\omega_{bp} = 100$, $\omega_{rp} = 0.1$, $p = 0.001$, $R = 300(AU/min)$.) **(B)** Spatial profile of the predicted rate of transcription calculated by averaging the instantaneous transcription rate (green) or by using the averaged input transcription factor concentrations as inputs (red). (A, B, error bars and shaded areas represent the standard error of mean over embryos 42 embryos generated from making pairs of independently measured six eGFP-Bicoid embryo and seven GreenLlamaTag-Runt embryo.)

S4 Markov Chain Monte Carlo inference protocol

Markov Chain Monte Carlo (MCMC) sampling is a widely used technique for robust parameter estimation using Bayesian statistics (Geyer and Thompson 1992; Sivia and Skilling 2006). We used the MATLAB package *MCMCstat*, an adaptive MCMC technique, which we could directly implement downstream of our data analysis pipeline (Haario, Saksman, and Tamminen 2001; Haario et al. 2006). Detailed instructions on how to implement the *MCMCstat* package can be found in `https://mjlaine.github.io/mcmcstat/`.

MCMC allows for an estimation of the set of parameter values of a model that best explain the experimental data along with their associated errors. In this work, we used MCMC to infer the set of best fit values of the parameters in our thermodynamic models given the observed profile of the rate of transcription initiation along the anterior-posterior axis of the embryo.

MCMC calculates a Bayesian posterior probability distribution of each free parameter given the data by stochastically sampling different parameter values. For a given set of observations D and a model with parameters θ, the posterior probability distribution of a particular set of values is given by Bayes' theorem

$$\underbrace{p(\theta|D)}_{\text{posterior}} \propto \underbrace{p(D|\theta)}_{\text{likelihood}} \underbrace{p(\theta)}_{\text{prior}}. \tag{S11}$$

The prior function represents the *a priori* assumption about the probability distribution of parameter values θ. Here, we assumed a uniform prior distribution for all parameters to reflect our ignorance about the model parameters within the following intervals:

- K_b: $[0, 100]$ AU
- ω_{bp}: $[0, 200]$
- p: $[0, 1]$
- R: $[0, 400]$ AU/min
- K_r: $[0, 100]$ AU
- ω_{rp}: $[0, 1.2]$
- ω_{rr}: $[0, 100]$
- ω_{rrp}: $[0, 100]$

These intervals were justified using the following arguments.

First, because we observed a gradual modulation of the rate of transcription by both Bicoid and Runt in the middle region of the embryo we reasoned that the binding sites for these transcription factors were not saturated. As a result, we posited that the real dissociation

constant should be between the minimum and maximum measured values of Bicoid and Runt (Fig. S10). Our measurements of Bicoid and Runt concentration yield fluorescence values over the 0-100 AU range for the embryo region that we used for contrasting our model and experimental data (20-50% of the embryo length), such that the dissociation constants (K_b and K_r) should not exceed the maximum value of the Bicoid or Runt concentration.

Second, ω_{bp} represents the cooperativity between Bicoid complex and RNAP. In the statistical mechanics framework, this cooperativity can be expressed using the interaction energy between Bicoid and RNAP, $\Delta\epsilon_{bp}$, such that $\omega_{bp} = exp(-\beta\Delta\epsilon_{bp})$, where $\beta = \frac{1}{k_B\ T}$, k_B is the Boltzmann constant and T is the temperature. There is not much known about *in vivo* interaction energies between Bicoid and RNAP complex, thus we tried several different bounds until we found a narrow enough parameter bound with unimodal distribution of the posterior chain. As we could see from the corner plots in Figure 5C, there is a positive correlation between K_b and ω_{bp}. Thus, we constrained the ω_{bp} intervals by finding an interval that gives both well-constrained K_b and ω_{bp} (Fig. 5C).

Third, R represents the rate of RNAP loading when the promoter is occupied, thus it is constrained by the maximum observed rate of RNAP loading (Fig. S10).

Fourth, $p = [RNAP]/K_p)$ represents the concentration of RNAP divided by its dissociation constant. Recall that the predicted rate of transcription from *hunchback* P2 in the limit where the Bicoid concentration reaches zero is given by

$$Rate([Bicoid] \to 0) = R\ \frac{p}{1+p}. \tag{S12}$$

This rate of transcription at the posterior region, where Bicoid reaches zero, is much lower than that at the anterior region where Bicoid saturates given by R (Fig. S10). As a result, we can write the inequality

$$R\ \frac{p}{1+p} \ll R. \tag{S13}$$

such that

$$\frac{p}{1+p} \ll 1, \tag{S14}$$

which holds if $p \ll 1$.

Finally, we did not have good estimates for the intervals of either Runt-Runt cooperativity, ω_{rr}, or higher-order cooperativity, ω_{rrp}. Thus, we initially started with an interval of $[0, 100]$, of the same order as the interval we used ω_{bp}. We then explored whether this parameter bound was sufficient to give us constrained values of ω_{rr} and ω_{rrp}. As we showed in Figure S16D, this interval gives reasonably constrained values of ω_{rr} and ω_{rrp}. As shown in Figure 7 and Figure S16, we posit that the ω_{rr} parameter is not well-constrained not because of its width of the interval, but because it is not as essential for the model fit to the data as it is to include ω_{rrp} into the model. Overall, our MCMC inference results as well as the corner plots shown demonstrate that our parameter intervals chosen were reasonable.

S5 Comparison of different modes of repression

Transcriptional repressors have been classified into two broad categories: short-range and long-range, depending on the genomic length scale that they act on (Courey and Jia 2001; Li and Gilmour 2011). Long-range repression is realized by the recruitment of chromatin modifiers. In contrast, short-range repressors act within 100-150 bp by interacting with nearby transcription factors or with the promoter (Li and Gilmour 2011). Traditionally, the molecular mechanism of short-range repressors, such as Runt, have been further classified into three categories: "direct repression", "competition", and "quenching" (Arnosti et al. 1996; Gray, Szymanski, and Levine 1994; Jaynes and O'Farrell 1991; Kulkarni and Arnosti 2005). In "direct repression", the repressor inhibits the binding of RNAP to the promoter (Fig. S4A). "Competition" denotes a repressor that competes with an activator for the same DNA binding location (Fig. S4B). This molecular mechanisms has been proposed for the action of Giant and Krüppel repressors on the *even-skipped* stripe 2 enhancer, where some activator and repressor binding sites partially overlap (Small, Blair, and Levine 1992). Lastly, "quenching" corresponds to the case where the repressor and activator do not interact with each other directly. Instead, the repressor inhibits the activators' action of recruiting the RNAP (Fig. S4C).

Despite several classic studies of the molecular mechanism of repressors in the early fly embryo (Bothma, Magliocco, and Levine 2011; Gray, Szymanski, and Levine 1994; Ip et al. 1992; Jaynes and O'Farrell 1991), the mechanisms of many repressors remain unknown. Note that, even for the same repressor, the mode of repression might not be the same depending on, for example, its sequence context (Hang and Gergen 2017; Koromila and Stathopoulos 2019). For example, it has been proposed that Runt repressor acts with different mechanisms in different regulatory elements of the *sloppy-paired* gene (Hang and Gergen 2017). In this section, we derive a thermodynamic model from each mode of repression and compare their explanatory power in the context of our data stemming from the *hunchback* P2 enhancer containing one Runt binding site. Note that, in the main text, we already developed a thermodynamic model for the "direct repression" scenario (Section S2). As a result, in this section, we focus on deriving the thermodynamic models for the "competition" and "quenching" scenarios, but repeat the result of the derivation for the "direct repression" here for ease comparison between different models.

Derivation of models for each scenario of repression for *hunchback* P2 with one Runt binding site

Modeling repression for *hunchback* P2 with one Runt binding site: direct repression

For completeness, we repeat the expression for the direct repression scenario as shown in Section S2 and Figure S4A. The probability of finding RNAP bound to the promoter, p_{bound}, is calculated by dividing the sum of all statistical weights featuring RNAP by the sum of

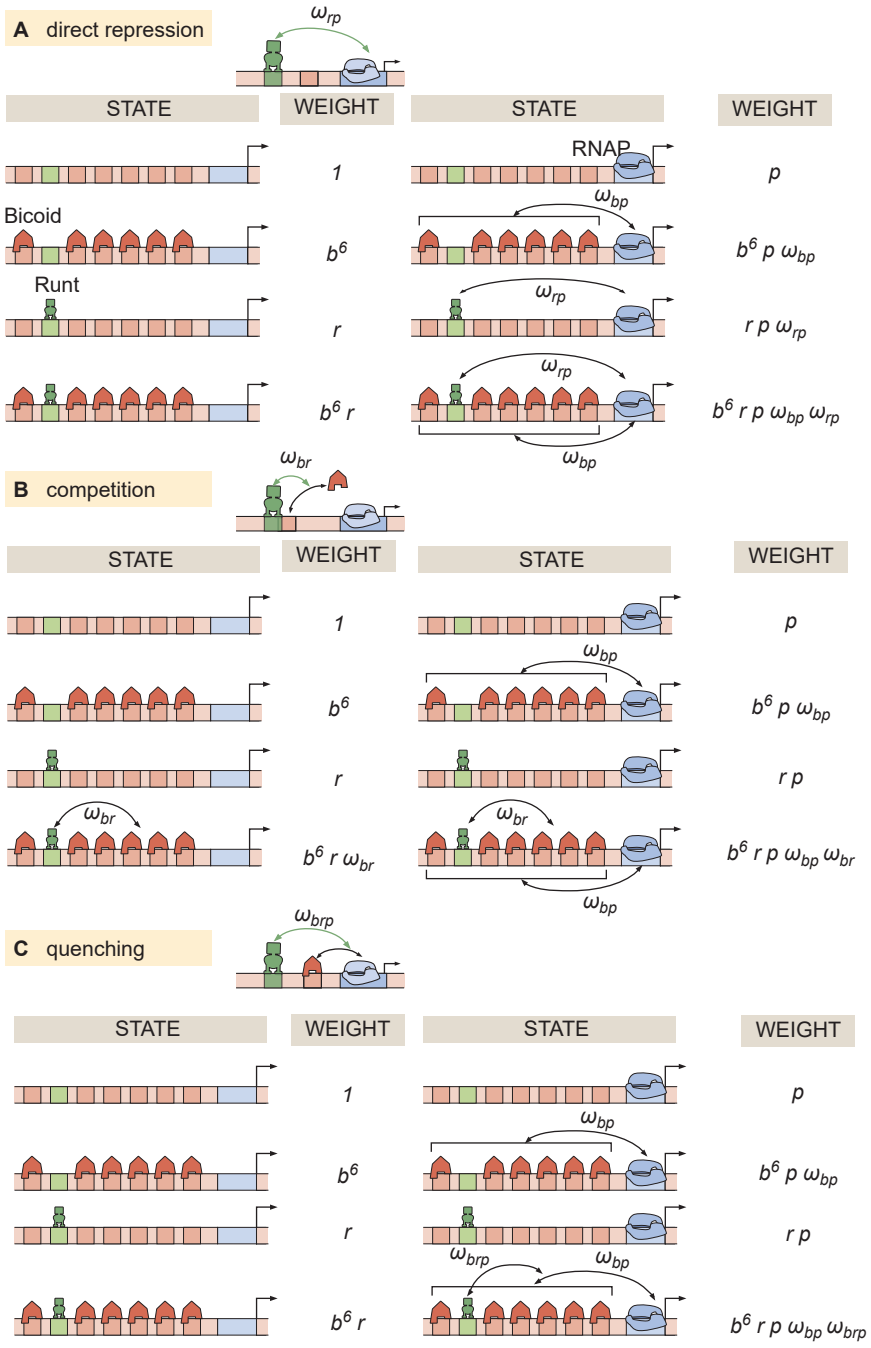

Figure S4: Thermodynamic models for different modes of repression. States and statistical weights corresponding to the *hunchback* P2 enhancer with one Runt binding site for the **(A)** direct repression, **(B)** competition, and **(C)** quenching mechanisms.

the weights of all possible microstates. The calculation of p_{bound}, combined with Equation 1, leads to the expression

$$Rate = R\ p_{bound} = R\ \frac{p + b^6\ p\ \omega_{bp} + r\ p\ \omega_{rp} + b^6\ r\ p\ \omega_{bp}\ \omega_{rp}}{1 + b^6 + r + b^6\ r + p + b^6\ p\ \omega_{bp} + r\ p\ \omega_{rp} + b^6\ r\ p\ \omega_{bp}\ \omega_{rp}}, \quad \text{(S15)}$$

where the parameters are as defined in Figure 2.

Modeling repression for *hunchback* P2 with one Runt binding site: competition

In the competition scenario, Runt binding makes Bicoid binding less likely. This mechanism can be captured by an interaction term between Bicoid and Runt given by ω_{br}. Building on our assumption of strong Bicoid-Bicoid cooperativity, we posit that Runt disfavors the state with six bound Bicoid molecules. We can enumerate the states and weights from Fig. S4B to calculate the $Rate$ ($\propto p_{bound}$) , which leads to

$$Rate = R\ \frac{p + b^6\ p\ \omega_{bp} + r\ p + b^6\ r\ p\ \omega_{bp}\ \omega_{br}}{1 + p + b^6 + r + b^6\ r\ \omega_{br} + b^6\ p\ \omega_{bp} + r\ p + b^6\ r\ p\ \omega_{bp}\ \omega_{br}}. \quad \text{(S16)}$$

Modeling repression for *hunchback* P2 with one Runt binding site: quenching

In the quenching scenario, Runt reduces the magnitude of the cooperativity between the Bicoid complex and RNAP by a factor ω_{brp}. We can enumerate the states and weights from Fig. S4C, leading to a rate of transcription given by

$$Rate = R\ \frac{p + b^6\ p\ \omega_{bp} + r\ p + b^6\ r\ p\ \omega_{bp}\ \omega_{brp}}{1 + p + b^6 + r + b^6\ r + b^6\ p\ \omega_{bp} + r\ p + b^6\ r\ p\ \omega_{bp}\ \omega_{brp}}. \quad \text{(S17)}$$

With these expressions for each repression mechanism in hand, we can now compare how each model fares against our experimental data.

Comparing the three models of repression with the one-Runt binding site data

We used the MCMC sampling to fit each model to our experimentally measured initial rate of transcription over the anterior-posterior axis of the embryo. As shown in Figure S5A, B, and C, we see that all three models can explain the [100] and [010] construct data relatively well. However, the competition model resulted in a qualitatively poor fit to the [001] construct as shown by the lack of saturation in the most anterior region of the embryo (Fig. S5C, ii). The direct repression and quenching models showed equally good fits to the data stemming from this construct.

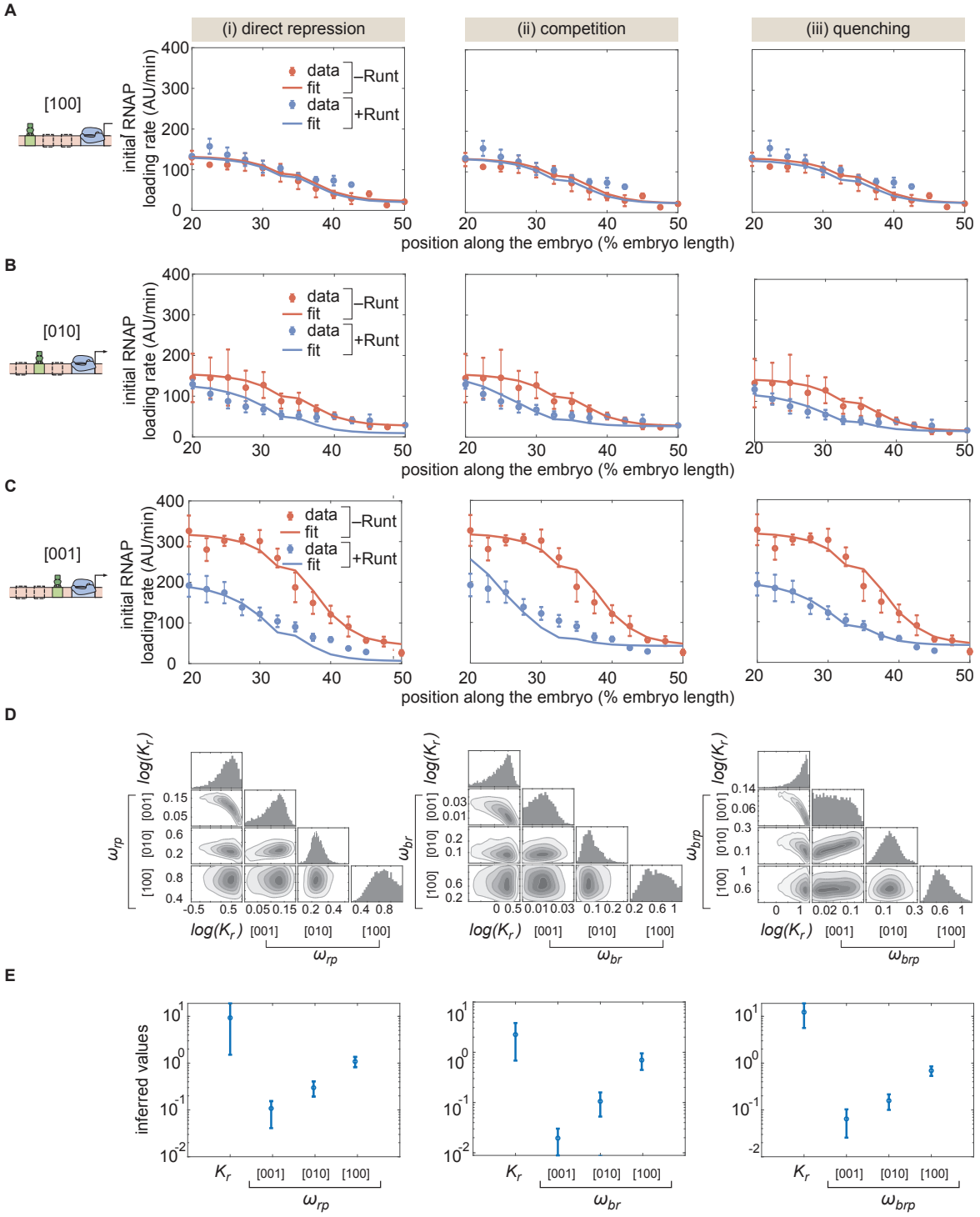

Figure S5: MCMC fitting to the *hunchback* P2 with one Runt binding site constructs using different models of repression. **(A,B,C)** MCMC fits for three modes of repression, (i) direct repression, (ii) competition, and (iii) quenching, for our three one-Runt site constructs, **(A)** [100], **(B)** [101], and **(C)** [001]. **(D)** Corner plots resulteing from MCMC inference on the three one-Runt site constructs for each model. **(E)** Inferred parameters from MCMC fitting. (A,B, and C, error bars represent standard error of the mean over ≥ 3 embryos; E, error

Predicting two-Runt binding sites data for each mode of repression

We further tested these different models of repression by using the parameters inferred from the one-Runt binding site constructs to predict the rate of initiation for the two-Runt binding sites constructs. As reasoned in the main text, we began by assuming that the two Runt molecules act independently of each other such that there are no interactions between Runt molecules. Figure S6 shows this parameter-free prediction for our two-Runt binding sites constructs for all three modes of repression. As shown in the figure, none of the models can explain the data, suggesting the need to invoke additional interactions between the molecular players of our model.

Next, we considered whether Runt-Runt pairwise or higher-order cooperativities had to be invoked in order to explain the two-Runt binding sites data for both the competition and quenching mechanisms. For the competition model, we considered Runt-Runt cooperativity, ω_{rr}, and Runt-Runt-Bicoid higher-order cooperativity, ω_{brr} in addition to the Runt-Bicoid interaction term ω_{br}. In the quenching scenario, we accounted for Runt-Runt cooperativity, ω_{rr}, and Runt-Runt-Bicoid-RNAP higher-order cooperativity, ω_{brrp}. For both the competition (Fig. S7) and quenching (Fig. S8) mechanisms, we observed a qualitatively similar trend to that observed for direct repression (Fig. 7). Specifically, as shown in Figures S7C and S8C, considering pairwise cooperativity did not significantly improve the MCMC fits to the data for either model considered. Further, considering only the higher-order cooperativity also did not improve the fits for both competition and quenching mechanisms as shown in Figure S7D and Figure S8D. Invoking both Runt-Runt cooperativity and higher-order cooperativity improved the fits qualitatively for both competition and quenching mechanisms as shown in Figure S7E and Figure S8E.

While the quenching model showed almost equally good MCMC fits to the data as the direct repression model, the competition model showed qualitatively poor fits in any combination of cooperativities. In particular, there was a significant mismatch in the most anterior region of the embryo, where Bicoid is thought to saturate *hunchback* expression. While we do not view these fits as conclusive evidence to support one mechanism over the other, an exercise that would require a new round of experimentation, we conclude that higher-order cooperativity is required to explain the data from the two-Runt binding sites constructs regardless of the choice of mechanism of Runt.

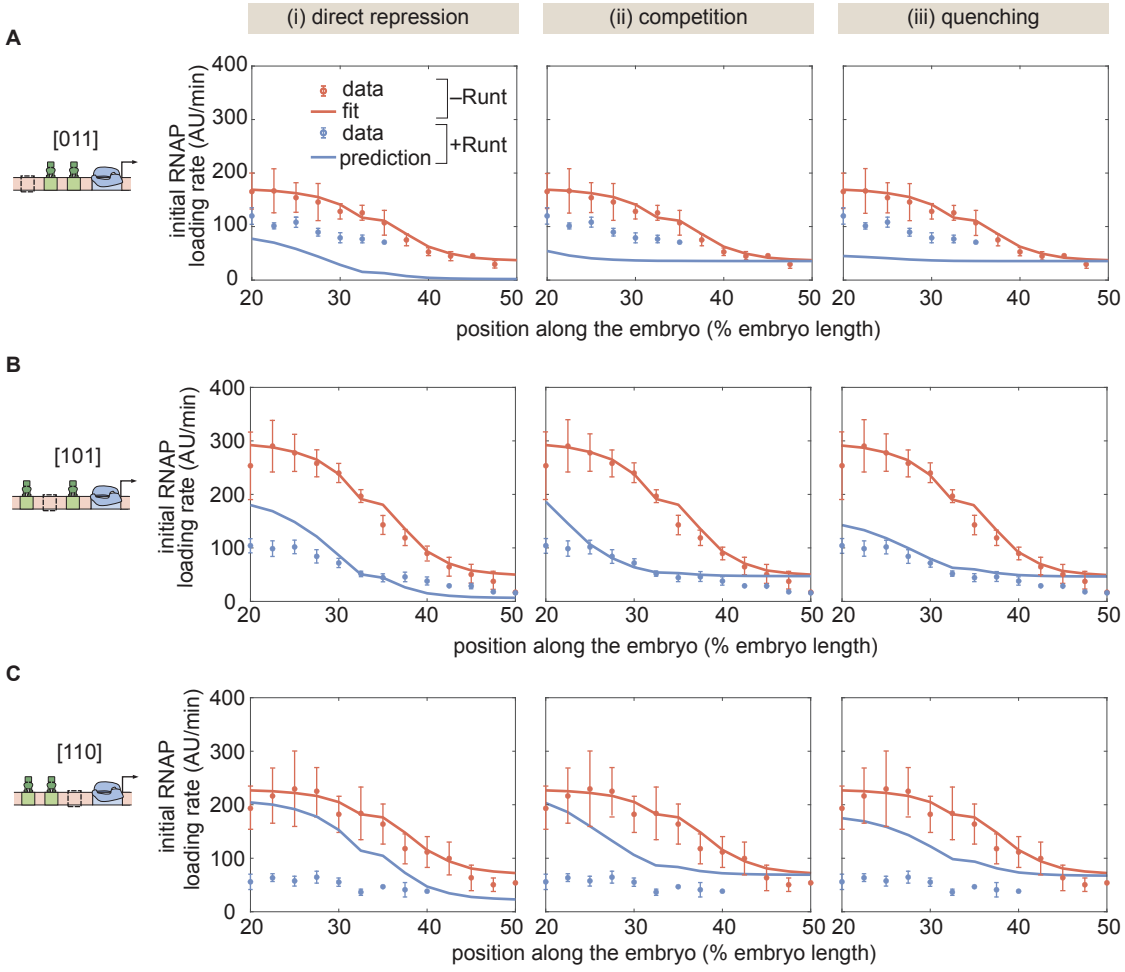

Figure S6: Prediction for two-Runt binding sites constructs based on the inferred parameters from the one-Runt binding site cases for different modes of repression for the **(A)** [011], **(B)** [101], and **(C)** [110] constructs. The model assumes no interactions between Runt molecules. (A,B, and C, error bars represent standard error of the mean over ≥ 3 embryos.)

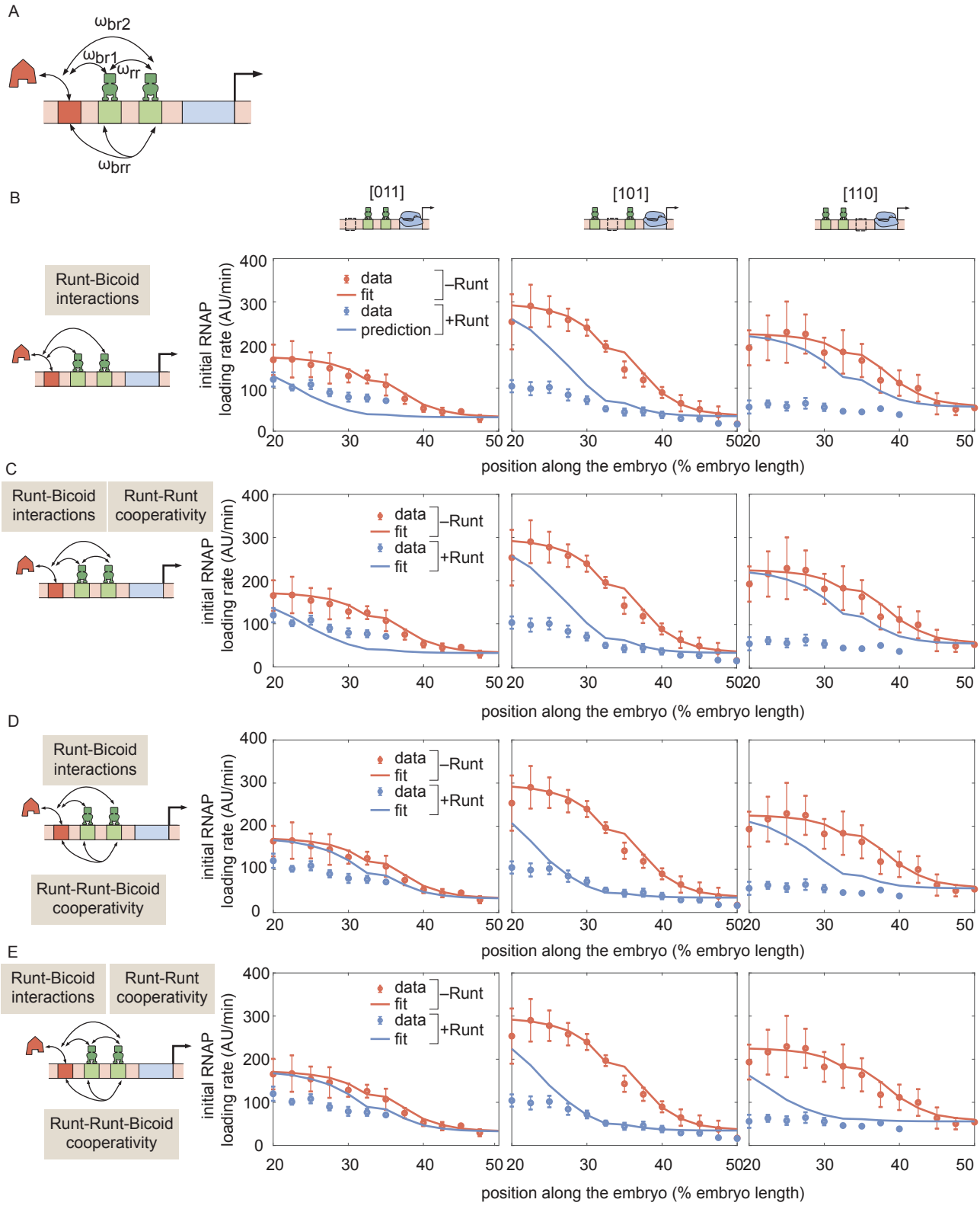

Figure S7: Prediction for *hunchback* P2 transcription initiation rate with two-Runt binding sites under the competition scenario for different combinations of cooperativities. See caption in the next page.

Figure S7: Prediction for *hunchback* P2 transcription initiation rate with two-Runt binding sites under the competition scenario for different combinations of cooperativities. **(A)** Schematic of cooperativity terms considered: Runt-Runt cooperativity given by ω_{rr} and Runt-Runt-Bicoid complex higher-order cooperativity captured by ω_{brr}, in addition to the competition terms ω_{br1} and ω_{br2}. **(B)** Zero-parameter prediction using the inferred parameters from zero- and one-Runt binding site constructs. **(C,D,E)** Best MCMC fits for our three two-Runt binding sites constructs considering **(C)** Runt-Runt cooperativity, **(D)** Runt-Runt-Bicoid complex higher-order cooperativity, and **(E)** both Runt-Runt cooperativity and Runt-Runt-Bicoid complex higher-order cooperativity. (B,C,D, and E, error bars represent standard error of the mean over ≥ 3 embryos.)

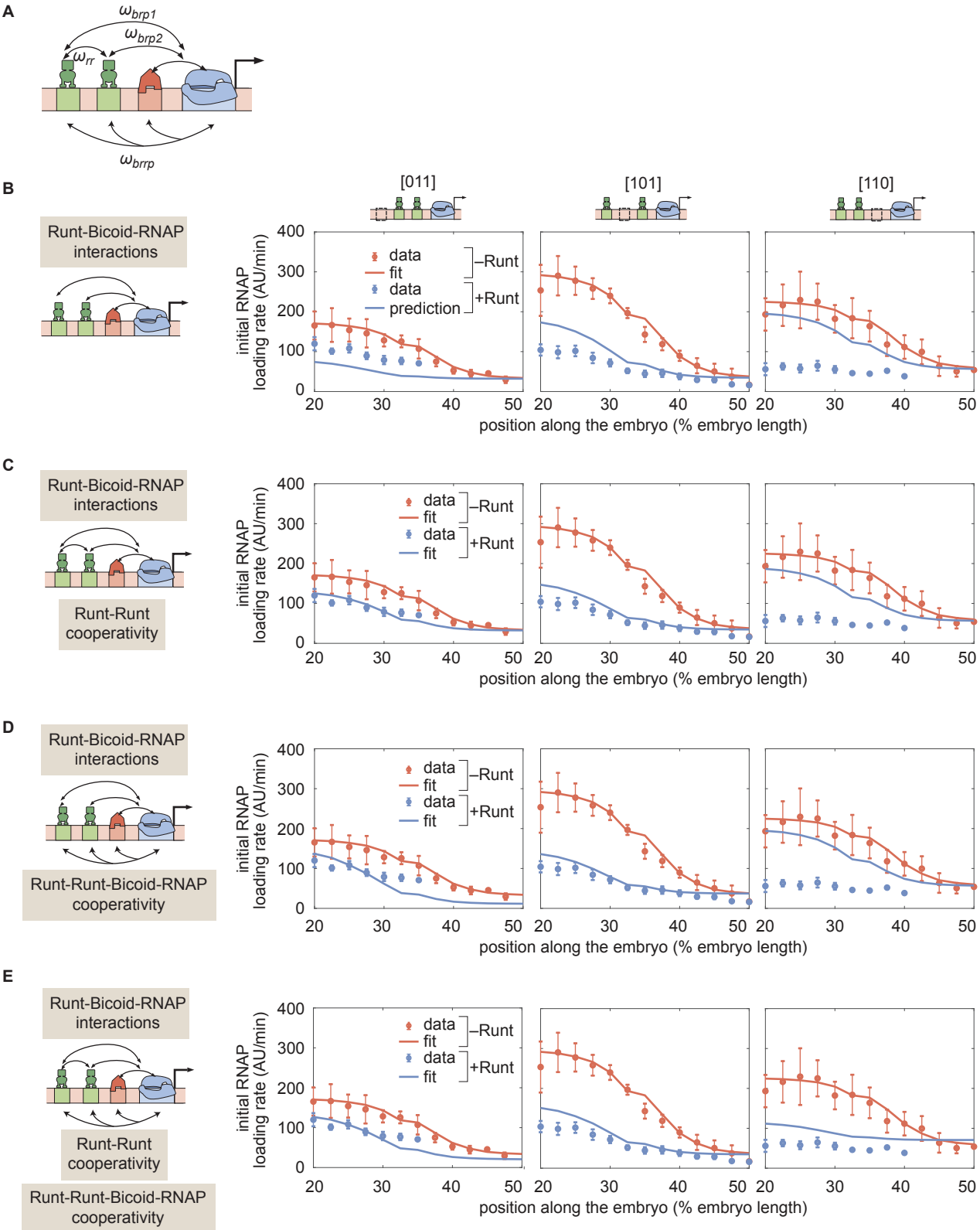

Figure S8: Prediction for *hunchback* P2 transcription initiation rate with two-Runt binding sites under the quenching mechanism for different combinations of cooperativities. See caption in the next page.

Figure S8: Prediction for *hunchback* P2 transcription initiation rate with two-Runt binding sites under the quenching mechanism for different combinations of cooperativities. **(A)** Schematics of additional cooperativities considered: Runt-Runt cooperativity ω_{rr} and Runt-Runt-Bicoid-RNAP complex higher-order cooperativity ω_{brrp}. **(B)** Zero-parameter prediction using the inferred parameters from one-Runt binding site constructs. **(C,D,E)** Best MCMC fits for our three two-Runt binding sites constructs considering **(C)** Runt-Runt cooperativity, **(D)** Runt-Runt-Bicoid-RNAP higher-order cooperativity, and **(E)** both Runt-Runt cooperativity and Runt-Runt-Bicoid-RNAP higher-order cooperativity. (B,C,D, and E, error bars represent standard error of the mean over ≥ 3 embryos.)

S6 Design of synthetic enhancer constructs based on the *hunchback* P2 enhancer

The Runt binding sites were introduced into the hunchback P2 minimal enhancers at the positions determined by **?**. To make this possible, the authors chose positions containing presumed neutral DNA sequences, meaning that these DNA locations did not contain obvious motifs for Bicoid or Zelda, the major input transcription factors that regulate this enhancer. Then, these DNA sequences were mutated to turn them into Runt binding sites.

To ensure that this process did not perturb the binding sites for Bicoid and Zelda we resorted to the Advanced PATSER entry form (Hertz, Hartzell, and Stormo 1990; Hertz and Stormo 1999) which identifies the location of transcription factor binding sites from a sequence of DNA based on position weight matrices. We used position weight matrices for Bicoid and Zelda from **?**. PATSER was run with the settings described in **?** for both the *hunchback* P2 enhancer and the *hunchback* P2 enchancer with three Runt binding sites (from **?**) for Bicoid and Zelda, respectively. The result of this analysis for these two constructs is shown for each transcription factor in Figure S9A. Here, we took a the PATSER score cutoff—for considering a given sequence to be a binding site—of 3 as in **?**. We observed that the recognized binding motifs for both Bicoid and Zelda were identical between the two constructs, meaning that we did not add additional Bicoid or Zelda binding sites by introducing the Runt motifs. The resulting synthetic enhancer with three Runt binding sites with mapped binding sites for Bicoid, Zelda (Fig. S9A), and Runt (Chen et al. 2012) is shown in Figure S9B as a reference. The position of the Runt binding sites are noted from their distance from the promoter (which is marked as 0).

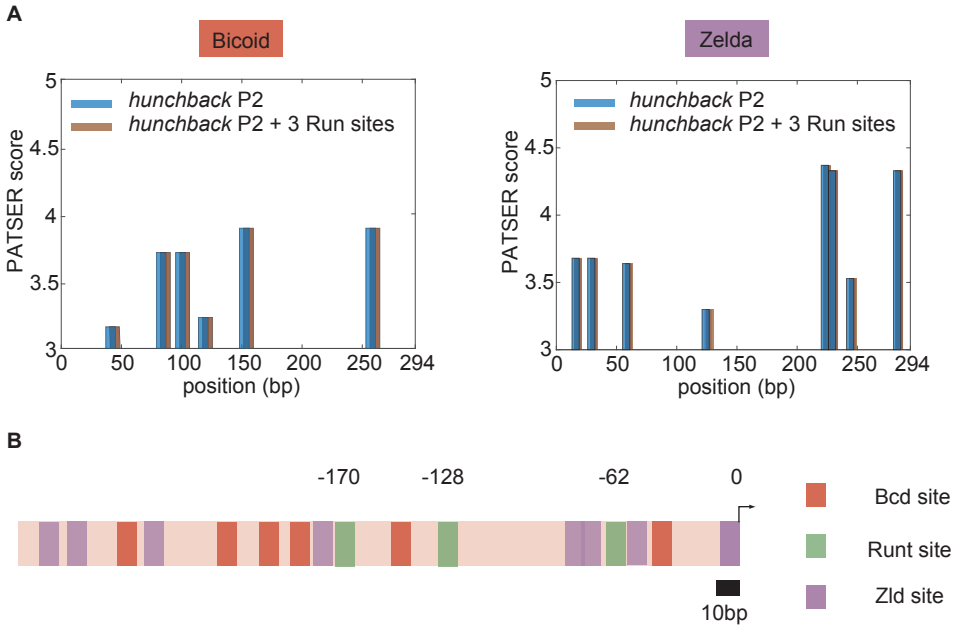

Figure S9: Bioinformatically predicted architecture of major transcription factor binding sites in the *hunchback* P2 minimal enhancer with three Runt binding sites. **(A)** PATSER scores for Bicoid and Zelda for *hunchback* P2 (blue) and *hunchback* P2 with three Runt sites (brown). The binding motifs with PATSER scores higher than three are shown. We concluded that neither Bicoid nor Zelda binding sites were created or removed by the introduction of these three Runt binding motifs. **(B)** A schematic diagram of *hunchback* P2 minimal enhancer with three Runt binding sites with mapped binding sites for Bicoid and Zelda from (A) and Runt binding sites from **?**. The position of Runt binding sites are noted with their distance from the promoter (marked as 0).

S7 Quantifying the nuclear concentration of LlamaTag-Runt

The major caveat in the eGFP:LlamaTag-Runt fluorescence measurements is that the raw nuclear fluorescence that we measured consists of two populations: eGFP *bound* to the LlamaTag-Runt, and *free*, *unbound* eGFP. Thus, in order to measure nuclear Runt concentration, we need to factor out the contribution from free eGFP to the overall fluorescence.

We followed the procedure described in **?** which consists of using cytoplasmic fluorescence to calculate the free nuclear eGFP under two assumptions. First, we posit that most of the transcription factors reside in the nucleus such that the cytoplasmic fluorescence mostly reports on free cytoplasmic eGFP. Second, we assume that the nucleus-to-cytoplasm ratio of free eGFP is kept constant at a measured chemical equilibrium of $K_G = GFP_C/GFP_N = 0.8$, where GFP_C and GFP_N are the eGFP fluorescence in nuclei and cytoplasm in the absence of LlamaTag (Bothma et al. 2018).

As shown in **?**, the nuclear concentration of the GFP-tagged transcription factor, $GFP - TF_N$, is given by

$$GFP - TF_N = Fluo_N - \frac{Fluo_C}{K_G}, \tag{S18}$$

where $Fluo_N$ and $Fluo_C$ are the eGFP fluorescence in nuclei and cytoplasm, respectively, that we measured in the embryos with both eGFP and LlamaTagged Runt. The resulting nuclear concentration of LlamaTag-Runt is shown in Figure 3B.

S8 Quantitative interpretation of MS2 signals

The MS2 signal reports on three features of transcriptional dynamics: 1) the initial RNAP loading rate, 2) the duration of transcription, and 3) the fraction of loci that engage in transcription at any time point in the nuclear cycle. In this section, we will explain in further detail how we extract these features from the MS2 signal over nuclear cycle 14.

Extracting the initial RNAP loading rate

The initial rate of RNAP loading corresponds the average transcription rate observed after transcriptional onset and until the MS2 signal reaches its peak value during nuclear cycle 14. In order to measure this rate, we followed the protocol described in **?**. Briefly, as shown in Figure S10A, we fitted a line to the MS2 time trace (averaged over nuclei within a spatial window of 2.5% of the embryo length) within the time window of 5 to 10 minutes after the 13th anaphase. The slope of this line reported on the initial rate of RNAP loading (Fig. 3G). The spatial profiles of this initial rate of RNAP loading across all our synthetic enhancer constructs and genotypes are shown in Figure S10B.

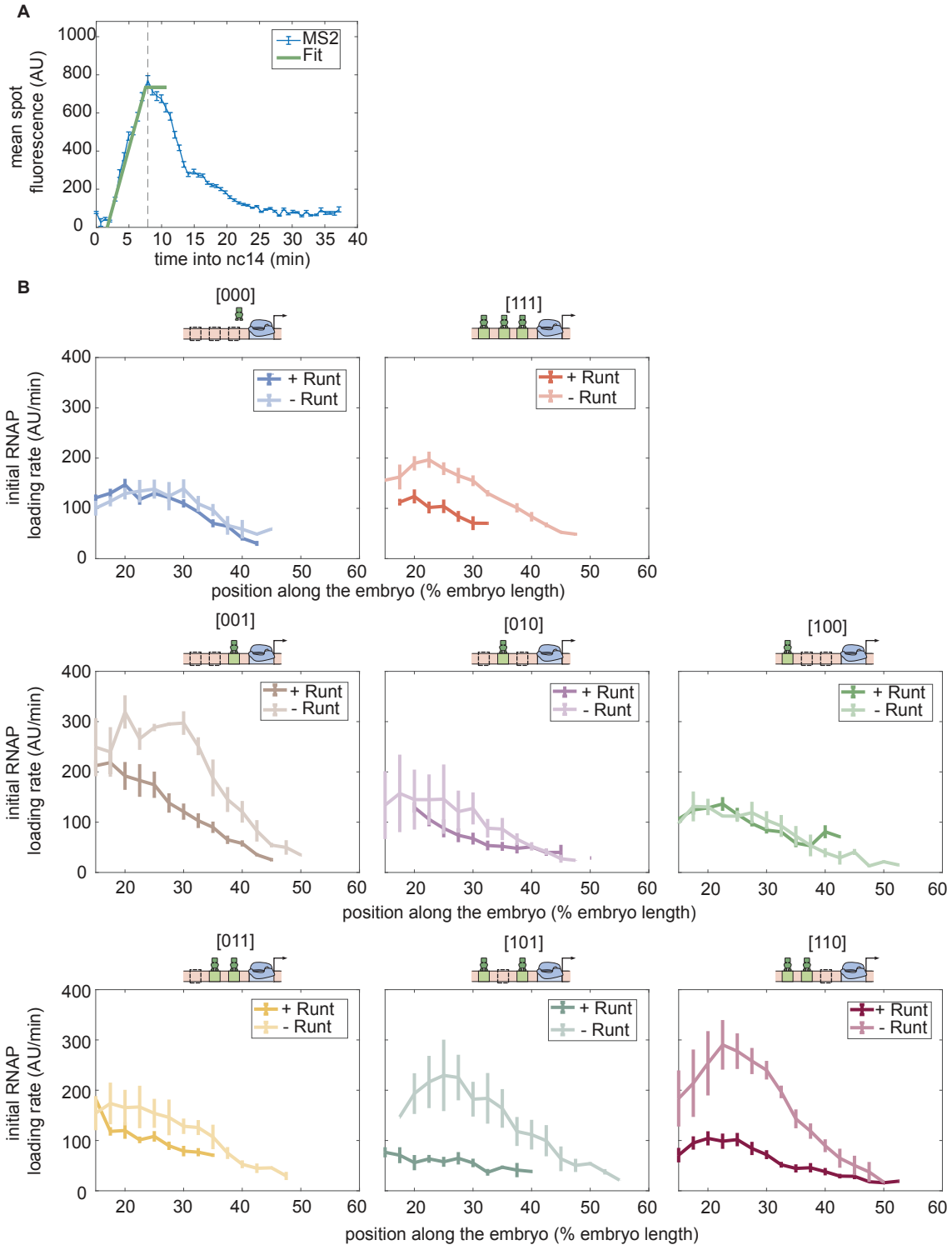

Figure S10: Initial rate of RNAP loading in nuclear cycle 14 across the anterior-posterior axis for different constructs, with or without Runt protein. **(A)** Schematic showing how the initial rate of RNAP loading is measured by extracting the slope resulting from a linear fit to the MS2 time traces at the beginning of nuclear cycle 14. **(B)** Initial rate of RNAP loading along the embryo length for each construct

Extracting the duration of transcription

In the main text, we focused on the theoretical prediction of the initial rate of transcription. However, the length of the time window over which transcription occurs (Lammers et al. 2020) is another regulatory knob that, in principle, Runt could modulate to dictate gene expression patterns. We sought to determine the duration of time over which transcription occurs to assess whether Runt affects not only the initial rate of transcription, but also the time window over which transcription could initiate. To quantify the effective duration of transcription initiation, we resorted to the analysis methodology developed in **?**. Briefly, we parametrized the MS2 signal decay regime—after transcription reaches its peak and becomes slower than the unloading rate (Garcia et al. 2013b)—as an exponential decay (Fig. S11A). Thus, we can describe the MS2 spot fluorescence trace in the decay regime as

$$Fluo(t) = Fluo_{max} e^{-(t-T_{peak})/\tau}, \tag{S19}$$

where T_{peak} represents the time point where the MS2 spot fluorescence reaches its peaks, and τ is the decay time.

Given the sometimes noisy MS2 traces (data not shown), we fitted an exponential curve to the more robust integral of the MS2 spot fluorescence over time from T_{peak} to the end of nuclear cycle 14 as shown in Figure S11B. This quantity is proportional to the amount of mRNA produced between the integration bounds (Garcia et al. 2013b). The resulting accumulated mRNA time trace is then fitted to the integrated form of Equation S19, which is given by

$$mRNA\ (t) = mRNA_{max}(1 - e^{(t-T_{peak})/\tau}), \tag{S20}$$

where $mRNA_{max}$ is the accumulated mRNA at the end of nuclear cycle 14.

The resulting profiles of the duration of transcription along the embryo for our all synthetic enhancer constructs are illustrated in Figure S11C in the presence and absence of Runt protein. As shown in the figure, this duration time is not significantly modulated by Runt repressor.

Calculation of the fraction of competent nuclei

Another quantity that could be modulated by Runt repressor is the fraction of loci that ever engage in transcription during a given nuclear cycle, which we termed as the "fraction of competent loci". As demonstrated by **???** and **?**, this fraction of transcriptionally competent loci is modulated along the anterior-posterior axis, presumably due to the action of transcription factor gradients.

To show a concrete example of how this quantity is calculated, we take data from one construct ([000]) showing the MS2 spot fluorescence time traces from individual loci of transcription as shown in Figure S12A. Here, columns represent time points during nuclear cycle 14, and rows represent individual transcriptional loci. As shown in the figure, roughly 80% of the loci, labeled as "competent loci", show active transcription during nuclear cycle

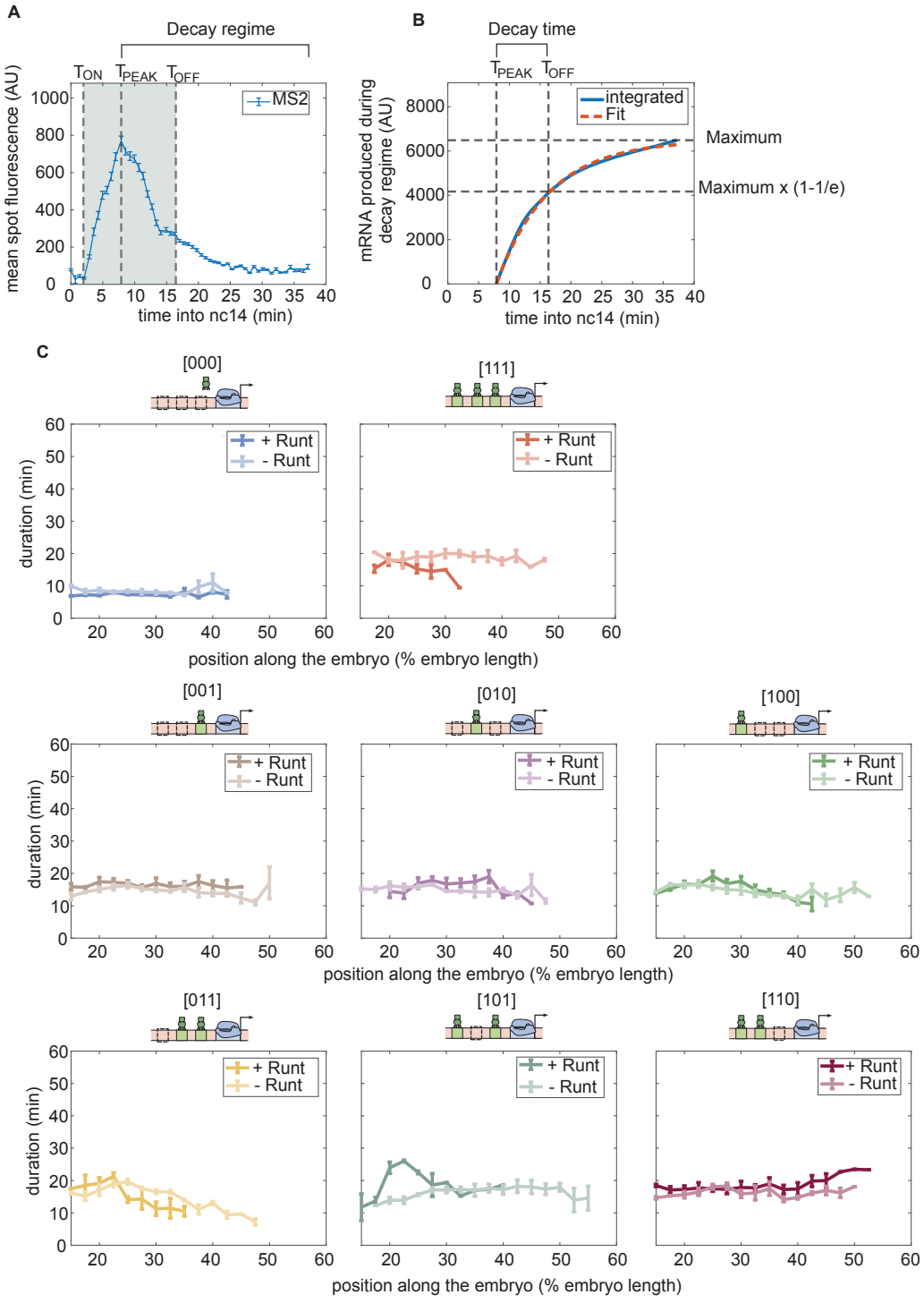

Figure S11: Durationof transcription over nc14. See Caption in the next page.

Figure S11: Duration of transcription over nc14. **(A)** An example MS2 time trace in nuclear cycle 14. The decay regime is defined from the peak of the signal to the end of the measurement. T_{ON} is defined by the x-intercept of the slope of the fitted line. T_{off} is determined by the decay time in the exponential function. The gray shaded region from T_{ON} to T_{OFF} is defined as the transcriptional time window. **(B)** The decay time can be extracted from the accummulated mRNA signal obtained by integrating the MS2 fluorescence. Here, decay time is defined as the time it takes to reach (1-1/e) of that maximum accumulated mRNA. **(C)** Transcriptional time window along the anterior-posterior axis for each construct with and without Runt protein. (A, error bars represent standard error of the mean over the spatial averaging corresponding to roughly ten nuclei; C, error bars represent standard error of the mean over ≥ 3 embryos.)

14. However, the remaining 20% of the loci never engage in transcription, which we termed as "incompetent loci". Because these two populations exhibit wildly different behaviors, we define the fraction of competent loci as

$$\text{fraction of competent loci} = \frac{\text{number of competent loci}}{\text{number of total loci}}. \tag{S21}$$

Thus, in this example in Figure S12A, the fraction of competent loci is approximately 0.8.

Figure S12B shows the measured fraction of active loci for all synthetic enhancer constructs in the presence and absence of Runt repressor. As seen in the figure, although this quantity can be modulated by the presence of Runt repressor, this is not always the case (e.g., [010] and [11]). Moreover, we could not find a trend for how the fraction of competent loci is modulated by different combinations of Runt binding sites. For example, the [100] construct alone did show a change in the fraction of active loci in the presence of Runt, whereas the [010] construct did not. When these two binding sites were combined as the [110], there was no significant modulation of the fraction of competent loci when adding Runt repressor. In another example, the [001] construct showed a mild modulation of the fraction of competent loci. However, when this Runt binding site was combined with the [010], which did not show any modulation, the [011] construct showed a much bigger modulation of the fraction of competent loci than the [001]. Thus, the [010] Runt binding site could drive more or less modulation of the fraction of competent loci when combined with different Runt binding sites in a context-dependent manner. As a result of our failure to uncover an apparent trend in terms of which regulatory architectures lead to a stronger modulation of the fraction of active loci, we did not attempt to theoretically explain the regulation of this fraction of active loci in this study.

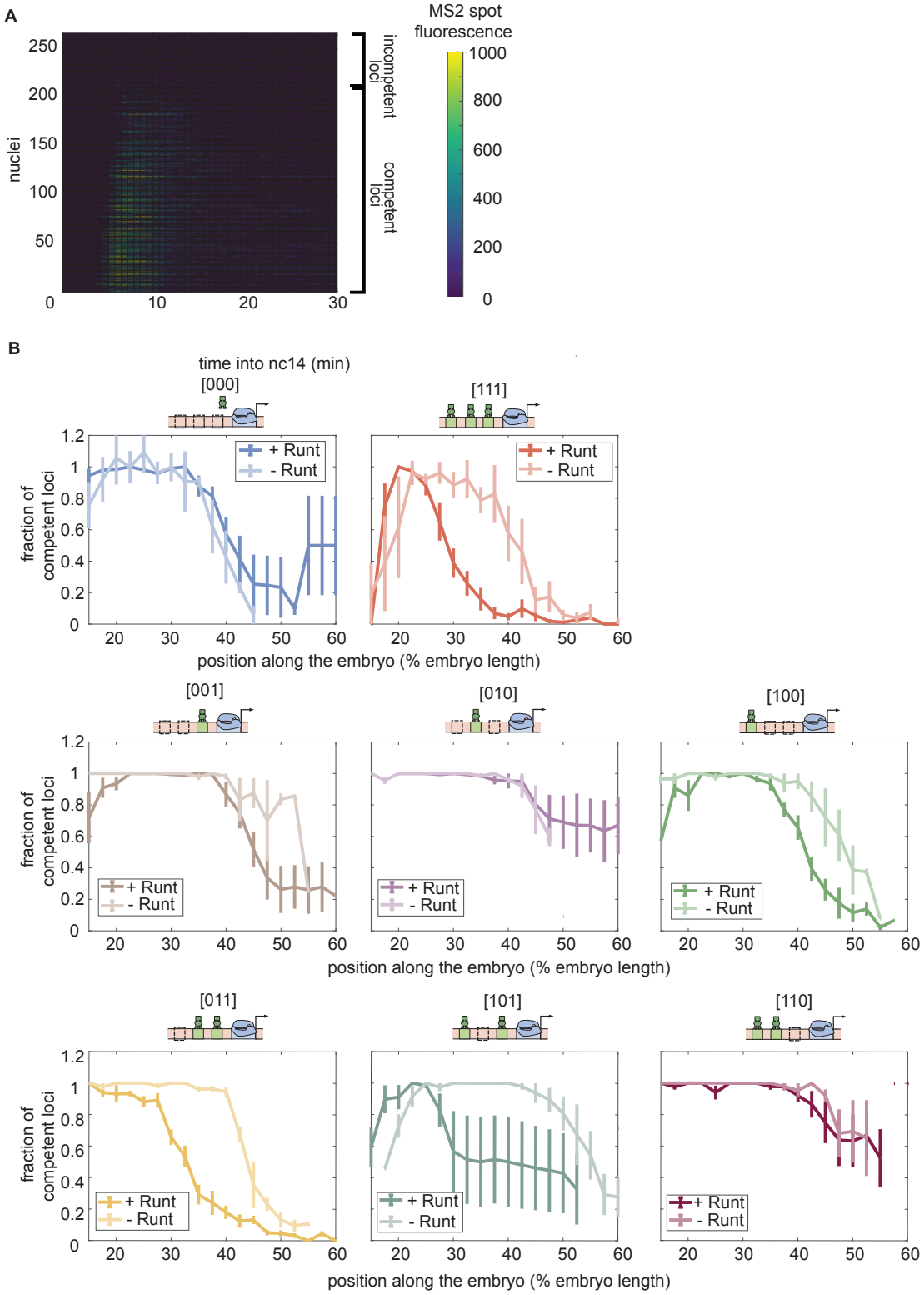

Figure S12: Fraction of competent loci in nuclear cycle 14 across the anterior-posterior axis for different constructs in the presence and absence of Runt protein. See caption in the next page.

Figure S12: Fraction of competent loci in nuclear cycle 14 along the anterior-posterior axis for each synthetic enhancer construct in the presence and absence of Runt protein. **(A)** Heatmap showing the transcriptional signal from the *hunchback* P2 enhancer for individual nuclei (rows) demonstrating that there are two populations of loci: transcriptionally active and inactive loci. **(B)** Fraction of transcriptionally active loci along the embryo for each construct for wild-type and runt null backgrounds. (B, error bars represent standard error of the mean over ≥ 3 embryos.)

S9 Supplementary figures

1

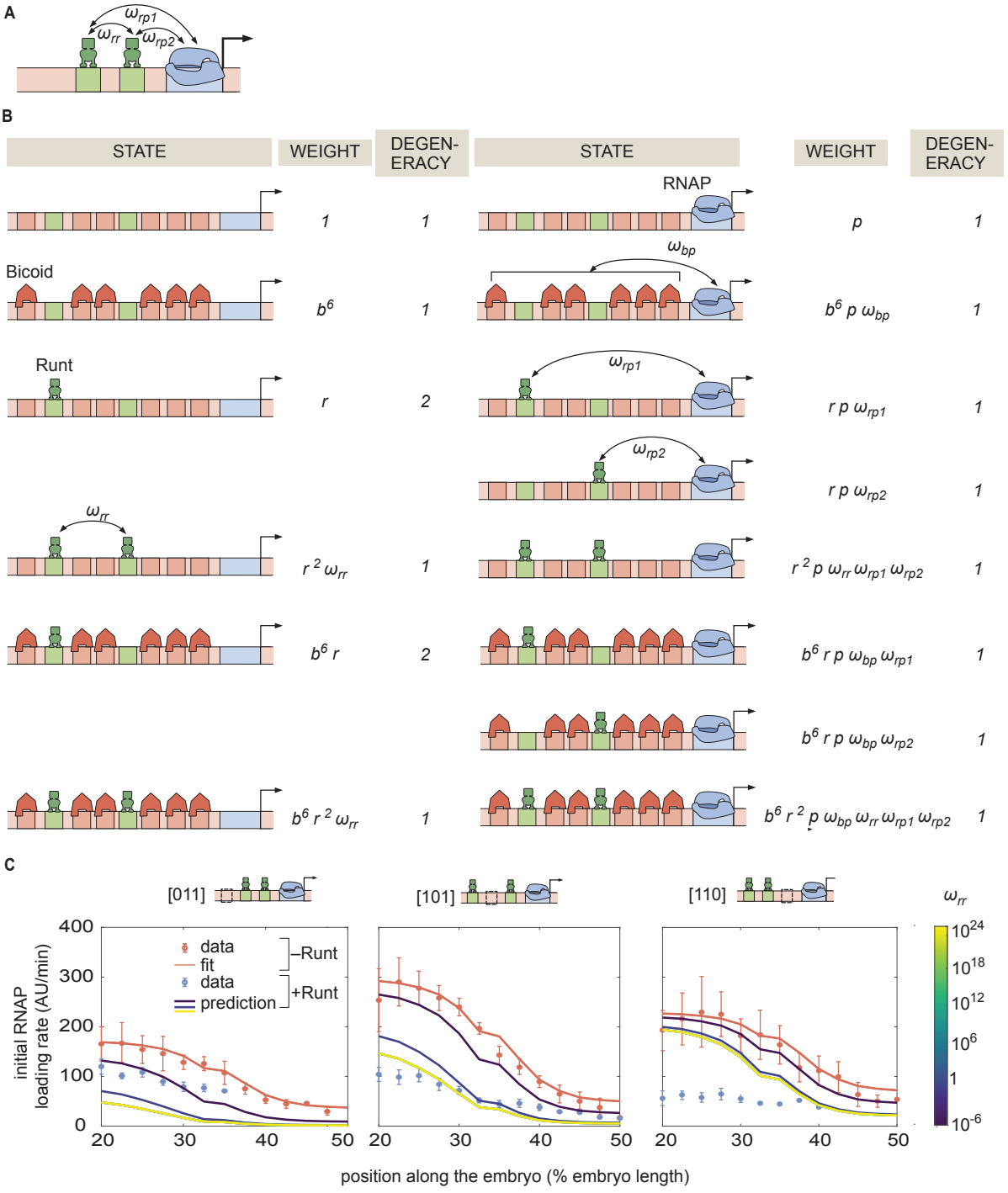

Figure S13: Invoking Runt-Runt cooperativity in the thermodynamic model is not sufficient to explain the experimental data from *hunchback* P2 with two Runt binding sites. See caption in the next page.

Figure S14: Invoking Runt-Runt cooperativity in the thermodynamic model is not sufficient to explain the experimental data from *hunchback* P2 with two Runt binding sites. **(A)** Model schematics where we add a new ω_{rr} parameter representing Runt-Runt cooperativity. **(B)** Corresponding states and weights for *hunchback* P2 with two Runt binding sites in the presence of Runt-Runt cooperativity. **(C)** Prediction of the initial rate of RNAP loading profiles over a range of Runt-Runt cooperativity strength, $\omega_{rr} = [10^{-6},\ 10^{24}]$, for all constructs of *hunchback* P2 with 2 Runt binding sites with different configurations. (Left) [011], (Center) [101], (Right) [110]. (C, error bars represent standard error of the mean over ≥ 3 embryos)

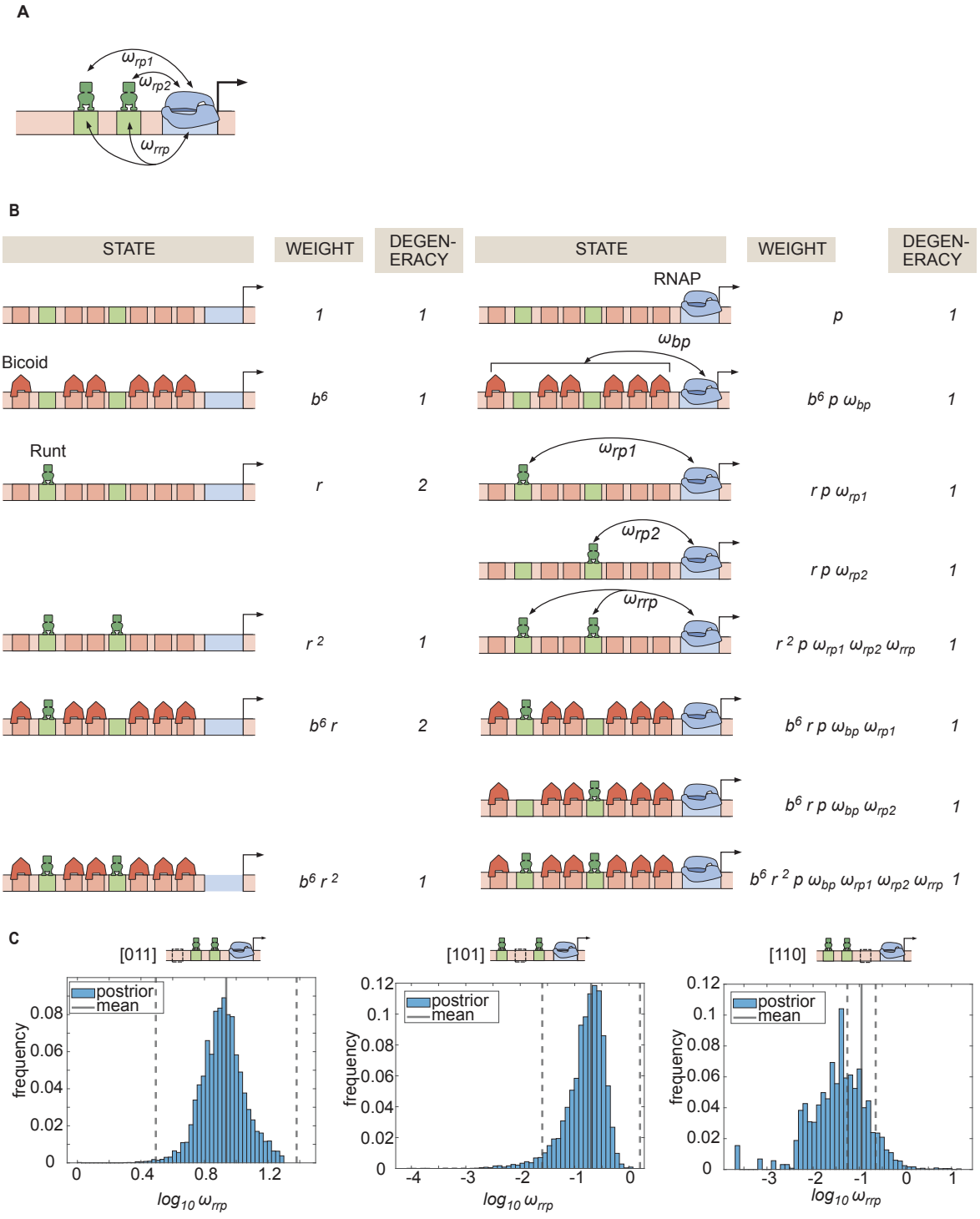

Figure S15: Invoking Runt-Runt-RNAP higher-order cooperativity is not sufficient to explain the two-Runt sites data. See caption in the next page.

Figure S15: Invoking Runt-Runt-RNAP higher-order cooperativity is not sufficient to explain the two-Runt sites data. **(A)** Schematics of a model where we add Runt-Runt-RNAP higher-order cooperativity represented by ω_{rrp}. **(B)** Thermodynamic model states and weights for *hunchback* P2 with two Runt binding sites in the presence of Runt-Runt-RNAP higher-order cooperativity. **(C)** Histograms showing the posterior distribution of the inferred ω_{rrp} parameter from the best MCMC fit shown in Figure 7D. The black line represents the mean and the dotted lines represent standard deviation from the mean.

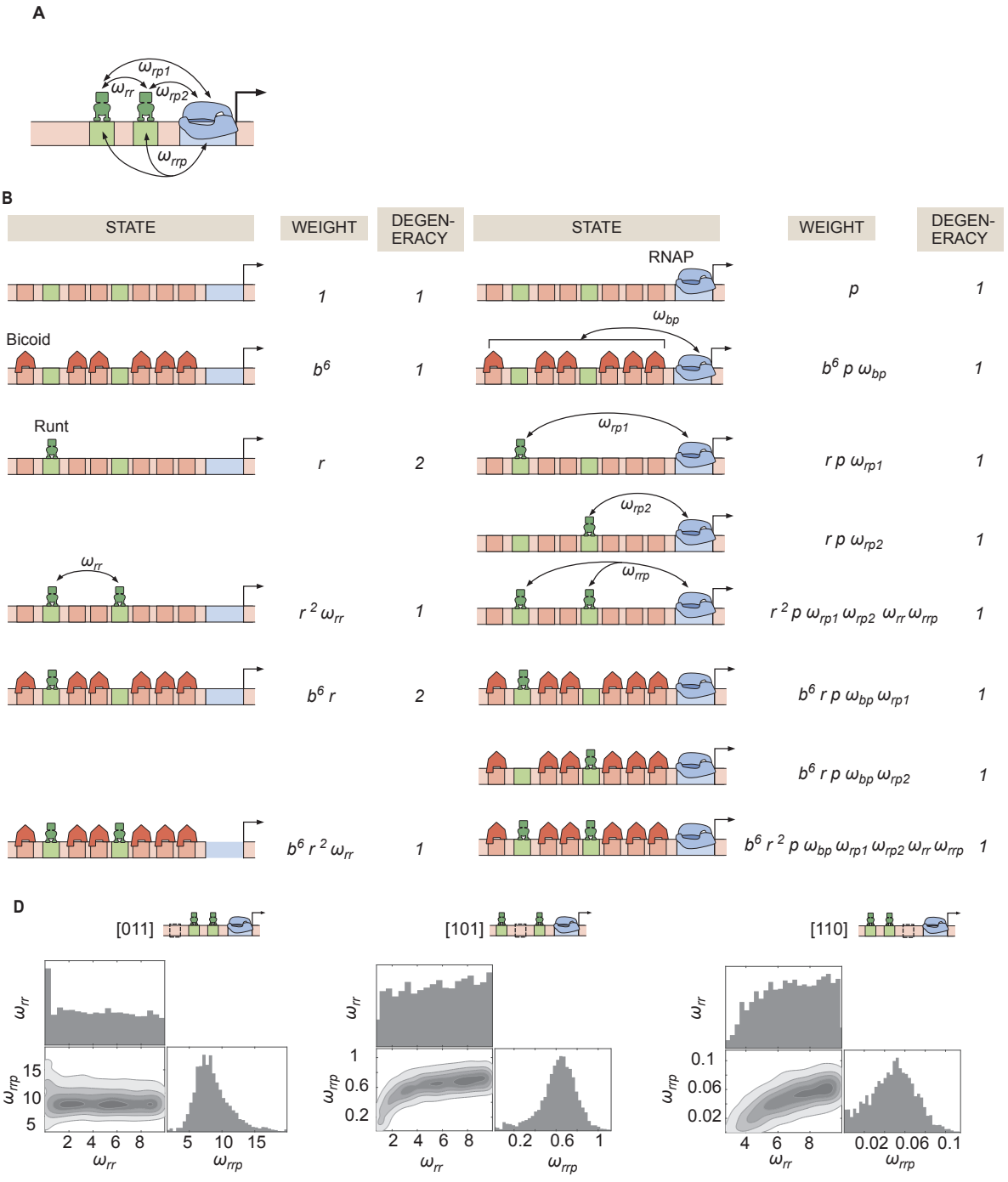

Figure S16: Invoking Runt-Runt cooperativity and higher-order cooperativity can explain the experimental data from *hunchback* P2 with two Runt binding sites. See caption in the next page.

Figure S16: Invoking Runt-Runt cooperativity and higher-order cooperativity can explain the experimental data from *hunchback* P2 with two Runt binding sites. **(A)** Schematic showing Runt-Runt cooperativity and higher-order cooperativity. **(B)** States and weights for *hunchback* P2 with two Runt binding sites with Runt-Runt cooperativity and higher-order cooperativity. **(C)** Corner plots associated with the MCMC inference performed on two-Runt binding sites data from the best MCMC fit shown in Figure 7E. While ω_{rr} is not very well constrained, ω_{ho} shows a unique optimal value.

S10 Supplementary videos

For better quality of visualization, we recommend downloading these videos.

S1. Video S1. **eGFP-Bicoid confocal movie.** Confocal microscopy movie taken on a developing fly embryo (*eGFP-Bicoid; His2Av-mRFP; +*) during nuclear cycle 13 and 14.

S2. Video S2. **eGFP:LlamaTag-Runt confocal movie.** Confocal microscopy movie taken on a developing fly embryo (*eGFP-Bicoid; His2Av-mRFP; +*) during nuclear cycle 13 and 14.

S3. Video S3. **[001]-MS2V5:MCP-GFP (+Runt) confocal movie.** Confocal microscopy movie taken on a developing fly embryo (yw; His2Av-mRFP; MCP-eGFP) for the [001] construct with MS2 reporter during nuclear cycle 13 and 14.

Chapter 3

Comparison of methods to quantify cytoplasmic mRNA concentration

1 Introduction

An accurate quantification method is essential in characterizing the patterns of transcription factors and their downstream gene products. One of the widely used techniques to measure the gene expression pattern is *in situ* hybridization - hybridizing the RNA of interest with the complementary DNA probes followed by tagging those complexes with fluorophores or enzymatic probes for characterization of the gene expression patterns. There are broadly two categories of *in situ* hybridization methods depending on the source of the signal:chemogenic and fluorogenic. The chemogenic method is called colorimetric *in situ* hybridization (which we refer to as *in situ* throughout this thesis). It relies on an enzymatic reaction such as horseradish peroxidase (HRP) with its substrate bound in the probe which generates luminescence (as showcased in Fig. 1A). The fluorogenic method is called fluorescence *in situ* hybridization (which we refer to as FISH), relying on fluorophores attached to the primary or secondary antibodies that bind to the DNA probe, thus generating a fluorescence signal that is proportional to the number of mRNA molecules (as showcased in Fig. 1B). These in situ hybridization methods could be multiplexed to detect multiple species of mRNA simultaneously (Chen et al. 2015). An alternative approach is tagging the nascent transcripts using the bacteriophage stem-loop structures such that the inserted sequence of MS2 (or PP7) forms a loop structure upon transcription which is then bound by bacteriophage coat proteins such as MCP (or PCP) fused to fluorescent proteins (Bertrand et al. 1998). This tagging system enables quantification of the number of nascent transcripts actively being transcribed in real-time by monitoring the MS2 *spots* as shown in Figure 1C (Garcia et al. 2013b). By integrating the MS2 spot fluorescence intensity over time, it is possible to calculate the accumulated mRNA quantity (Garcia et al. 2013b).

All of these methods mentioned above have different types of caveats. For example, *in situ* hybridization methods could be used for multiplexed detection of hundreds to thousands

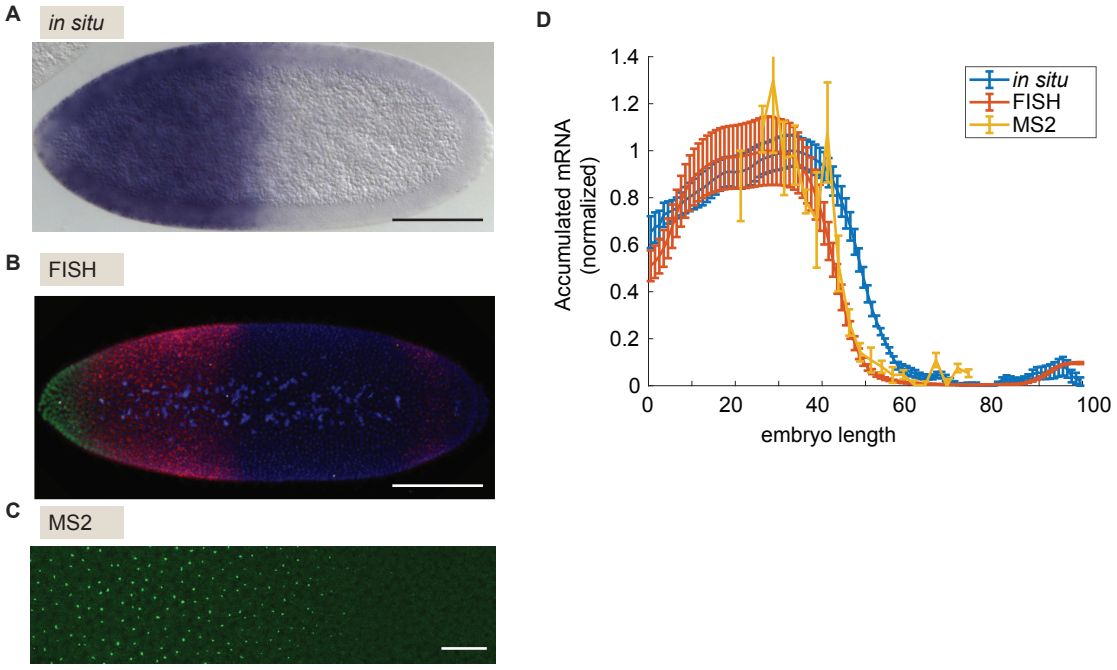

Figure 1: Experimental methods to measure the patterns of cytoplasmic mRNA. **(A,B,C)** Snapshot of fly embryos with mRNA expression driven by *hunchback* P2 enhancer in nuclear cycle 14. **(A)** colorimetric *in situ* hybridization. Scale bar represents $100\mu m$ **(B)** Fluorescence *in situ* hybridization (FISH) with the Alexa488 probe. Scale bar represents $100\mu m$. **(C)** MS2 with MCP-GFP. Green dots represent the loci of active transcription. The embryo image shows 20-60% of the embryo length along the anterior-posterior axis. Scale bar represents $20\mu m$. **(D)** Comparison of the patterns of cytoplasmic mRNA acquired from different experimental methods. The y-axis is showing the accumulated mRNA from each method normalized by the accumulated mRNA values at 20% of the embryo length.

of mRNA species, whereas stem-loop methods can detect two or three genes at a time. Also, while stem-loop methods enable the tracking of temporal dynamics in real-time at the single-cell level, the *in situ* hybridization methods require fixed samples, thus offering data from a snapshot. In my view, there is no perfect method in the world; instead, there is one method more suitable than the other in terms of throughput, ease of use, and accuracy. In this section, we will perform a comparative study for colorimetric in situ hybridization (*in situ*), fluorescence in situ hybridization (FISH), and MS2-MCP techniques to assess their accuracy in quantifying the cytoplasmic mRNA patterns in the fruit fly embryos.

To compare these three different methods in their ability to quantify the cytoplasmic mRNA patterns, we chose a well-characterized system of *hunchback* P2 enhancer that is known to drive a step-like pattern of mRNA (Perry, Boettiger, and Levine 2011). We used all three methods for the same construct that is driving transcription under the *hunchback* P2 enhancer. We observed a difference in the patterns of cytoplasmic mRNA between the three methods as shown in Figure 1D. Briefly, the FISH and MS2 data showed agreement while the *in situ* showed a more posteriorly shifted pattern. To further dissect this, we made a one-on-one comparison between these three methods. First, we reveal a striking disagreement in patterns of cytoplasmic mRNA between *in situ* hybridization and MS2 data. Specifically, when examining a *hunchback* step-like gene expression pattern, *in situ* patterns of accumulated mRNA have wider plateaus along the AP axis compared to those reported by MS2. We show that, by assuming saturation in the *in situ* signal, both *in situ* and MS2 measurements can qualitatively agree. Finally, we find that measurements by FISH and MS2 lead to similar results across the AP axis. Thus, we provide evidence that MS2 and FISH can capture a wider dynamic range of accumulated mRNA than *in situ* measurements, making them more appropriate for quantifying the pattern of gene expression. In conclusion, we revealed the pros and cons of different methods of quantifying the patterns of cytoplasmic mRNA, facilitating the choice of experimental method that is more suitable for one's specific scientific question.

2 Results

We started by making a one-to-one comparison of methods to quantify the cytoplasmic mRNA patterns. First, we compare *in situ* and MS2 using the constructs with *hunchback* P2 enhancer with differing number of Runt binding sites. Next, we compare MS2 and FISH by using the FISH data from Park et al. (2019). Lastly, we make a comparison between all three methods for *hunchback* P2 driven construct.

Comparison of accumulated mRNA pattern from *in situ* vs MS2

We compare the accumulated mRNA profiles during the nuclear cycle 13 and 14 for constructs with *hunchback* P2 enhancer with zero-, one-,two-, or three- Runt binding sites side-by-side in Figure 2 A and B. Here, each profile was normalized so as to compare the overall features of

the pattern such as boundary position and sharpness. As revealed by the Figure 2 C and F, there are significant differences in patterns between the mRNA profiles acquired with *in situ* and MS2-MCP.

We hypothesized that the difference between the two methodologies could stem from the fact that the signal from colorimetric *in situs* could saturate. To test this hypothesis, we incorporated saturation into our MS2 data by finding a saturation point that, after renormalization, can qualitatively match the data from the two techniques (Fig. 3B, black line). As shown in Figure 3C-F, after incorporating this saturation both measurements yield similar gene expression patterns for most constructs. Critically, for all constructs but r0, the boundary position and sharpness now become comparable. It is important to note that, in Figure 3, we are assuming the same saturation value for all *in situ* measurements. However, we speculate that this saturation value could fluctuate due to staining variability or variation in the illumination conditions, for example.

Comparison of accumulated mRNA pattern from FISH vs MS2

We compared MS2-MPC and FISH through measurements of a *hunchback* P2 enhancer and promoter driving *lacZ* (with MS2 repeats in the case of MS2-MCP), to take advantage of the data sets from the DePace lab. The FISH data that was acquired roughly five minutes into nuclear cycle 14. At this early time point in the nuclear cycle, transcription has not yet started. Thus, we assumed that they (Park et al. (2019)) measured accumulated mRNA up until NC13. The MS2-MCP datasets are from nine embryos spanning 20% to 80% of the embryo length. The profiles resulting from each method are shown in Figure 5 A and B, respectively. As shown in Figure 5 C, after normalization we could get qualitatively similar patterns of accumulated mRNA with the boundary position and sharpness being comparable.

Comparison of *in situ* vs FISH vs MS2

In the above sections, we have compared FISH vs MS2, and *in situ* vs MS2. In this section, we will try to compare all three methods for the accumulated mRNA profile in the early nuclear cycle 14. For FISH and MS2, we already have datasets for *hunchback* P2 enhancer and promoter, but we do not have datasets for the same construct with *in situ*. Thus, we assumed that the *hunchback* P2 with *even-skipped* promoter would drive similar pattern of expression as

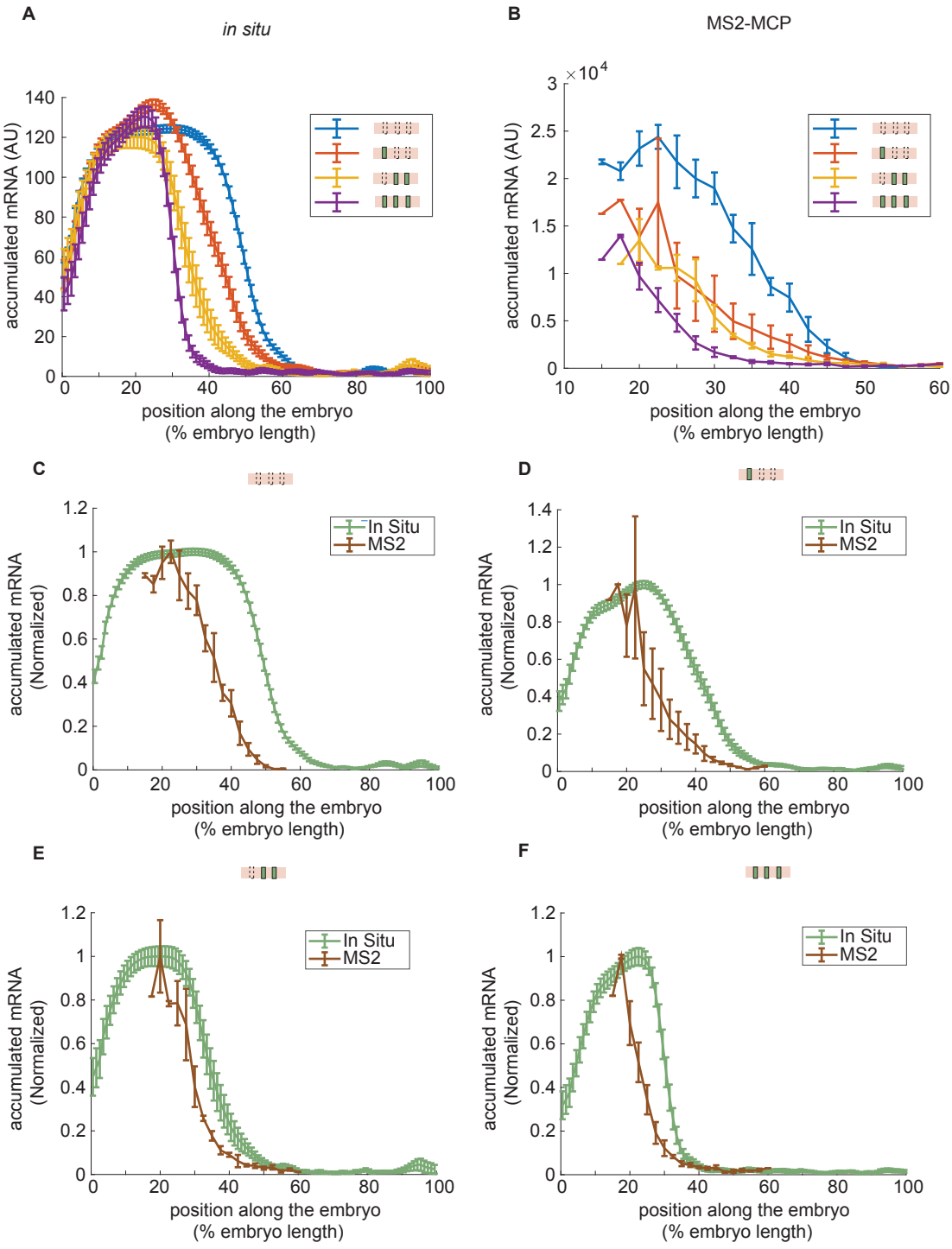

Figure 2: Comparison of accumulated mRNA profiles between *in situ* hybridization and MS2-MCP. See caption in the next page.

Figure 2: Comparison of accumulated mRNA profiles between *in situ* hybridization and MS2-MCP. **(A,B)** Accumulated (cytoplasmic) mRNA for *hunchback* P2 enhancer with differing number of Runt binding sites constructs acquired by (A) *in situ* hybridization and (B) MS2-MCP. **(C,D,E,F)** Comparison of normalized accumulated mRNA profile for each construct shown in (A) and (B). Schematics of each construct is shown at the top of each plot.

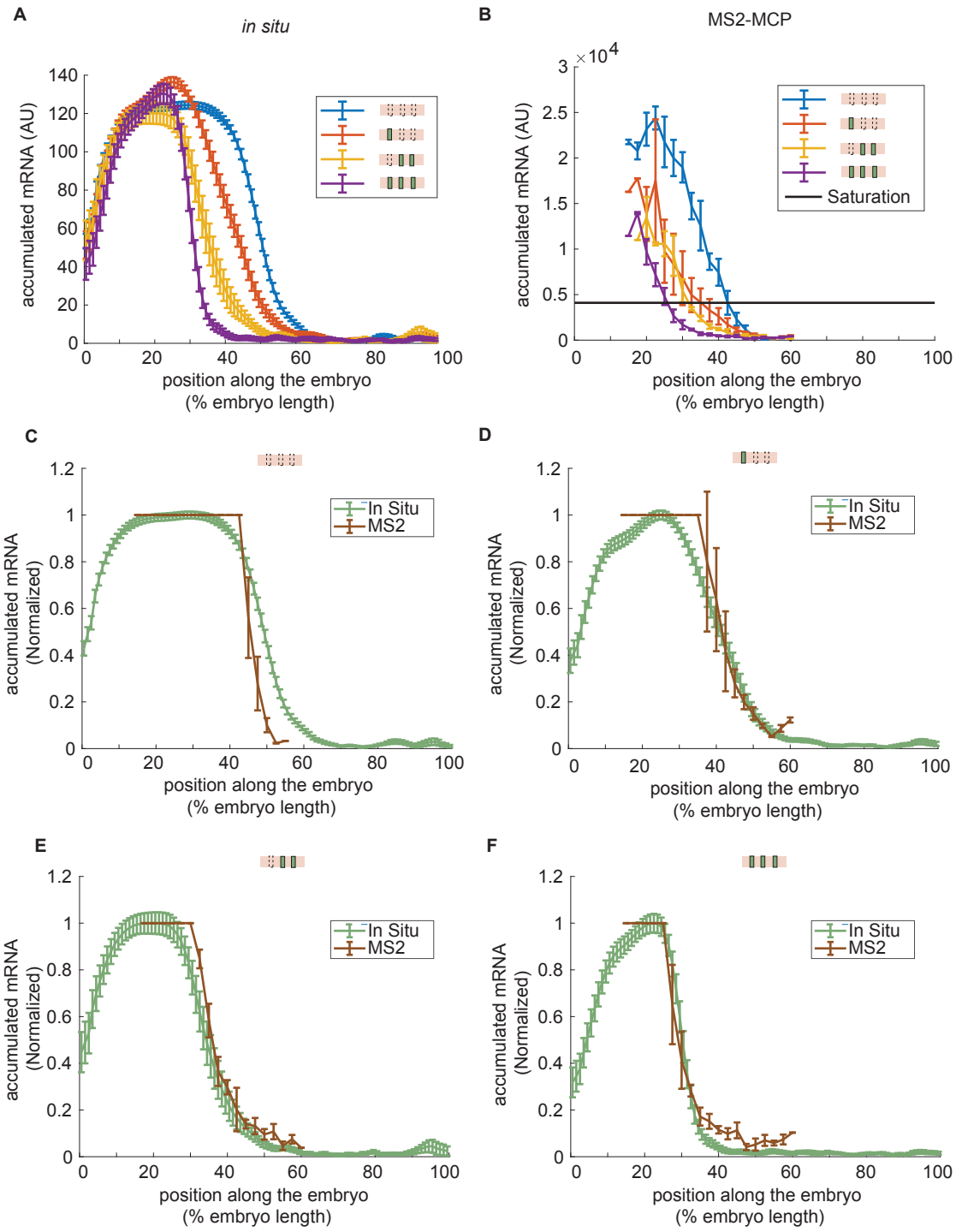

Figure 3: Comparison of accumulated mRNA profiles between *in situ* hybridization and MS2-MCP assuming there is saturation in the *in situ* data. See caption in the next page.

Figure 4: Comparison of accumulated mRNA profiles between *in situ* hybridization and MS2-MCP assuming there's saturation in the *in situ* data. **(A,B)** Accumulated mRNA profiles for the *hunchback* P2 enhancer constructs with zero-, one-, two-, or three-Runt binding sites acquired by (A) *in situ* hybridization and (B) MS2-MCP. In (B), a saturation point is chosen such that the renormalized profiles from the two methods become comparable. Accumulated mRNA values larger than this saturation point are set to this saturation value. **(C,D,E,F)** Comparison of re-normalized accumulated mRNA profile for *hunchback* P2 enhancer with (C) zero-Runt site, (D) one-Runt site, (E) two-Runt sites, (F) three-Runt sites.

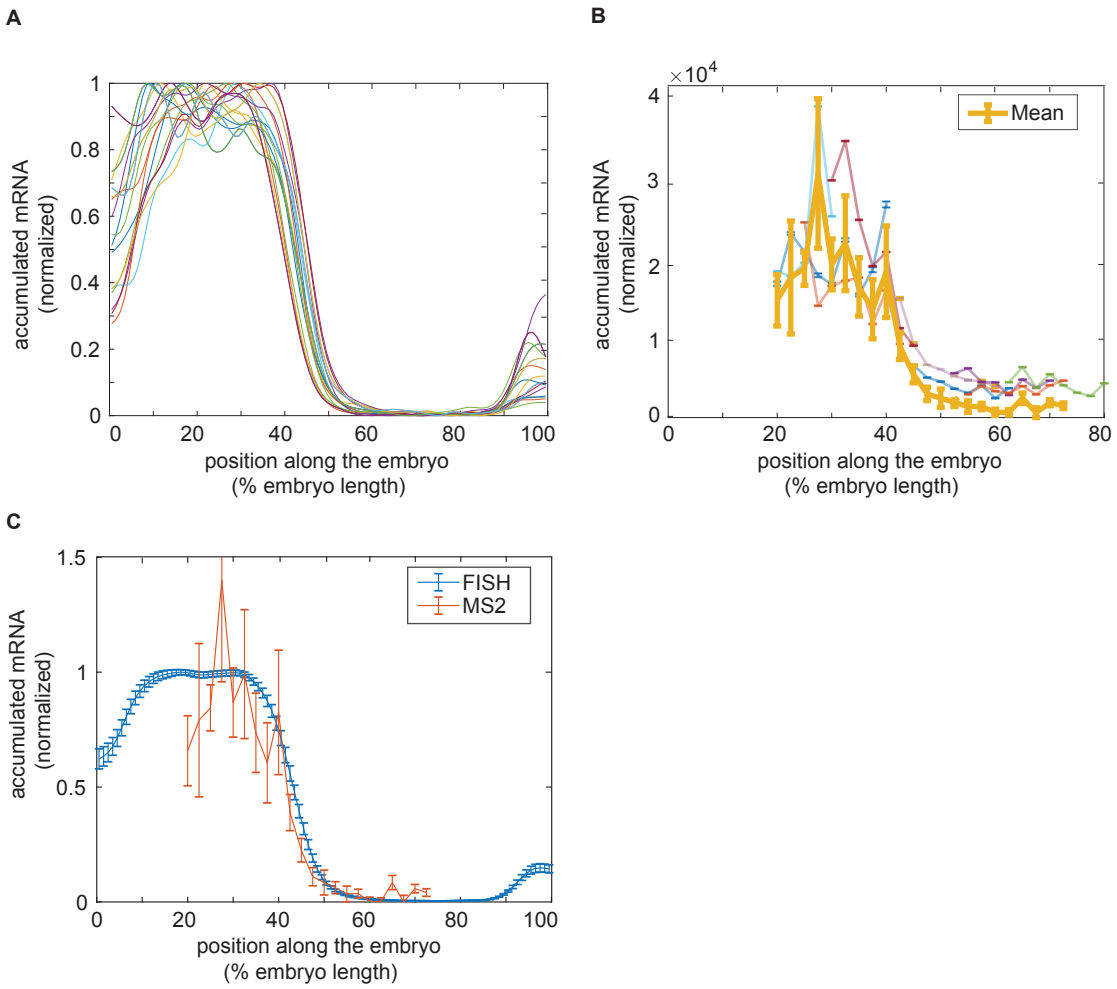

Figure 5: Comparison of accumulated mRNA profiles measured by FISH and MS2. **(A)** Accumulated mRNA (FISH intensity) from P2P construct from individual embryos (Park et al. 2019). **(B)** Accumulated mRNA (accumulated fluorescence) by MS2 technique from the *hunchback* P2 enhancer and promoter construct. The yellow curve shows the mean and standard error of the mean (SEM) over 9 embryos. (C) Mean profile of accumulated mRNA from FISH and MS2.

Chapter 4

Development of live-imaging toolkits for monitoring translation dynamics in developing fly embryos

1 Introduction

Translational control is a widely used strategy to regulate gene expression across different cell types and organisms. This regulation is especially relevant for biological systems where local control of protein accumulation is needed such as developing syncytial embryos or neuronal synapses (Gebauer and Hentze 2004).

In the context of developing embryos, translational regulation has been studied primarily focusing on understanding how the spatial patterns of transcription factors emerge. One of the most well-known examples of translational regulation is the regulation of maternal gradients in the early fruit fly embryo. For example, *caudal* mRNA is supplied maternally with a uniform distribution along the embryo's anterior-posterior axis. The translation of *caudal* mRNA is repressed by Bicoid, which forms an exponentially decaying gradient along the anterior-posterior axis. Thus, Bicoid represses the translation of *caudal* mRNA mainly at the anterior pole, leading to an opposite gradient of Caudal protein which peaks at the posterior and decreases towards anterior as shown in Figure 1.6 A and B. Another well-studied example is the translational regulation of maternal *hunchback* mRNA. Unlike zygotic *hunchback* mRNA whose expression pattern is a step-like, which resembles that of the Hunchback protein pattern, the maternal *hunchback* mRNA is distributed uniformly along the anterior-posterior axis of the embryo. The maternal gene *nanos* is expressed in a protein concentration gradient which is high in the posterior end of the embryo and low in the anterior end. Nanos protein is known to bind to the 3'UTR of the *hunchback* mRNA via Pumilio. Nanos protein represses the translation of maternal hunchback mRNA, which leads to a step-like expression pattern emerging from uniform mRNA distribution along the anterior-posterior axis (Murata and Wharton 1995; Wharton et al. 1998). Although it is

known that protein levels are downregulated by these translational repressors (either Bicoid or Nanos), the molecular mechanism by which this repression is achieved still remains elusive. For example, there could be different strategies to achieve an equivalent level of translational repression: either regulating the rate of translational initiation or elongation, the fraction of mRNA engaged in translation, or any combination thereof as shown in Figure 1.6 C (Vinter et al. 2021).

In order to determine which scenario is at play in the regulation of translation, we need a tool to monitor and quantify translation dynamics at the single ribosome level. To fluorescently label nascent polypeptides, we used the recently developed SunTag system. This system consists of repeated peptides (SunTag) inserted into the N-terminal of the protein of interest that can be bound by a single-chain variable fragment of an antibody (scFv) fused to fluorescent proteins (shown in Fig. 1.7 A and B) (Tanenbaum et al. 2014; Yan et al. 2016). Recent studies in the early fruit fly embryos using the SunTag reporter system reported on the spatio-temporal heterogeneities in translational dynamics, such as along the apical-basal axis (Dufourt et al. 2021) or along the anterior-posterior axis (Vinter et al. 2021). Briefly, Dufourt et al. (2021) reported that the translation efficiency (number of actively translating ribosomes per mRNA molecules) of *twist* mRNA is higher in the basal region of the embryo compared to the apical region. Additionally, Vinter et al. (2021) revealed that *hunchback* mRNA translation is also under regulation along the anterior-posterior axis, in this case, by modulating both the number of ribosomes associated with single mRNA molecules and the fraction of mRNA molecules that engage in translation. These studies have revealed that translation could be under regulation whose exact molecular mechanisms or quantitative details still remain unclear.

Our initial goal was to implement the SunTag system in fruit fly embryos by plugging in the SunTag sequences in a synthetic gene cassette with the PP7 sequences for tethering the mRNA (Yan et al. 2016). We chose the *hunchback* P2 minimal enhancer as the driver, as its mRNA pattern is very well characterized thus could be used as a platform to dissect the translational pattern (Perry et al. 2012). We used scFv fused to sfGFP to quantify the SunTag translation and PCP-mCherry with CAAX motif that binds to the plasma membrane to visualize and tether the mRNA molecules (Yan et al. 2016).

Our preliminary results are promising: we could see a punctuated signal in the SunTag-scFv channel that recapitulated the step-like *hunchback* pattern along the anterior-posterior axis. Next step, we sought to image this construct over time during nuclear cycle 14. Some representative time traces showed downregulation of transcription over time in nuclear cycle 14, which is consistent with Vinter et al. (2021).

Upon validation of the SunTag approach, we aimed to quantitatively dissect the differential translation dynamics controlling *caudal* and maternal *hunchback*. Specifically, we generated SunTag reporter constructs whose gene cassettes are followed by different 3'UTR sequences, such as *caudal* or maternal *hunchback*. As a control we used the 3'UTR sequence whose translation is not known to be regulated in space and time, such as *α-tubulin*. The characterization of these constructs was not done yet, thus I only summarize our current state of the project for future references.

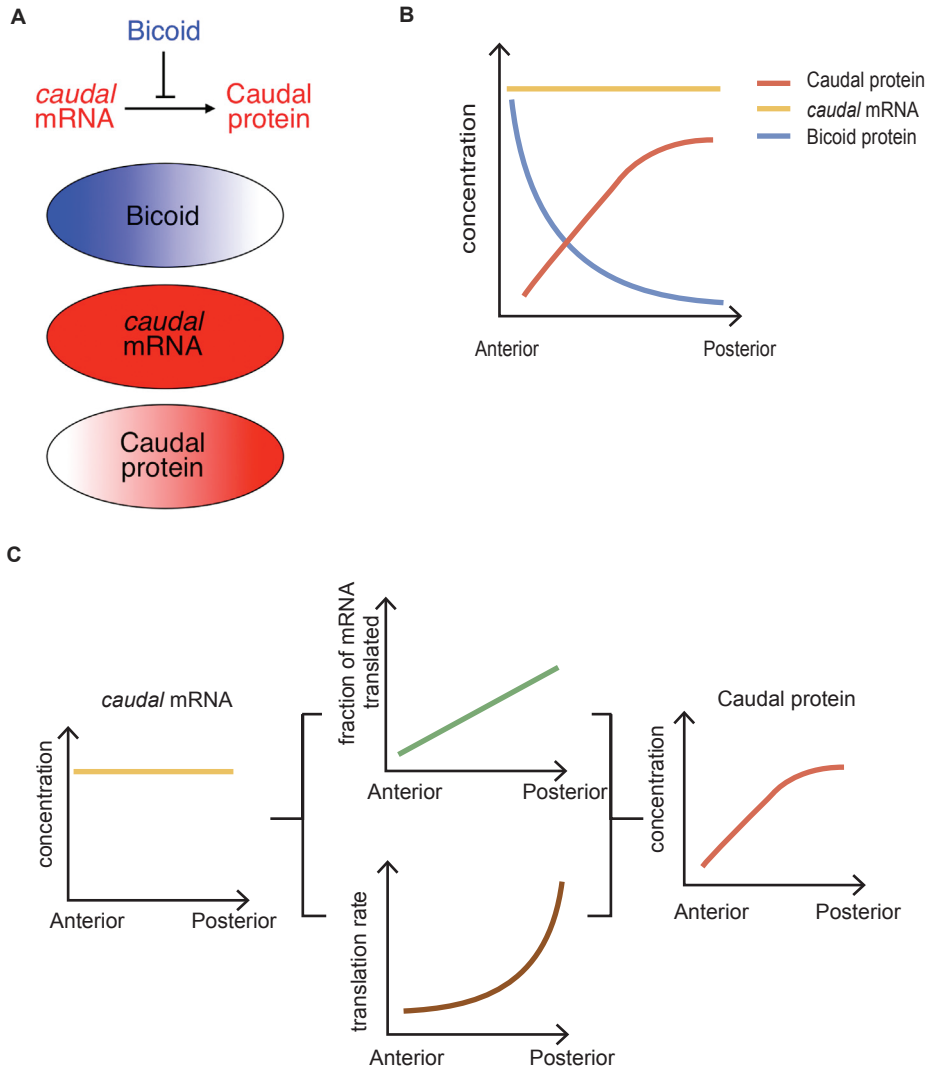

Figure 1: Translational regulation generates a spatial protein gradient out of a spatially uniform mRNA pattern. **(A)** An example of translational repression of *caudal* mRNA by Bicoid protein. Bicoid protein is expressed in an exponentially decaying gradient along the anterior-posterior axis of the embryo. *caudal* mRNA is supplied maternally and distributed uniformly along the anterior-posterior axis. Bicoid protein represses the translation of the *caudal* mRNA, thus generating the spatial gradient of the Caudal protein. (A) is adapted from (Rödel, Gilles, and Averof 2013). **(B)** A schematic figure of the concentration profiles along the anterior-posterior axis of the fly embryo for *caudal* mRNA, Bicoid protein, and Caudal protein. **(C)** Different strategies to achieve translational repression. Either the rate of translation or the fraction of mRNA translated (or both) could be under regulation by Bicoid to achieve the spatial gradient of the resulting Caudal protein.

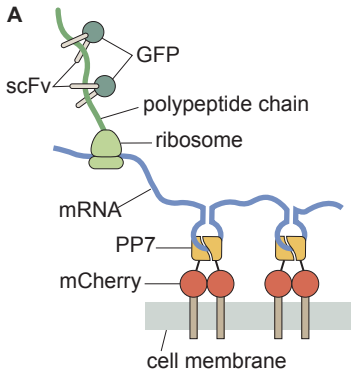

Figure 2: SunTag enables visualizing nascent loci of translation and quantifying the number of nascent polypeptides. **(A)** Schematics of the SunTag:scFv-GFP to tag the nascent polypeptides and PP7:PCP to tether the mRNA to the cell membrane. Usually, tethering is done for more extended tracking of the loci. **(B)** A series of snapshots of the SunTag:scFv-GFP, PP7:PCP with a reporter construct with SunTag over 30 minutes. Two example time traces from translation puncta are shown at the bottom. (B) is adapted from Yan et al. (2016).

2 Results

Establishing the SunTag reporter system in the early fly embryos

To establish the SunTag reporter system in the early fly embryos, we generated the fluorescent protein components for visualization of nascent polypeptides as well as mRNA molecules. To visualize the SunTag and individual mRNA molecules, we expressed a single-chain variable fragment (scFv) fused to sfGFP, and PCP fused to mCherry and CAAX tag to tether the reporter mRNA to the membrane (Yan et al. 2016). As our initial trial, we chose to drive these two components using independent constructs driven by a *nanos* promoter as shown in Figure 3 A (Garcia et al. 2013b). This promoter ensures sufficiently high levels of maternal protein expression in the early embryos as shown in Figure 3 B. Briefly, in the absence of the SunTag reporter, we could observe scFv-sfGFP uniformly distributed across nuclei and the cytoplasm. Additionally, we could clearly see cellular boundaries with membrane-tethered PCP-mCherry-CAAX. Interestingly, we could see this cellular boundaries during early nuclear cycles such as nuclear cycle 12 or 13 which are known to be syncytial and before complete cellularization occurs. We suspect that the cell membrane precursors form as early as nuclear cycle 12 or 13, yet we do not know how stable these structures are.

We then tested the SunTag reporter construct driven by the *hunchback* P2 minimal enhancer (Fig. 4 A). The hunchback mRNA pattern has been extensively characterized Perry et al. (2012) and thus could be used as a platform to dissect the underlying translational

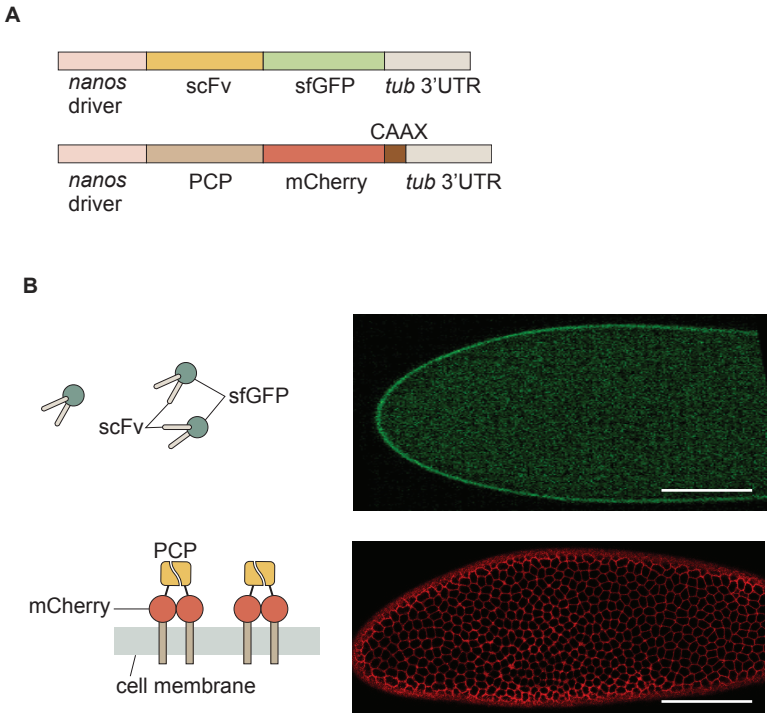

Figure 3: Establishment of fluorescent protein components for the SunTag system. **(A)** Schematics of the constructs expressing either scFv-sfGFP or PCP-mCherry-CAAX under the maternal *nanos* driver. **(B)** Example snapshots of fly embryos expressing either scFv-sfGFP (Top) or PCP-mCherry-CAAX (Bottom). Scale bars represent $100\mu m$.

pattern .

Our promising preliminary data showed a punctuated signal in the SunTag-scFv channel that recapitulated the step-like *hunchback* mRNA pattern along the anterior-posterior axis. This pattern did not exist in the control embryo lacking the *hunchback* driven SunTag reporter but containing scFv-sfGFP and PCP-mCherry-CAAX (Fig. 4 B). As the next step, we sought to image the temporal dynamics reported by our construct. Some representative time traces showed down regulation of translation over time in nuclear cycle 14, which is consistent with previous measurements of hunchback translational dynamics Vinter et al. (2021) (Fig. 4 C and D).

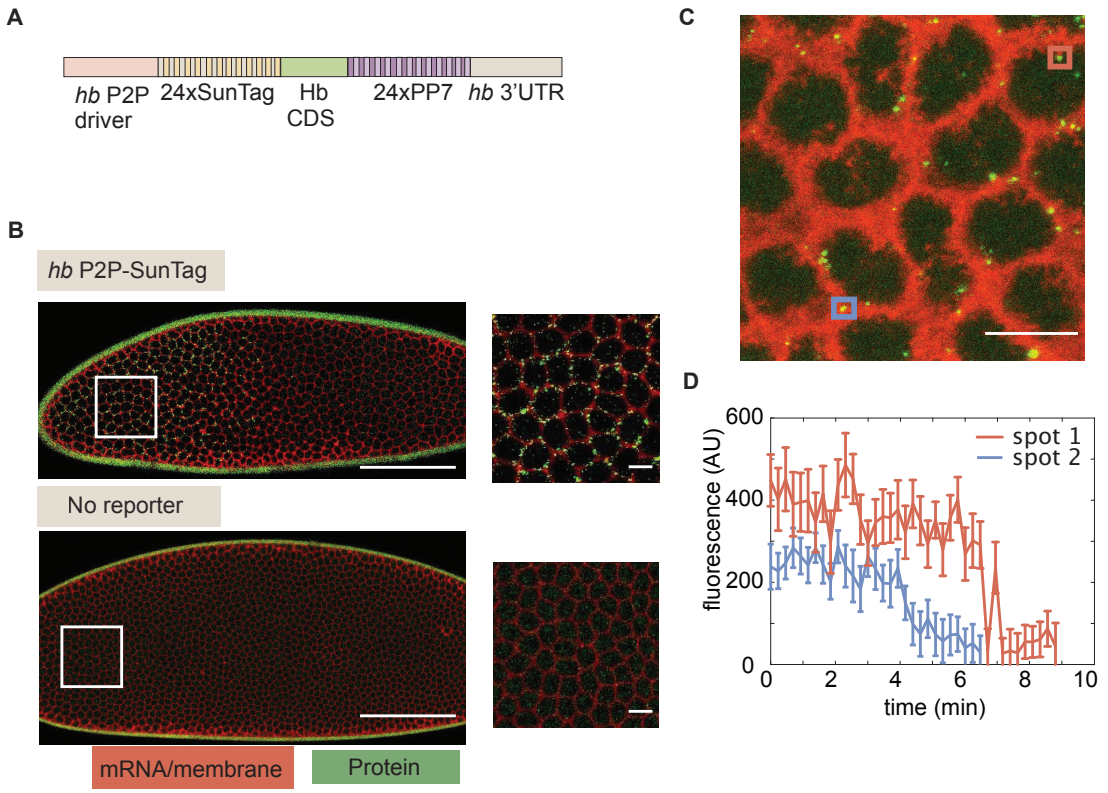

Figure 4: Proof-of-principle: *hunchback* P2P driven SunTag reporter recapitulatedsthe step-like spatial pattern of *hunchback* mRNA and captures its translational dynamics. **(A)** Schematics of the reporter constructs. The *hunchback* P2P driver is followed by 24 repeats of SunTag, the *hunchback* coding sequence, 24 repeats of PP7 loops, and the *hunchback* 3'UTR. PP7 loops are used to tether the mRNA molecules to the membrane and simplify live imaging. **(B)** Snapshots of embryos with or without the SunTag reporter shown in (A). (Top Left) A full embryo snapshot with the SunTag reporter and (Top Right) a zoomed-in image from the white squared region in the full embryo image. (Bottom Left) A full embryo snapshot without the SunTag reporter and (Bottom Right) a zoomed-in image from the white squared region in the full embryo image. Scale bars on the full embryo images represent $100\mu m$. Scale bars on the zoomed-in images represent $10\mu m$. **(C)** A zoomed-in image of the *hunchback*P2P driven SunTag construct with scFv-sfGFP and PCP-mCherry-CAAX. The green puncta represent the nascent loci of translation, and the membrane is marked with PCP-mCherry-CAAX. Blue and Red squared regions mark two nascent loci of translation whose temporal dynamics are shown in (D). **(D)** Time traces of the two loci of translation over 10 minutes in nuclear cycle 14. The two spots were chosen from the movie shown in (C).

Construction of synthetic reporter constructs with different 3' UTRs

After we validated the SunTag approach, we sought to dissect the molecular mechanisms of translational regulation corresponding to different 3'UTRs. As mentioned in the introduction, we chose the 3'UTR sequences of *caudal* and *hunchback* maternal transcripts as our initial targets. For controls, we chose the 3'UTRs of *tubulin* and *hunchback* zygotic transcripts respectively. We used the *bicoid* maternal driver to drive moderate levels of mRNA and prevent potential crowding of the mRNA molecules. Such crowding could complicate our detection of translation events from single, individual mRNA molecules (Hannon, Blythe, and Wieschaus 2017). Our construct design is illustrated in Figure.XX.

Further dissection of these constructs remains as future work. For example, we can start by acquiring the snapshots at different positions along the embryo's anterior-posterior axis for different nuclear cycles. This could narrow down when and where exactly we need to look at to see the translational repression either driven by Bicoid or Nanos for *caudal* or maternal *hunchback* 3'UTRs respectively. After we get a better sense of when and where in the embryo the translational repression is prominent, we could focus on those for further investigation of the temporal dynamics of translation. We envision that the translational repression for *caudal* 3'UTR would be more prominent in the earlier cycles, such as nuclear cycle 12 or 13 as the Bicoid protein level decreases over nuclear cycle 14.

3 Discussion

Translational dynamics studies have greatly progressed with the development of new live-imaging tools that make it possible to monitor the translation event in real-time at single-molecule scale (Tanenbaum et al. 2014; Yan et al. 2016). These technological advances have revealed the inherent stochasticity in translation process that gives rise to heterogenous translation in the absence of any specific regulation (Yan et al. 2016). The application of these techniques to multicellular organisms have revealed similar translational heterogenieties as well as unknown translational regulation along the apico-basal and anterior-posterior axes (Dufourt et al. 2021; Vinter et al. 2021).

Building on the research summarized above, we implemented the SunTag system in the early fly embryos. However, we found a number of technical challenges that we have yet to overcome. One of the biggest challenges was that it was hard to identify individual mRNA molecules from the PCP-mCherry channel. This lack of single mRNA resolution probably stems from the high background level of expression of the PCP-mCherry. We tried different maternal drivers (such as *vasa* or multimerized version of minimal *vasa* driver) that are known to drive lower level of protein expression, but with no luck. Briefly, 1x*vasa* driver drove almost no PCP-mCherry, whereas with 2x*vasa* driver drove too high of PCP-mCherry. Thus, we probably need more fine-tuning of the protein expression level to find the sweet spot where we can detect individual mRNA molecules. The fact that we cannot be certain

that the fluorescence signal from each individual translational locus comes from individual mRNA molecules complicates our interpretation of the data. For example, the fluorescence intensity from the translational spots could stem from one, two, or multiple mRNA molecules. However, we can still quantitatively assess the amount of translated peptides over time and space which already gives new insights on the spatio-temporal translational dynamics and regulation encoded by the different 3'UTR sequences.

Secondly, imaging translational loci over a long time period requires tethering of the mRNA to the membrane such that we do not lose track of the loci due to the diffusion of mRNA molecules (Vinter et al. 2021). Although this tethering strategy was shown to be effective for long-term imaging (Vinter et al. 2021), it is unclear whether this tethering could impact the translational dynamics that we are interested in. For example, tethering to the cytoplasmic membrane brings mRNA to the inner border of the cell, which could have a different microenvironment for translation than the cytoplasm in terms of, for example, the availability of the translational machinery. Further characterization of the translational dynamics between tethered and untethered mRNA molecules could shed light on this potential issue.

4 Materials and Methods

Construct Design

We used Genscript's Gene Synthesis service to generate all plasmids used for this study. The transgene cassettes were synthesized and subcloned into the pBphi vector with an attB site such that we could insert the transgene cassette into VK landing sites (Venken and Bellen 2007).

All of the plasmids that were generated from this study can be found in Benchling folder, `https://benchling.com/garcialab/f_/Z8JML0RT-translation-reporter/`.

Generation of transgenic fly lines

The transgenic fly lines were generated by Bestgene's plasmid injection and screening services. Briefly, the pBphi plasmids were injected into the fly lines carrying VK landing sites (Venken and Bellen 2007).

For the *hunchback* P2P driven SunTag reporter, we chose the VK33 site as this site has shown good level of expression from our previous studies (unpublished). For *bicoid* driven SunTag reporters with different 3'UTRs, we made two variants, VK33 and VK20, expecting to see some titration in case we want weaker expression for easier segmentation of the translational loci.

We inserted scFv-sfGFP and PCP-mCherry-CAAX into the same chromosome (chromosome II) for easier fly husbandry. The scFv-sfGFP transgene was inserted into the VK02 site and the PCP-mCherry-CAAX transgene was inserted into the VK22 site. These two VK sites

which are known to have orange eye color, rather than dark red. As a result, recombination to combine these two constructs into the same chromosomes could be done by screening for the red eyes resulting from the simultaneous presence of the two transgenes. For recombination, we crossed these two lines, did single-fly crosses with balancers, then screened for darker red eyes. Although not all of the darker red eyed fly lines carried both transgenes, we could confirm that more than 50% of the fly lines that we screened for indeed have both transgenes.

Sample preparation and data collection

Sample preparation was done following the protocols described in **?**. Briefly, embryos were collected, dechorionated with bleach for 1-2 minutes, and then mounted between a semipermeable membrane (Lumox film, Starstedt, Germany) and a coverslip while embedded in Halocarbon 27 oil (Sigma-Aldrich). Live imaging was performed using a Leica SP8 scanning confocal microscope, a White Light Laser and HyD dectectors (Leica Microsystems, Biberach, Germany). Imaging settings for the SunTag experiments with the presence of scFv-sfGFP and PCP-mCherry-CAAX were the same as in **?** except that we used 512x512 (pixels) format with a tiling option to image a wider field of view along the anterior-posterior axis.

Image Analysis

Images were analyzed using custom-written software (MATLAB, mRNA Dynamics Github repository) following a simpler version of the protocol in **?** and **?**. Briefly, this procedure involved segmentation and tracking of translational spots (from SunTag and scFv-sfGFP). First, segmentation of each transcription spot was done based on its fluorescence intensity and existence over multiple z-stacks. The intensity of each SunTag:scFv-sfGFP translational spot was calculated by integrating pixel intensity values in a small window around the spot and subtracting the background fluorescence measured outside of the active translational locus. When there was no detectable translational activity, we assigned NaN values for the intensity. The tracking of translational spots was done by using the proximity of translational spots between consecutive time points.

Chapter 5

A theory-experiment dialogue to connect patterns of transcription and translation

1 Introduction

So far, we have looked into different steps along the Central Dogma, from a set of transcription factors binding to a regulatory DNA sequence to drive transcription initiation, leading to the accumulation of mRNA molecules forming a gene expression pattern along the embryo's body axes, which then leads to a pattern of protein which acts onto the gene regulatory network. Classic developmental biology work has treated the patterns of transcripts and protein as almost equivalent. Only recently, it was proposed that this is not always the case, especially with novel techniques revealing the translational regulation (Fig. 1 A) (Surkova et al. 2019). In this chapter, we connect quantitative measurements of transcription and translation under the reaction-diffusion modeling framework (Jaeger et al. 2004).

The reaction-diffusion model was proposed by Alan Turing to explain pattern formation in nature: patterns of stripes or spots emerging autonomously from homogeneous, uniform state (Turing 1952). A widespread application of the reaction-diffusion model in the fruit fly embryo is the so-called Synthesis, Degradation, and Diffusion (SDD) model (Gregor et al. 2007a). This model has been used to explain pattern formation of a maternal gene, *bicoid*.

Inspired by the SDD modeling framework, we wondered to which degree we could explain the protein pattern solely from the knowledge of mRNA patterns. Moreover, we wanted to challenge the SDD model by generating experimentally testable predictions. For example, the widespread SDD model assumes static parameters (such as diffusion coefficients, synthesis or degradation rates for mRNA or protein (Gregor et al. 2007a). By contrasting the predictions generated from this simple assumption with quantitative data, we can test this widespread assumption.

The SDD model has parameters as follows: synthesis and degradation of both mRNA and

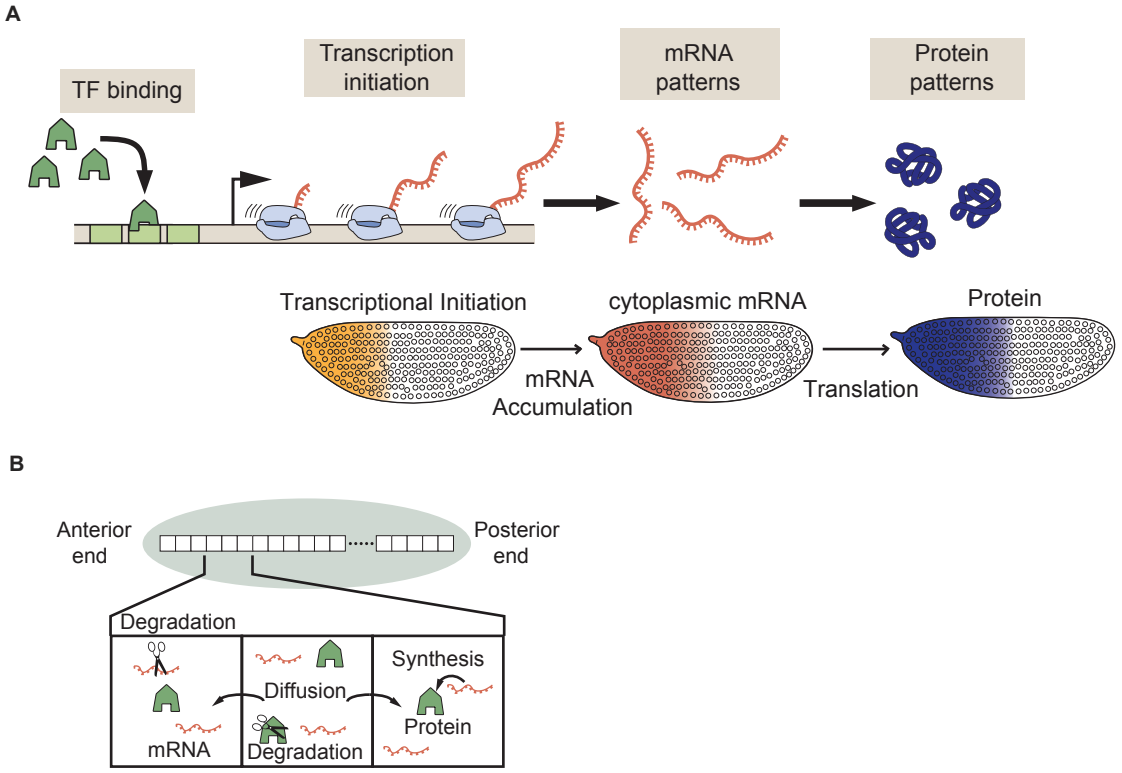

Figure 1: Conceptual framework to predict protein patterns from transcriptional initiation patterns using the reaction-diffusion model. **(A)** Schematic showing pattern formation along the Central Dogma. Pattern formation starts with a pattern of transcription initiation, leading to a pattern of cytoplasmic mRNA, then ultimately to a protein pattern. **(B)** A conceptual framework of the reaction-diffusion model. Reaction entails the synthesis and degradation of both mRNA and protein. Both mRNA and protein diffuse through the embryo. For simplicity, we assume that the embryo is one-dimensional along the anterior-posterior axis.

protein as well as diffusion coefficients of both mRNA and protein. For simplicity, we assume that the embryo is one-dimensional along the anterior-posterior axis (Fig. 1 B). From previous measurements, some of these parameters were readily available, and if not, we could make educated guesses from the measurements from similar systems (Abu-Arish et al. 2010; Little, Tikhonov, and Gregor 2013) With these parameters at hand, we could generate predictions of the protein pattern given the rate of transcription as a function of space and time.

To test the predictive power of our model, we built an experimental system where we can simultaneously measure the transcription dynamics and protein output in real-time. Specifically, we combined the MS2-MCP system with the LlamaTag in a synthetic gene

cassette to simultaneously monitor the transcription and translation events (Bertrand et al. 1998; Bothma et al. 2018; Garcia et al. 2013b; Lucas et al. 2013). By plugging in the rate of transcription from the MS2-MCP measurement, combined with the best estimates of the SDD model parameters, we could get a quantitative prediction for the protein level along space and time. This predicted protein pattern along the anterior-posterior axis can be directly compared with the measured protein pattern revealed by the LlamaTag.

As a proof of concept, we chose two sets of parameters, one that is our best guess and the other that deviates from our best guess (Abu-Arish et al. 2010; Little, Tikhonov, and Gregor 2013), to generate the predicted patterns of protein at different time points. To contrast this prediction with the experimental data, we calculated the correlation coefficients between predictions and measurement. We expected to see a better correlation from our best-guessed parameters than the one that deviates from our best guesses. As expected, the correlation between experiments and predictions was higher for our best-guessed parameters. This suggested that the reaction-diffusion model could explain the experimental data quite nicely, and that the inferred parameters roughly match previously measured values.

We noticed one caveat that the predicted protein level always has non-zero values in nuclear cycle 13 due to active transcription during nuclear cycle 13. However, the measured protein level shows almost the background level of fluorescence during nuclear cycle 13 and increases only during nuclear cycle 14. A couple of scenarios could explain this discrepancy: First, the translation is more active during nuclear cycle 14 compared to nuclear cycle 13. Second, our measurement is limited for detecting a low level of nuclear protein due to the high background of fluorophores by the design of the LlamaTag scheme (Bothma et al. 2018).

The first hypothesis is in line with recent experimental results proposing that the translation of zygotic *hunchback* mRNA is under spatio-temporal regulation (Vinter et al. 2021). Further investigation is needed in theoretical modeling and experimental measurements to test the spatiotemporal dependence of these biophysical parameters, potentially revealing another hidden knobs of gene regulation during development.

Our result showcases what we can learn from the dialogue between theoretical modeling and quantitative measurements. Starting from the simplest assumption that the biophysical parameters for the SDD model are static, we generated an experimentally testable prediction. By contrasting this prediction to quantitative data measured by live-imaging techniques, we could falsify our prediction, which led us to revise and build new hypotheses.

2 Results

A theoretical framework of reaction-diffusion model to predict the protein pattern from transcriptional pattern

The theoretical framework is based on the reaction-diffusion model, where we assume that the major events in the embryo are synthesis, degradation, and diffusion of mRNA and protein,

respectively. The functional form of reaction-diffusion equations for mRNA and protein are given in Eqn.1 and Eqn.2.

$$\frac{\partial mRNA(x,t)}{\partial t} = \underbrace{D_m \frac{\partial^2 mRNA(x,t)}{\partial x^2}}_{\text{Diffusion}} + \underbrace{r_m(x,t)}_{\text{Synthesis}} + \underbrace{\gamma_m mRNA(x,t)}_{\text{Degradation}}, \tag{1}$$

$$\frac{\partial Protein(x,t)}{\partial t} = \underbrace{D_p \frac{\partial^2 Protein(x,t)}{\partial x^2}}_{\text{Diffusion}} + \underbrace{r_p mRNA(x,t)}_{\text{Synthesis}} + \underbrace{\gamma_p Protein(x,t)}_{\text{Degradation}}, \tag{2}$$

, where the parameters D, r, γ represent diffusion coefficient, synthesis rate, and degradation rate with subscripts m represents mRNA and p represents protein.

In this chapter, we focus on an example of *hunchback* gene as its biophysical parameters have been characterized reasonably well. Not all of these parameters have been measured experimentally, but some are better characterized than the others in the early fly embryo. To summarize our current knowledge, we put the best estimates of these parameters in Table 1 along with references. Briefly, the diffusion coefficient for protein was measured for Bicoid, a maternal transcription factor, using Fluorescence Correlation Spectroscopy (FCS) in the early fly embryo (Abu-Arish et al. 2010). FCS measures the fluctuation of fluorescence in a small volume, calculates the auto-correlation of the fluorescence, which gives a proxy for the concentration of molecules as well as the diffusion coefficient (Hess et al. 2002). The diffusion coefficient of mRNA was measured for *twist* mRNA using single-molecule live-imaging of mRNA tagged with fluorescent proteins (Dufourt et al. 2021). Notably, it is two orders of magnitude smaller than that of protein.

The half-life of protein was measured for Bicoid by using a photo-convertible fluorescent protein fusion followed by a scheme of converting bright-dark states repeatedly and measuring the remaining population of undegraded protein (Drocco et al. 2011). Drocco et al. (2011) measured the half-life of Bicoid protein to be roughly 50 minutes prior to nuclear cycle 14, then to be shorter after nuclear cycle 14. The half-life of mRNA was measured by halting the transcription initiation followed by quantification of mRNA at different time points after the transcription is stopped (Little, Tikhonov, and Gregor 2013). Little, Tikhonov, and Gregor (2013) measured the half-life of *hunchback* mRNA in the early fly embryos, acquiring roughly 60 minutes of half-life.

Measurement of transcription and protein level in real time

To generate the predicted protein pattern using the reaction-diffusion model at each position and time, we need to measure the transcription rate at each position and time. For example, we used the MS2-MCP technique, which labels the nascent transcripts whose fluorescence readout reports the number of nascent transcripts being transcribed in real-time (Bertrand et al. 1998; Garcia et al. 2013b; Lucas et al. 2013). To measure the protein pattern at each time and position, we used the LlamaTag approach, where the nanobody-tagged transcription factors

Parameter	Significance	Value	Reference
D_p	Protein diffusion coefficient	$7\mu m^2/sec$	Abu-Arish, et al, 2010
D_m	mRNA diffusion coefficient	$0.016 - 0.051\mu m^2/sec$	Dufourt, et al, 2020
T_p	Protein half-life	50 min	Drocco, et al., 2011
T_m	mRNA half-life	60 min	Little, et al, 2013
r_p	Translation rate	2 (molecules/ mRNA /min)	Petkova, et al, 2014

Table 1: Parameters for the reaction-diffusion model for mRNA and protein.

bind to fluorescent proteins that are already mature. This approach ensures no complication of slow maturation of fluorophores in the early fly embryo. Hence the fluorescence readout is proportional to the number of transcription factor protein molecules (Bothma et al. 2018).

Our construct design is illustrated in Figure 2 A. We chose the *hunchback* gene cassette as a case study because its mRNA half-life and expression pattern have been characterized very well (Little, Tikhonov, and Gregor 2013; Perry et al. 2012). Briefly, under the *hunchback* driver, we placed 24 repeats of MS2 loops for mRNA detection and LlamaTag in the N-terminal of the Hunchback coding sequence followed by *hunchback* 3'UTR. Snapshots of live-imaging measurements of this construct are shown in Figure 2 B for two different time points in nuclear cycle 14. As shown in the quantification in Figure2 C, we could see that the peak in transcription in nuclear cycle 14 (around 10 minutes into the cycle) precedes the peak of the nuclear protein (around 50-60 minutes into the cycle).

The MS2-MCP fluorescence signal is the readout of the number of actively transcribing RNA polymerases, which then can be converted to the rate of transcription initiation (Bothma et al. 2014). This rate of transcription at each time and position can be fed into the reaction-diffusion model to generate the predicted patterns of protein given a set of parameters.

Comparing model predictions with experimental measurements

With these measurements in our hand, we sought to generate predictions of protein patterns for different sets of parameters for the reaction-diffusion model (as shown in Fig. 3 A). As a proof-of-concept, we chose two sets of parameters. One set is from Table 1, which is closer to *hunchback* gene (or other gap genes), and the other set is closer to pair-rule genes, such as *even-skipped*, which are known to have shorter half-lives of mRNA and protein (Bothma et al. 2014). For convenience, we termed the former as *hunchback* (*hb*) parameters and the latter as *even-skipped* (*eve*) parameters.

As showcased in Figure 3 B, we could generate two predicted patterns of protein (at different time points) for these two sets of parameters. We can then compare these two predictions with the measured protein patterns shown in Figure 3 B.

We calculated the correlation coefficients between predictions and measurement to contrast this prediction with the experimental data. We expected to see a better correlation from our best-guessed parameters than the one that deviates from our best guesses. As expected, the correlation between experiments and predictions were higher for the *hunchback* parameters than the *even-skipped* parameters. This result suggested that the reaction-diffusion model could explain the experimental data nicely and that the inferred parameters roughly match previously measured values.

Lastly, we tested the parameter sensitivity by fixing all the parameter values as *hunchback* parameters, then changed two parameters at a time. We could see how sensitive this correlation is for each parameter by monitoring Pearson's correlation coefficient. As shown in Figure 4 A (Left), we could see that the diffusion of mRNA should be slow, and the half-life of mRNA should be quite long such that on the order of tens of minutes. Furthermore, as shown in Figure 4 A (Right), the protein diffusion has a sweet spot, which means that it should not be too fast nor too slow, but on the order of $1 - 10\mu m^2/sec$, which is closer to the measured values for Bicoid. Also, the protein half-life should be longer than tens of minutes, similar to the mRNA half-life. Overall, this exploration matches well with our previous knowledge of biophysical parameters for the reaction-diffusion model. Of course, a more systematic exploration of the parameter sensitivity is needed. Since we have five parameters, the exhaustive parameter sensitivity test was challenging. We discuss how we could explore this parameter sensitivity from the Bayesian inference viewpoint and further challenge our models in the Discussion.

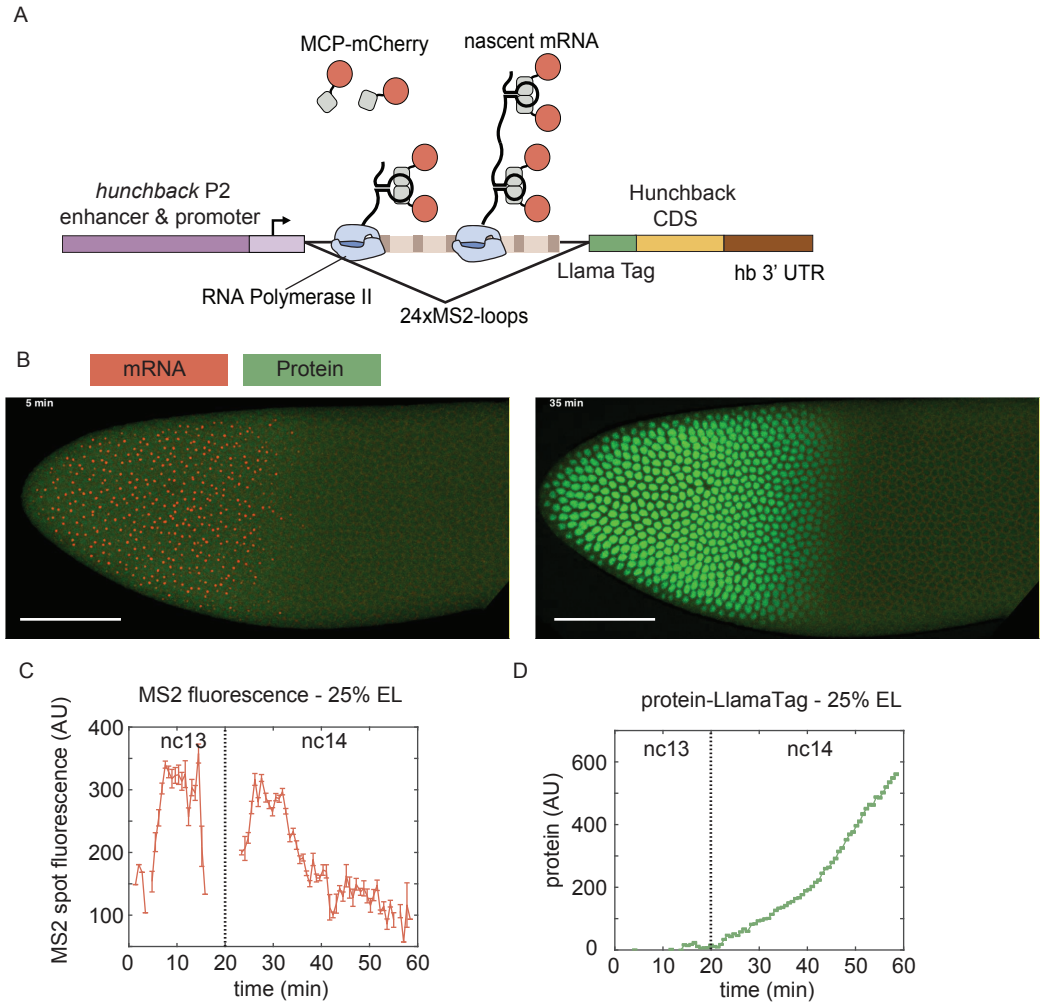

Figure 2: Schematics of the reporter construct for monitoring transcription and translation in real-time. Experimental methods to simultaneously measure the transcriptional activity and protein patterns. **(A)** Schematics of our construct. *hunchback* P2P driver is followed by 24 repeats of the MS2 loop, a LlamaTag, *hunchback* coding sequence (CDS), and *hunchback* 3'UTR. **(B)** Two snapshots of an embryo expressing the reporter constructs are shown in (A). (Left) An embryo in early nuclear cycle 14. Transcriptional loci are shown as red spots. The protein pattern has not emerged yet. (Right) The same embryo as on the left, but in late nuclear cycle 14. Transcriptional activity has halted at this point, and the protein pattern emerged. The scale bar represents $100\mu m$. **(C)** MS2 spot fluorescence time trace averaged over 2.5% spatial bin at 25% of the embryo length (EL). **(D)**The LlamaTag protein nuclear fluorescence time trace averaged over 2.5% spatial bin at 25% of the embryo length.

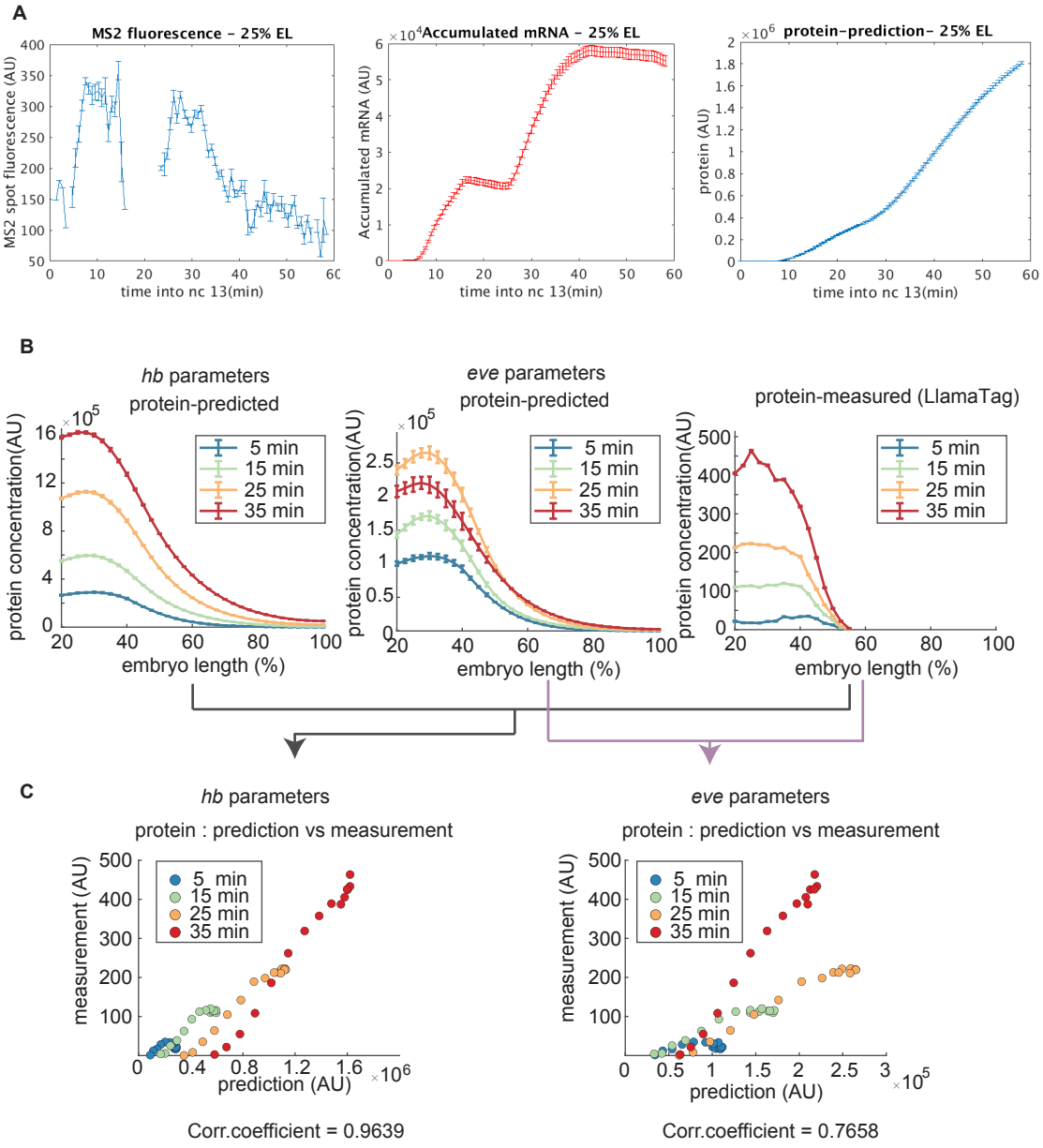

Figure 3: Prediction of protein pattern using the coupled Reaction-Diffusion model. See caption in the next page.

Figure 3: Prediction of protein pattern using the coupled Reaction-Diffusion model.**(A)** Example of numerical calculation for the accumulated mRNA and protein time-trace using the equation in (A), with a set of parameters from Table.1 at the position of 25% of the embryo length. (Left) Averaged MS2 spot fluorescence (over ON nuclei) (Center) Accumulated mRNA (Right) Protein over the time course of nc13 and nc14. **(B)** The spatial profile of protein at four time points : (Left and Center) the predicted paterrns of protein with two different sets of parameters (Right) measured protein patterns. (Left) using the *hb* parameters ($D_m = 0\mu m^2/sec$, $T_m = 60$ min, $D_p = 7\mu m^2/sec$, $T_p = 50$ min), (Center) using the *eve* parameters ($D_m = 0\mu m^2/sec$, $T_m = 7$ min, $D_p = 7\mu m^2/sec$, $T_p = 7$ min). The difference between the *hb* and *eve* parameters are different half-lives of mRNA and protein. **(C)** Comparison of prediction and measurement for two different sets of parameters used in (B). The prediction and measurement values are one-to-one paired by the time point and their position along the anterior-posterior axis. (Left, comparison drawn in black lines) *hb* parameters, (Right, comparison drawn in purple lines) *eve* parameters. In an ideal scenario where we can predict the protein pattern perfectly at each time point, the prediction and measurement should be perfectly correlated. Thus, we used Pearson's correlation coefficient to score the predictability of a specific set of parameters. Correlation coefficients for the two sets of parameters are shown at the bottom of each plot.

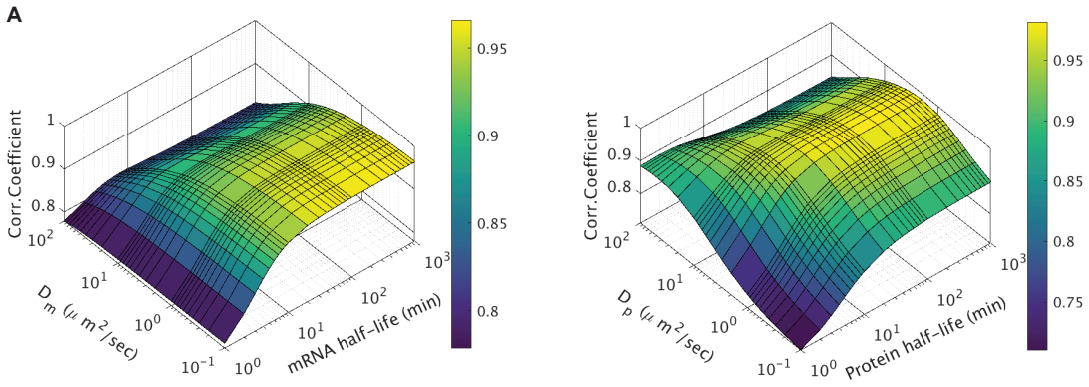

Figure 4: Parameter sensitivity for Pearson's correlation coefficient of prediction and measurement. **(A)** Here, we fixed either mRNA or protein parameters, then see how the correlation coefficient changes for different parameter regimes of protein or mRNA. (Left) Protein parameters are fixed as in Table 1. mRNA parameters (D_m,T_m) are tuned for 4 orders of magnitude. For each set of mRNA parameters, the correlation coefficient is shown in Z-axis, color-coded as the color bar shown in right. (Right) mRNA parameters are fixed as in Table 1. Protein parameters (D_p,T_p) are tuned for 4 orders of magnitude. For each set of protein parameters, the correlation coefficient is shown in Z-axis, color coded as the colorbar shown in right. These plots show that there is a regime of parameters that shows a higher correlation between prediction and measurement.

3 Discussion

Overall, we have built a theoretical framework to connect the patterns of transcription to the patterns of protein using the reaction-diffusion framework. Most studies have focused on using this model to infer the biophysical parameters, yet missing one or two parameters depending on circumstances (Jaeger et al. 2004; Surkova et al. 2019). This leaves a question on how much we can justify the inferred parameters to biologically meaningful parameters. Here, we take another approach to challenge the model by starting from the prediction and testing it experimentally.

Using the MS2-MCP technique to measure the rate of transcription, we could generate experimentally testable predictions of the protein patterns. We then contrasted the predicted protein patterns with experimentally measured protein patterns using the LlamaTag at each point in space and time. By doing this, we could assess whether a given set of parameters could explain our data well or not. Finally, our proof-of-concept test using two widely different sets of parameters revealed that this framework of comparing predictions and measurements could work to favor one set of parameters over another.

For future directions, we note a couple of points to discuss. First, we have seen that our modeling-experiment dialogue could work as a framework to infer the biophysical parameters, such as diffusion, synthesis, or degradation of mRNA and protein. We can use this framework to measure these parameters for different genes or under different conditions, which are thought to have a huge impact on these parameters. Second, we can imagine performing a more systematic parameter sensitivity test following the last section of the Results. We do not have a clear suggestion on how to approach this. However, we hope a Bayesian inference approach such as Markov-Chain Monte-Carlo (MCMC) could work as a framework to scan a wide range of parameters in an unbiased way. We hope that this could give a clearer idea of which parameters have a bigger impact in dictating the protein patterns.

4 Materials and Methods

Plasmid design and fly transgenesis

The *hb* P2 promoter and proximal enhancer are followed by 24 repeats of MS2V5 loops (Wu et al. 2015) flanked by the *hunchback* intron, and coding sequence of LlamaTag (Bothma et al. 2018) and Hunchback protein-coding sequence linked by 6xGlycine linker. This construct is subcloned into the pBphi vector, which can be integrated into specific landing sites (attP) on the fly genome by the $\phi C31$ integrase mediated insertion (Venken et al. 2011). This manuscript used the VK00033 fly line, which has a landing site on chromosome III. The VK00033 fly line is $w(-)$, and the pBphi vector carries *mini-white* gene as a positive marker for transformants. Thus, a positive selection method was used to identify transformants. The injected flies were crossed with the balancer line on chromosome III, *Dr/TM3,Sb*, and $w(+)$ F1 progeny with the balancer were selected and used to establish homozygous stocks.

To supply fluorescent protein components for both MS2 and LlamaTag, we combined *nanos* driven MCP-mCherry and *vasa* driven eGFP (Kim et al. 2021; Reimer et al. 2021). The fly line that we used has the genotype as following *yw; MCP-mCherry, Histone-iRFP; MCP-mCherry, vasa-eGFP*, where Histone-iRFP was recombined with the MCP-mCherry allele for an accurate determination of the mitosis timing.

S1 Establishment of MCP-mCherry to measure the transcription

To use the MS2-MCP signal for estimation of the mRNA production, we need to validate that the MS2 signal reports the number of RNA polymerases reliably. One way to validate this is titrating the MCP dosage and monitoring whether the MS2 signal saturates in our concentration regime of the MCP protein. MCP protein is supplied by maternal *nanos* driver randomly inserted into the fly genome using the P-element method. Thus, we could combine multiple copies of the transgene by genetic crosses to generate a wide range of MCP levels. In practice, we used two transgenic MCP lines that have the MCP transgene on either II or III. (*yw; Nos-MCP-mCherry(6); +*, *yw; + ; Nos-MCP-mCherry(3)*). Then, we used the *hb P2*-MS2 line from (**?**) to measure the transcriptional activity for different levels of MCP protein. The transcriptional activity of *hb P2* reporter peaks around 10 minutes into nc14 then decreases. We used the feature of the *hb P2* reporter that the expression peaks around ten minutes into nc14 as shown in Fig. S1 A. We used the peak intensity as a proxy for the transcriptional activity, which should be consistent over embryos if MCP protein saturates the MS2 loops. As Fig. S1 B shows, the MS2 signal saturates with 3, 4 copies of MCP transgenes but under-saturated with two copies. We could use this conclusion to construct our experimental reporter lines with saturating MCP levels.

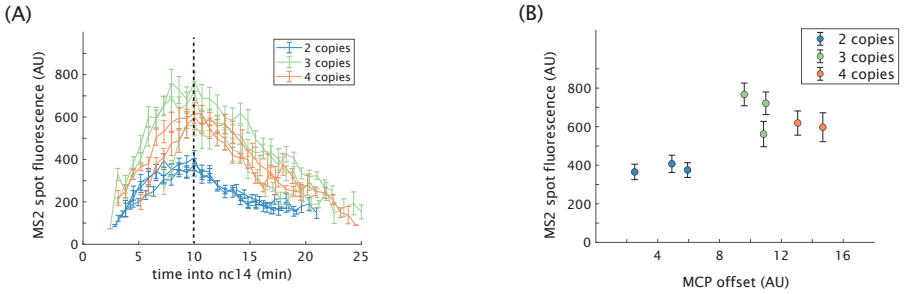

Figure S1: MCP-mCherry saturation test. (A) MS2 spot fluorescence traces during nuclear cycle 14 at 30 percent of embryo length for different MCP-mCherry dosages. Different traces are synchronized using the time point when the trace peaks. Blue, green, and red lines represent two, three, and four copies, respectively. (B) The maximum MS2 spot fluorescence at nuclear cycle 14 at the same spatial bin (along the anterior-posterior axis) for different MCP-mCherry dosages. Dosages are inferred from the offset values.

Bibliography

Abu-Arish, A. et al. (2010). "High mobility of bicoid captured by fluorescence correlation spectroscopy: implication for the rapid establishment of its gradient". In: *Biophys J* 99.4, pp. L33–5. ISSN: 1542-0086 (Electronic) 0006-3495 (Linking). DOI: S0006-3495(10)00669-7[pii]10.1016/j.bpj.2010.05.031.

Ackers, G. K., A. D. Johnson, and M. A. Shea (1982). "Quantitative model for gene regulation by lambda phage repressor". In: *Proc Natl Acad Sci U S A* 79.4, pp. 1129–33. ISSN: 0027-8424 (Print).

Alberts, Bruce (2015). *Molecular biology of the cell*. Sixth edition. New York, NY: Garland Science, Taylor and Francis Group, 1 volume (various pagings). ISBN: 9780815344322 (hardcover) 0815344325 (hardcover) 9780815344643 (paperback) 0815344643 (paperback) 9780815345244 (looseleaf) 0815345240 (looseleaf).

Arnosti, D. N. et al. (1996). "The eve stripe 2 enhancer employs multiple modes of transcriptional synergy". In: *Development* 122.1, pp. 205–14.

Barr, Kenneth A. et al. (2017). "Synthetic enhancer design by in silico compensatory evolution reveals flexibility and constraint in cis-regulation". In: *BMC Systems Biology* 11.1, pp. 1–15. ISSN: 17520509. DOI: 10.1186/s12918-017-0485-2.

Bateman, J. R., A. M. Lee, and C. T. Wu (2006). "Site-specific transformation of Drosophila via phiC31 integrase-mediated cassette exchange". In: *Genetics* 173.2, pp. 769–77. ISSN: 0016-6731 (Print) 0016-6731 (Linking). DOI: genetics.106.056945[pii]10.1534/genetics.106.056945.

Bertrand, E et al. (1998). "Localization of ASH1 mRNA particles in living yeast". In: *Mol Cell* 2.4, pp. 437–445. ISSN: 1097-2765 (Print) 1097-2765 (Linking). DOI: S1097-2765(00)80143-4[pii].

Biddle, J.W. et al. (2020). "Allosteric conformational ensembles have unlimited capacity for integrating information". In: *bioRxiv*, pp. 1–58. ISSN: 26928205. DOI: 10.1101/2020.12.10.420117.

Bintu, L. et al. (2005a). "Transcriptional regulation by the numbers: applications". In: *Curr Opin Genet Dev* 15.2, pp. 125–35.

Bintu, L. et al. (2005b). "Transcriptional regulation by the numbers: models". In: *Curr Opin Genet Dev* 15.2, pp. 116–24.

Boedicker, J. Q., H. G. Garcia, and R. Phillips (2013). "Theoretical and experimental dissection of DNA loop-mediated repression". In: *Phys Rev Lett* 110.1, p. 018101. ISSN: 1079-7114 (Electronic) 0031-9007 (Linking). DOI: 10.1103/PhysRevLett.110.018101.

Boedicker, J. Q. et al. (2013). "DNA sequence-dependent mechanics and protein-assisted bending in repressor-mediated loop formation". In: *Phys Biol* 10.6, p. 066005. ISSN: 1478-3975 (Electronic) 1478-3967 (Linking). DOI: 10.1088/1478-3975/10/6/066005.

Bolouri, H. and E. H. Davidson (2003). "Transcriptional regulatory cascades in development: initial rates, not steady state, determine network kinetics". In: *Proc Natl Acad Sci U S A* 100.16, pp. 9371–6. ISSN: 0027-8424 (Print) 0027-8424 (Linking). DOI: 10.1073/pnas.1533293100.

Bothma, J P, J Magliocco, and M Levine (2011). "The Snail Repressor Inhibits Release, Not Elongation, of Paused Pol II in the Drosophila Embryo". In: *Curr Biol*. ISSN: 1879-0445 (Electronic) 0960-9822 (Linking). DOI: 10.1016/j.cub.2011.08.019.

Bothma, J. P. et al. (2014). "Dynamic regulation of eve stripe 2 expression reveals transcriptional bursts in living Drosophila embryos". In: *Proceedings of the National Academy of Sciences* 111.29, pp. 10598–10603. ISSN: 0027-8424. DOI: 10.1073/pnas.1410022111. URL: http://www.pnas.org/cgi/doi/10.1073/pnas.1410022111.

Bothma, J. P. et al. (2018). "LlamaTags: A Versatile Tool to Image Transcription Factor Dynamics in Live Embryos". In: *Cell* 173.7, p. 1810. ISSN: 1097-4172 (Electronic) 0092-8674 (Linking). DOI: 10.1016/j.cell.2018.03.069.

Brewster, R. C. et al. (2014). "The transcription factor titration effect dictates level of gene expression". In: *Cell* 156.6, pp. 1312–23. ISSN: 1097-4172 (Electronic) 0092-8674 (Linking). DOI: 10.1016/j.cell.2014.02.022.

Briscoe, James and Stephen Small (2015). "Morphogen rules: Design principles of gradient-mediated embryo patterning". In: *Development (Cambridge)* 142.23, pp. 3996–4009. ISSN: 14779129. DOI: 10.1242/dev.129452.

Chen, Fei et al. (2015). "Stably paused genes revealed through inhibition of transcription initiation by the TFIIH inhibitor triptolide". In: *Genes and Development* 29.1, pp. 39–47. ISSN: 15495477. DOI: 10.1101/gad.246173.114.

Chen, H et al. (2012). "A system of repressor gradients spatially organizes the boundaries of bicoid-dependent target genes". In: *Cell* 149.3, pp. 618–629. ISSN: 1097-4172 (Electronic) 0092-8674 (Linking). DOI: 10.1016/j.cell.2012.03.018.

Courey, A. J. and S. Jia (2001). "Transcriptional repression: the long and the short of it". In: *Genes Dev* 15.21, pp. 2786–96.

Crocker, J, G R Ilsley, and D L Stern (2016). "Quantitatively predictable control of Drosophila transcriptional enhancers in vivo with engineered transcription factors". In: *Nat Genet* 48.3, pp. 292–298. ISSN: 1546-1718 (Electronic) 1061-4036 (Linking). DOI: 10.1038/ng.3509.

Dodd, I B et al. (2004). "Cooperativity in long-range gene regulation by the lambda {CI} repressor". In: *Genes Dev* 18.3, pp. 344–354.

Driever, W. and C. Nusslein-Volhard (1988). "The bicoid protein determines position in the Drosophila embryo in a concentration-dependent manner". In: *Cell* 54.1, pp. 95–104. ISSN: 0092-8674 (Print) 0092-8674 (Linking).

Driever, W. and C. Nusslein-Volhard (1989). "The bicoid protein is a positive regulator of hunchback transcription in the early Drosophila embryo". In: *Nature* 337.6203, pp. 138–43. ISSN: 0028-0836 (Print) 0028-0836 (Linking). DOI: 10.1038/337138a0.

Driever, W., G. Thoma, and C. Nusslein-Volhard (1989). "Determination of spatial domains of zygotic gene expression in the Drosophila embryo by the affinity of binding sites for the bicoid morphogen". In: *Nature* 340.6232, pp. 363–7. ISSN: 0028-0836 (Print) 0028-0836 (Linking). DOI: 10.1038/340363a0.

Drocco, J. A. et al. (2011). "Measurement and perturbation of morphogen lifetime: effects on gradient shape". In: *Biophys J* 101.8, pp. 1807–15. ISSN: 1542-0086 (Electronic) 0006-3495 (Linking). DOI: 10.1016/j.bpj.2011.07.025.

Dufourt, J et al. (2018). "Temporal control of gene expression by the pioneer factor Zelda through transient interactions in hubs". In: *Nat Commun* 9.1, p. 5194. ISSN: 2041-1723 (Electronic) 2041-1723 (Linking). DOI: 10.1038/s41467-018-07613-z.

Dufourt, Jeremy et al. (2021). "Imaging translation dynamics in live embryos reveals spatial heterogeneities". In: *Science* 372.6544, pp. 840–844. ISSN: 10959203. DOI: 10.1126/science.abc3483.

Eck, Elizabeth et al. (Mar. 2020). "Quantitative dissection of transcription in development yields evidence for transcription factor-driven chromatin accessibility". In: *bioRxiv*, p. 2020.01.27.922054. DOI: 10.1101/2020.01.27.922054. URL: https://doi.org/10.1101/2020.01.27.922054.

Estrada, J et al. (2016a). "Information Integration and Energy Expenditure in Gene Regulation". In: *Cell* 166.1, pp. 234–244. ISSN: 1097-4172 (Electronic) 0092-8674 (Linking). DOI: 10.1016/j.cell.2016.06.012.

Estrada, J. et al. (2016b). "SiteOut: An Online Tool to Design Binding Site-Free DNA Sequences". In: *PLoS One* 11.3, e0151740. ISSN: 1932-6203 (Electronic) 1932-6203 (Linking). DOI: 10.1371/journal.pone.0151740.

Fakhouri, W D et al. (2010). "Deciphering a transcriptional regulatory code: modeling short-range repression in the Drosophila embryo". In: *Mol Syst Biol* 6, p. 341. ISSN: 1744-4292 (Electronic) 1744-4292 (Linking). DOI: msb200997[pii]10.1038/msb.2009.97.

Furlong, E E M and M Levine (2018). "Developmental enhancers and chromosome topology". In: *Science* 361.6409, pp. 1341–1345. ISSN: 1095-9203 (Electronic) 0036-8075 (Linking). DOI: 10.1126/science.aau0320.

Garcia, H G and R Phillips (2011). "Quantitative dissection of the simple repression input-output function". In: *Proc Natl Acad Sci U S A* 108.29, pp. 12173–12178. ISSN: 1091-6490 (Electronic) 0027-8424 (Linking). DOI: 1015616108[pii]10.1073/pnas.1015616108.

Garcia, H. G. et al. (2012). "Operator sequence alters gene expression independently of transcription factor occupancy in bacteria". In: *Cell Rep* 2.1, pp. 150–61. ISSN: 2211-1247 (Electronic). DOI: 10.1016/j.celrep.2012.06.004.

Garcia, H. G. et al. (2013a). "Quantitative imaging of transcription in living Drosophila embryos links polymerase activity to patterning". In: *Curr Biol* 23.21, pp. 2140–5. ISSN: 1879-0445 (Electronic) 0960-9822 (Linking). DOI: 10.1016/j.cub.2013.08.054.

Garcia, Hernan G et al. (2013b). *Quantitative Imaging of Transcription in Living Drosophila Embryos Links Polymerase Activity to Patterning*. DOI: 10.1016/j.cub.2013.08.054.

Garcia, Hernan G. et al. (Jan. 2020). "Lighting up the central dogma for predictive developmental biology". In: *Current Topics in Developmental Biology*. Vol. 137. Academic Press Inc., pp. 1–35. ISBN: 9780128127902. DOI: 10.1016/bs.ctdb.2019.10.010.

Gebauer, Fátima and Matthias W. Hentze (2004). "Molecular mechanisms of translational control". In: *Nature Reviews Molecular Cell Biology* 5.10, pp. 827–835. ISSN: 14710072. DOI: 10.1038/nrm1488.

Gergen, J. P. and B. A. Butler (1988). "Isolation of the Drosophila segmentation gene runt and analysis of its expression during embryogenesis." In: *Genes & development* 2.9, pp. 1179–1193. ISSN: 08909369. DOI: 10.1101/gad.2.9.1179.

Geyer, Charles J. and Elizabeth A. Thompson (1992). "Constrained Monte Carlo Maximum Likelihood for Dependent Data". In: *Journal of the Royal Statistical Society: Series B (Methodological)* 54.3, pp. 657–683. ISSN: 0035-9246. DOI: 10.1111/j.2517-6161.1992.tb01443.x.

Gilbert, Scott F. (2010). *Developmental biology*. 9th. Sunderland, Mass.: Sinauer Associates, xxi, 711, 80 p. ISBN: 9780878933846 (casebound) 0878933840 (casebound) 9780878935642 (hbk.) 0878935649 (hbk.)

Giniger, E. and M. Ptashne (1988). "Cooperative DNA binding of the yeast transcriptional activator GAL4". In: *Proc Natl Acad Sci U S A* 85.2, pp. 382–6. ISSN: 0027-8424 (Print).

Gratz, S. J. et al. (2015). "CRISPR-Cas9 Genome Editing in Drosophila". In: *Curr Protoc Mol Biol* 111, pp. 31 2 1–20. ISSN: 1934-3647 (Electronic) 1934-3647 (Linking). DOI: 10.1002/0471142727.mb3102s111.

Gray, S, P Szymanski, and M Levine (1994). "Short-Range Repression Permits Multiple Enhancers to Function Autonomously within a Complex Promoter". In: *Genes Dev* 8.15, pp. 1829–1838. ISSN: 0890-9369.

Gregor, T. et al. (2007a). "Stability and nuclear dynamics of the bicoid morphogen gradient". In: *Cell* 130.1, pp. 141–52. ISSN: 0092-8674 (Print).

Gregor, Thomas et al. (July 2007b). "Probing the Limits to Positional Information". In: *Cell* 130.1, pp. 153–164. URL: http://linkinghub.elsevier.com/retrieve/pii/S0092867407006629file:///Users/martini/Dropbox/Library.papers3/Files/31/3192646E-0499-41BF-9AA1-4667DECB99D3papers3://publication/doi/10.1016/j.cell.2007.05.025.

Haario, Heikki, Eero Saksman, and Johanna Tamminen (2001). "An Adaptive Metropolis Algorithm". In: *Bernoulli* 7.2, pp. 223–242. ISSN: 13507265. URL: http://www.jstor.org/stable/3318737.

Haario, Heikki et al. (2006). "DRAM: Efficient adaptive MCMC". In: *Statistics and Computing* 16.4, pp. 339–354. ISSN: 1573-1375. DOI: 10.1007/s11222-006-9438-0. URL: https://doi.org/10.1007/s11222-006-9438-0.

Hang, Saiyu and J. Peter Gergen (2017). "Different modes of enhancer-specific regulation by Runt and Even-skipped during Drosophila segmentation". In: *Molecular Biology of the Cell* 28.5, pp. 681–691. ISSN: 19394586. DOI: 10.1091/mbc.E16-09-0630.

Hannon, Colleen E., Shelby a. Blythe, and Eric F. Wieschaus (2017). "Concentration dependent chromatin states induced by the bicoid morphogen gradient". In: *eLife* 6, pp. 1–29. ISSN: 2050084X. DOI: 10.7554/eLife.28275. arXiv: 0610070v2 [hep-th].

Harrison, M. M., M. R. Botchan, and T. W. Cline (2010). "Grainyhead and Zelda compete for binding to the promoters of the earliest-expressed Drosophila genes". In: *Dev Biol* 345.2, pp. 248–55. ISSN: 1095-564X (Electronic) 0012-1606 (Linking). DOI: 10.1016/j.ydbio.2010.06.026.

He, X et al. (2010). "Thermodynamics-based models of transcriptional regulation by enhancers: the roles of synergistic activation, cooperative binding and short-range repression". In: *PLoS Comput Biol* 6.9. ISSN: 1553-7358 (Electronic) 1553-734X (Linking). DOI: 10.1371/journal.pcbi.1000935.

Hertz, Gerald Z., George W. Hartzell, and Gary D. Stormo (1990). "Identification of consensus patterns in unaligned DNA sequences known to be functionally related". In: *Bioinformatics* 6.2, pp. 81–92. ISSN: 13674803. DOI: 10.1093/bioinformatics/6.2.81.

Hertz, Gerald Z. and Gary D. Stormo (1999). "Identifying DNA and protein patterns with statistically significant alignments of multiple sequences". In: *Bioinformatics* 15.7-8, pp. 563–577. ISSN: 13674803. DOI: 10.1093/bioinformatics/15.7.563.

Hess, Samuel T. et al. (2002). "Biological and chemical applications of fluorescence correlation spectroscopy: A review". In: *Biochemistry* 41.3, pp. 697–705. ISSN: 00062960. DOI: 10.1021/bi0118512.

Hewitt, G. F. et al. (1999). "Transcriptional repression by the Drosophila giant protein: cis element positioning provides an alternative means of interpreting an effector gradient". In: *Development* 126.6, pp. 1201–10. ISSN: 0950-1991 (Print) 0950-1991 (Linking).

Ip, Y. T. et al. (1992). "dorsal-twist interactions establish snail expression in the presumptive mesoderm of the Drosophila embryo". In: *Genes Dev* 6.8, pp. 1518–30. ISSN: 0890-9369 (Print) 0890-9369 (Linking).

Jaeger, J. et al. (2004). "Dynamic control of positional information in the early Drosophila embryo". In: *Nature* 430.6997, pp. 368–71. ISSN: 1476-4687 (Electronic) 0028-0836 (Linking). DOI: 10.1038/nature02678.

Jaynes, J. B. and P. H. O'Farrell (1991). "Active repression of transcription by the Engrailed homeodomain protein". In: *EMBO Journal* 10.6, pp. 1427–1433. ISSN: 02614189. DOI: 10.1002/j.1460-2075.1991.tb07663.x.

Jiang, J. and M. Levine (1993). "Binding affinities and cooperative interactions with bHLH activators delimit threshold responses to the dorsal gradient morphogen". In: *Cell* 72.5, pp. 741–52. ISSN: 0092-8674 (Print) 0092-8674 (Linking).

Kim, Yang Joon et al. (2021). "Predictive modeling reveals that higher-order cooperativity drives transcriptional repression in a synthetic developmental enhancer". In: *bioRxiv*, pp. 1–55.

Koromila, Theodora and Angelike Stathopoulos (2017). "Broadly expressed repressors integrate patterning across orthogonal axes in embryos". In: *Proceedings of the National Academy of Sciences* 6, p. 201703001. ISSN: 0027-8424. DOI: 10.1073/pnas.1703001114. URL: http://www.pnas.org/lookup/doi/10.1073/pnas.1703001114.

Koromila, Theodora and Angelike Stathopoulos (2019). "Distinct Roles of Broadly Expressed Repressors Support Dynamic Enhancer Action and Change in Time". In: *Cell Reports* 28.4, pp. 855–863. ISSN: 22111247. DOI: 10.1016/j.celrep.2019.06.063. URL: https://doi.org/10.1016/j.celrep.2019.06.063.

Kulkarni, M. M. and D. N. Arnosti (2005). "cis-regulatory logic of short-range transcriptional repression in Drosophila melanogaster". In: *Mol Cell Biol* 25.9, pp. 3411–20. ISSN: 0270-7306 (Print).

Lammers, Nicholas C. et al. (2020). "Multimodal transcriptional control of pattern formation in embryonic development". In: *Proceedings of the National Academy of Sciences of the United States of America* 117.2, pp. 836–847. ISSN: 10916490. DOI: 10.1073/pnas.1912500117.

Lebrecht, D. et al. (2005). "Bicoid cooperative DNA binding is critical for embryonic patterning in Drosophila". In: *Proc Natl Acad Sci U S A* 102.37, pp. 13176–81. ISSN: 0027-8424 (Print) 0027-8424 (Linking). DOI: 10.1073/pnas.0506462102.

Li, C. et al. (2018). "Frequency Modulation of Transcriptional Bursting Enables Sensitive and Rapid Gene Regulation". In: *Cell Syst* 6.4, 409–423 e11. ISSN: 2405-4712 (Print) 2405-4712 (Linking). DOI: 10.1016/j.cels.2018.01.012.

Li, J. and D. S. Gilmour (2011). "Promoter proximal pausing and the control of gene expression". In: *Curr Opin Genet Dev* 21.2, pp. 231–5. ISSN: 1879-0380 (Electronic) 0959-437X (Linking). DOI: S0959-437X(11)00014-1[pii]10.1016/j.gde.2011.01.010.

Little, S. C., M. Tikhonov, and T. Gregor (2013). "Precise developmental gene expression arises from globally stochastic transcriptional activity". In: *Cell* 154.4, pp. 789–800. ISSN: 1097-4172 (Electronic) 0092-8674 (Linking). DOI: 10.1016/j.cell.2013.07.025.

Liu, Jonathan et al. (2021). "Real-time single-cell characterization of the eukaryotic transcription cycle reveals correlations between RNA initiation, elongation, and cleavage". In: *bioRxiv*, p. 2020.08.29.273474. ISSN: 26928205. DOI: 10.1371/journal.pcbi.1008999. URL: https://www.biorxiv.org/content/10.1101/2020.08.29.273474v4%0Ahttps://www.biorxiv.org/content/10.1101/2020.08.29.273474v4.abstract.

Löhr, Ulrike et al. (2009). "Antagonistic action of Bicoid and the repressor Capicua determines the spatial limits of Drosophila head gene expression domains". In: *Proceedings of the National Academy of Sciences of the United States of America* 106.51, pp. 21695–21700. ISSN: 00278424. DOI: 10.1073/pnas.0910225106.

Lott, Susan E. et al. (2011). "Noncanonical compensation of zygotic X transcription in early Drosophila melanogaster development revealed through single-embryo RNA-Seq". In: *PLoS Biology* 9.2. ISSN: 15449173. DOI: 10.1371/journal.pbio.1000590.

Lucas, T. et al. (2013). "Live imaging of bicoid-dependent transcription in Drosophila embryos". In: *Curr Biol* 23.21, pp. 2135–9. ISSN: 1879-0445 (Electronic) 0960-9822 (Linking). DOI: 10.1016/j.cub.2013.08.053.

Ma, D. et al. (1996). "The local repressor AcrR plays a modulating role in the regulation of acrAB genes of Escherichia coli by global stress signals". In: *Mol Microbiol* 19.1, pp. 101–12. ISSN: 0950-382X (Print) 0950-382X (Linking).

Mayer, Jürgen, Khaled Khairy, and Jonathon Howard (2010). "Drawing an elephant with four complex parameters". In: *American Journal of Physics* 78.6, pp. 648–649. ISSN: 0002-9505. DOI: 10.1119/1.3254017.

Murata, Y. and R. P. Wharton (1995). "Binding of pumilio to maternal hunchback mRNA is required for posterior patterning in Drosophila embryos". In: *Cell* 80.5, pp. 747–56. ISSN: 0092-8674 (Print) 0092-8674 (Linking).

Nusslein-Volhard, C. and E. Wieschaus (1980). "Mutations affecting segment number and polarity in Drosophila". In: *Nature* 287.5785, pp. 795–801. ISSN: 0028-0836 (Print) 0028-0836 (Linking).

Nusslein-Volhard, C., E. Wieschaus, and H. Kluding (1984). "Mutations Affecting the Pattern of the Larval Cuticle in Drosophila-Melanogaster .1. Zygotic Loci on the 2nd Chromosome". In: *Wilhelm Rouxs Archives of Developmental Biology* 193.5, pp. 267–282. ISSN: 0340-0794.

Papagianni, Aikaterini et al. (2018). "Capicua controls Toll/IL-1 signaling targets independently of RTK regulation". In: *Proceedings of the National Academy of Sciences* 115.8, p. 201713930. ISSN: 0027-8424. DOI: 10.1073/pnas.1713930115. URL: http://www.pnas.org/lookup/doi/10.1073/pnas.1713930115.

Park, Jeehae et al. (2019). "Dissecting the sharp response of a canonical developmental enhancer reveals multiple sources of cooperativity". In: pp. 1–25.

Parker, D. S. et al. (2011). "The cis-regulatory logic of Hedgehog gradient responses: key roles for gli binding affinity, competition, and cooperativity". In: *Sci Signal* 4.176, ra38. ISSN: 1937-9145 (Electronic). DOI: 10.1126/scisignal.2002077.

Peeters, Eveline et al. (2013). "A thermodynamic model of the cooperative interaction between the archaeal transcription factor Ss-LrpB and its tripartite operator DNA". In: *Gene* 524.2, pp. 330–340. ISSN: 03781119. DOI: 10.1016/j.gene.2013.03.118. URL: http://dx.doi.org/10.1016/j.gene.2013.03.118.

Perry, M. W., A. N. Boettiger, and M. Levine (2011). "Multiple enhancers ensure precision of gap gene-expression patterns in the Drosophila embryo". In: *Proc Natl Acad Sci U S A*. ISSN: 1091-6490 (Electronic) 0027-8424 (Linking). DOI: 10.1073/pnas.1109873108.

Perry, M. W. et al. (2012). "Precision of hunchback expression in the Drosophila embryo". In: *Curr Biol* 22.23, pp. 2247–52. ISSN: 1879-0445 (Electronic) 0960-9822 (Linking). DOI: 10.1016/j.cub.2012.09.051.

Phillips, Rob, Jane Kondev, and Julie Theriot (2009). *Physical biology of the cell*. New York: Garland Science, xxiv, 807 p. ISBN: 9780815341635 0815341636.

Phillips, Rob et al. (2019). "Figure 1 Theory Meets Figure 2 Experiments in the Study of Gene Expression". In: *Annu. Rev. Biophys* 48, pp. 121–163. DOI: 10.1146/annurev-biophys-052118. URL: https://doi.org/10.1146/annurev-biophys-052118-.

Ptashne, M. and A. Gann (2002). *Genes and Signals*. New York: Cold Spring Harbor Laboratory Press.

Ptashne, Mark (2004). *A genetic switch: phage lambda revisited*. 3rd. Cold Spring Harbor, N.Y.: Cold Spring Harbor Laboratory Press, xiv, 154 p. ISBN: 0879697172 (cloth) 0879697164 (pbk. alk. paper).

Razo-Mejia, M et al. (2018). "Tuning Transcriptional Regulation through Signaling: A Predictive Theory of Allosteric Induction". In: *Cell Syst* 6.4, pp. 456–469. ISSN: 2405-4712 (Print) 2405-4712 (Linking). DOI: 10.1016/j.cels.2018.02.004.

Razo-Mejia, M. et al. (2020). "First-principles prediction of the information processing capacity of a simple genetic circuit". In: *Phys Rev E* 102.2-1, p. 022404. ISSN: 2470-0053 (Electronic) 2470-0045 (Linking). DOI: 10.1103/PhysRevE.102.022404.

Reeves, G T et al. (2012). "Dorsal-Ventral Gene Expression in the Drosophila Embryo Reflects the Dynamics and Precision of the Dorsal Nuclear Gradient". In: *Dev Cell*. ISSN: 1878-1551 (Electronic) 1534-5807 (Linking). DOI: 10.1016/j.devcel.2011.12.007.

Reimer, Armando et al. (2021). "Minimal synthetic enhancers reveal control of the probability of transcriptional engagement and its timing by a morphogen gradient". In: pp. 1–41.

Rivera, John et al. (2019). "REDfly: The transcriptional regulatory element database for Drosophila". In: *Nucleic Acids Research* 47.D1, pp. D828–D834. ISSN: 13624962. DOI: 10.1093/nar/gky957.

Rödel, Claudia J., Anna F. Gilles, and Michalis Averof (2013). "MicroRNAs act as cofactors in bicoid-mediated translational repression". In: *Current Biology* 23.16, pp. 1579–1584. ISSN: 09609822. DOI: 10.1016/j.cub.2013.06.041.

Sauer, F. and H. Jackle (1991). "Concentration-dependent transcriptional activation or repression by Kruppel from a single binding site". In: *Nature* 353.6344, pp. 563–6. ISSN: 0028-0836 (Print) 0028-0836 (Linking). DOI: 10.1038/353563a0.

Sayal, R et al. (2016). "Quantitative perturbation-based analysis of gene expression predicts enhancer activity in early Drosophila embryo". In: *Elife* 5. ISSN: 2050-084X (Electronic) 2050-084X (Linking). DOI: 10.7554/eLife.08445.

Segal, E et al. (2008). "Predicting expression patterns from regulatory sequence in Drosophila segmentation". In: *Nature* 451.7178, pp. 535–540. ISSN: 1476-4687 (Electronic). DOI: nature06496[pii]10.1038/nature06496.

Sepulveda, L. A. et al. (2016). "Measurement of gene regulation in individual cells reveals rapid switching between promoter states". In: *Science* 351.6278, pp. 1218–22. ISSN: 1095-9203 (Electronic) 0036-8075 (Linking). DOI: 10.1126/science.aad0635.

Sivia, D and J Skilling (2006). *Data Analysis: A Bayesian Tutorial*. OUP Oxford. ISBN: 9780191546709.

Small, S., A. Blair, and M. Levine (1992). "Regulation of even-skipped stripe 2 in the Drosophila embryo". In: *EMBO J* 11.11, pp. 4047–57.

Small, Stephen (2000). "In Vivo Analysis of lacZ Fusion Genes in Transgenic Drosophila melanogaster". In: 326.1988, pp. 146–159.

Small, Stephen and David N. Arnosti (2020). "Transcriptional enhancers in Drosophila". In: *Genetics* 216.1, pp. 1–26. ISSN: 19432631. DOI: 10.1534/genetics.120.301370.

Spitz, F. and E. E. Furlong (2012). "Transcription factors: from enhancer binding to developmental control". In: *Nat Rev Genet* 13.9, pp. 613–26. ISSN: 1471-0064 (Electronic) 1471-0056 (Linking). DOI: 10.1038/nrg3207.

Surkova, Svetlana et al. (2019). "Quantitative analysis reveals genotype- and domain- specific differences between mRNA and protein expression of segmentation genes in Drosophila".

In: *Developmental Biology* 448.1, pp. 48–58. ISSN: 1095564X. DOI: 10.1016/j.ydbio.2019.01.006. URL: https://doi.org/10.1016/j.ydbio.2019.01.006.

Tanenbaum, M. E. et al. (2014). "A protein-tagging system for signal amplification in gene expression and fluorescence imaging". In: *Cell* 159.3, pp. 635–46. ISSN: 1097-4172 (Electronic) 0092-8674 (Linking). DOI: 10.1016/j.cell.2014.09.039.

Turing, Alan M. (1952). "The Chemical Basis of Morphogenesis Author (s): A . M . Turing Source : Philosophical Transactions of the Royal Society of London . Series B , Biological Published by : Royal Society Stable URL : http://www.jstor.org/stable/92463 REFERENCES Linked refer". In: *Philosophical Transactions of the Royal Society of London* 237.641, pp. 37–72.

Venken, K. J. and H. J. Bellen (2007). "Transgenesis upgrades for Drosophila melanogaster". In: *Development* 134.20, pp. 3571–84. ISSN: 0950-1991 (Print) 0950-1991 (Linking). DOI: 134/20/3571[pii]10.1242/dev.005686.

Venken, K. J. T. et al. (2011). "MiMIC: a highly versatile transposon insertion resource for engineering Drosophila melanogaster genes". In: *Nat Methods* 8.9, 737–U80. ISSN: 1548-7091. DOI: Doi10.1038/Nmeth.1662.

Vilar, J. M. and S. Leibler (2003). "DNA looping and physical constraints on transcription regulation". In: *J Mol Biol* 331.5, pp. 981–9.

Vincent, B. J., J. Estrada, and A. H. DePace (2016). "The appeasement of Doug: a synthetic approach to enhancer biology". In: *Integr Biol (Camb)* 8.4, pp. 475–84. ISSN: 1757-9708 (Electronic) 1757-9694 (Linking). DOI: 10.1039/c5ib00321k.

Vinter, Daisy J. et al. (2021). "Dynamics of hunchback translation in real-time and at single-mRNA resolution in the Drosophila embryo". In: *Development (Cambridge)* 148.18. ISSN: 14779129. DOI: 10.1242/DEV.196121.

Walrad, Pegine B., Saiyu Hang, and J. Peter Gergena (2011). "Hairless is a cofactor for Runt-dependent transcriptional regulation". In: *Molecular Biology of the Cell* 22.8, pp. 1364–1374. ISSN: 10591524. DOI: 10.1091/mbc.E10-06-0483.

Wharton, Robin P et al. (1998). "1-s2.0-S1097276500800854-main". In: 1, pp. 863–872.

Wu, B. et al. (2015). "Synonymous modification results in high-fidelity gene expression of repetitive protein and nucleotide sequences". In: *Genes Dev* 29.8, pp. 876–86. ISSN: 1549-5477 (Electronic) 0890-9369 (Linking). DOI: 10.1101/gad.259358.115.

Yan, X. et al. (2016). "Dynamics of Translation of Single mRNA Molecules In Vivo". In: *Cell* 165.4, pp. 976–89. ISSN: 1097-4172 (Electronic) 0092-8674 (Linking). DOI: 10.1016/j.cell.2016.04.034.